POLITECNICO
MILANO 1863

SCUOLA DI INGEGNERIA INDUSTRIALE
E DELL'INFORMAZIONE

Nanoemulsions as chEOR fluids: from laboratory tests to coreflooding simulations

TESI DI LAUREA MAGISTRALE IN
ENERGY ENGINEERING
INGEGNERIA ENERGETICA

Author: **Chiara Gamurrini**

Student ID: 946293
Advisor: Prof. Alberto Guadagnini
Company Advisor: Ing. Martina Sambiase
Academic Year: 2020-2021

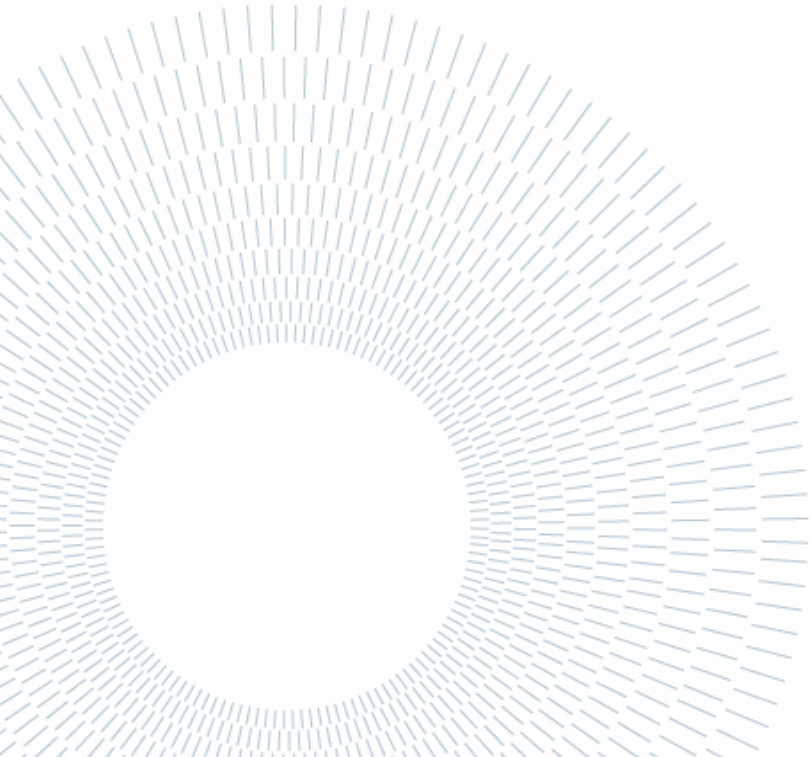

Abstract

The present thesis work, developed in collaboration with Eni, concentrates on the investigation and numerical modelling of nanoemulsions injection for Enhanced Oil Recovery (*EOR*). The purpose of the work is to identify a robust simulation workflow able to catch nanoemulsions behavior in porous media and to predict the additional oil recovery obtained by this type of chemical injection.
Nanoemulsions are an emergent *EOR* technique based on the synergic effect given by the presence of two immiscible phases (water and a solvent) and surfactants, used to stabilize the dispersed phase in droplet shape.
CMG STARS commercial simulator has been used to model the recovery process. At the beginning, the activity has been focused on modelling the process at the laboratory scale, analyzing two oil-saturated core experiments carried out in Eni laboratories. The two experiments differ for the utilized core: the first application relies on plugs, while the second adopts slim tubes. The additional recovery obtained with nanoemulsions with respect to waterflooding registered in such experiments is between 15% and 21%. The elaborated numerical model has been consolidated through History Matching (*HM*) procedure and Global Sensitivity Analysis (*GSA*), aimed at quantifying the impact of each unknown input parameter on two of the model outputs: Recovery Factor (*RF*) and Bottom Hole Pressure (*BHP*). Subsequently, the results of the experiment modeling have been applied to a sector of the specific field selected inside the Eni portfolio, to perform forecast analyses. The performed simulations have shown that nanoemulsion technique is effective, however, from a preliminary economic analysis, it appears to be still too expensive in composition and formulation for industrial and field applications.

Key-words: nanoemulsions, enanhced oil recovery, CMG STARS, simulation, *GSA*.

Abstract in italiano

Il presente lavoro di tesi, sviluppato in collaborazione con Eni, si concentra sullo studio e la modellazione numerica di iniezione di nanoemulsioni per il recupero avanzato di petrolio (*EOR* - Enhanced Oil Recovery). Lo scopo del lavoro è quello di identificare una procedura di simulazione atta a cogliere il comportamento delle nanoemulsioni all'interno dei mezzi porosi e a predire il recupero addizionale ottenuto grazie all'iniezione di tale agente chimico.
Le nanoemulsioni sono una tecnologia emergente per il recupero avanzato di petrolio basata sull'effetto sinergico dato dalla presenza di due fasi immiscibili (l'acqua e il solvente) e di tensioattivi, usati per stabilizzare la fase dispersa in forma di gocce.
Per la simulazione del processo di recupero è stato utilizzato il simulatore commerciale CMG STARS. In un primo momento è stata presa in considerazione la modellazione del processo a scala di laboratorio, attraverso l'analisi di due esperimenti riguardanti il flussaggio portati avanti da Eni. Le due applicazioni sperimentali differiscono per il tipo di campione di mezzo poroso utilizzato: nel primo caso una carota satura di olio, nel secondo un tubo snello caratteristico per la sua lunghezza. Il recupero addizionale portato dalle nanoemulsioni rispetto al solo flussaggio di acqua, registrato in queste applicazioni si attesta tra il 15 e il 21%. Il modello numerico elaborato è stato consolidato attraverso una procedura di History Matching (*HM*) e una Analisi di Sensitività Globale (*GSA* – Global Sensitivity Analysis), volta a quantificare l'impatto che ogni parametro di input incognito ha sui due principali output del modello: il fattore di recupero (RF – Recovery Factor) e la pressione a fondo pozzo (*BHP* – Bottom Hole Pressure).
Successivamente, i risultati del modello sono stati applicati ad un settore del campo scelto all'interno del portfolio di Eni, per effettuare una analisi previsionale.
Le simulazioni effettuate hanno evidenziato l'efficacia della tecnologia delle nanoemulsioni, tuttavia, a seguito di una valutazione economica preliminare, risulta chiaro che i costi associati alla loro composizione e formulazione sono ancora troppo rilevanti per l'applicazione sul campo.

Parole chiave: nanoemulsioni, recupero avanzato di petrolio, CMG STARS, simulazione, Analisi di Sensitività Globale.

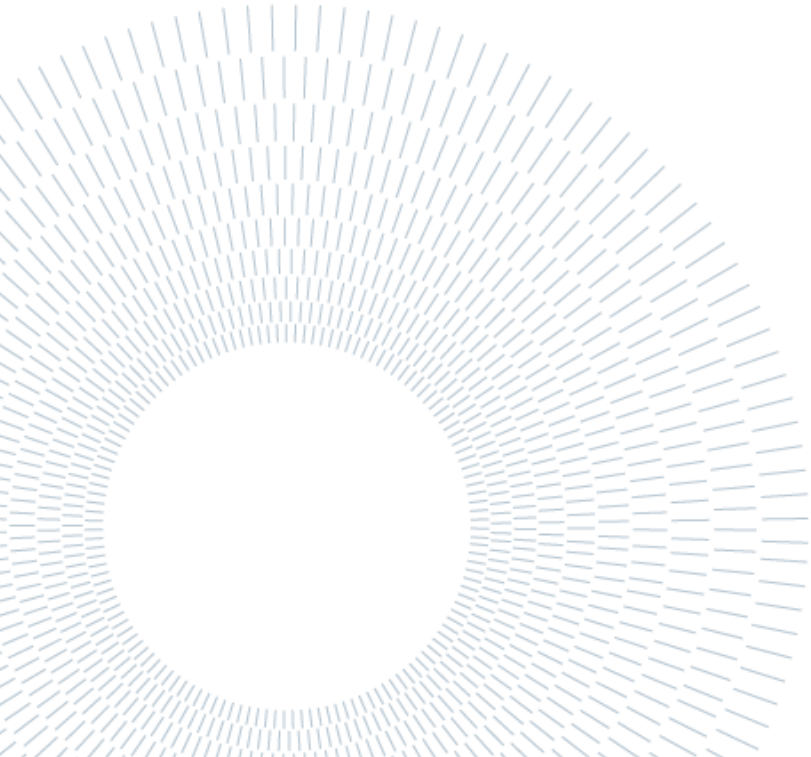

Contents

1 Introduction

1.1. General framework

Crude oil still represents one of the principal sources of energy used around the world and, according to the British Petroleum Statistical Review of World Energy [1], it leads the energy market together with other fossil fuels, covering 85% of the total energy mix in 2020 (Figure 1.1). To be more precise, oil is the first source by consumption (31.2%) followed by coal (27.2%) and gas (24.7%).

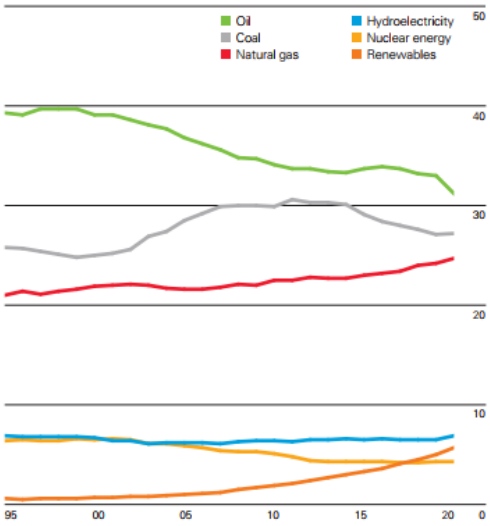

Figure 1.1: Shares of global primary energy according to BP [1].

British Petroleum Energy Outlook [2] highlights three possible scenarios as regards the future developments of primary energy consumption until 2050:

- Rapid Transition Scenario, which posts a series of policy measures that cause a fall in carbon emissions by around 70% by 2050;
- Net Zero Scenario, which assumes that policy measures embodied in Rapid Scenario are reinforced by significant shifts in societal behavior with a decrease in carbon emission of 95%;
- Business-as-usual Scenario, which considers that government policies, technology and social preferences continue to evolve in a manner seen in the recent past.

The main characteristics of these forecasts are displayed in Figure 1.2.

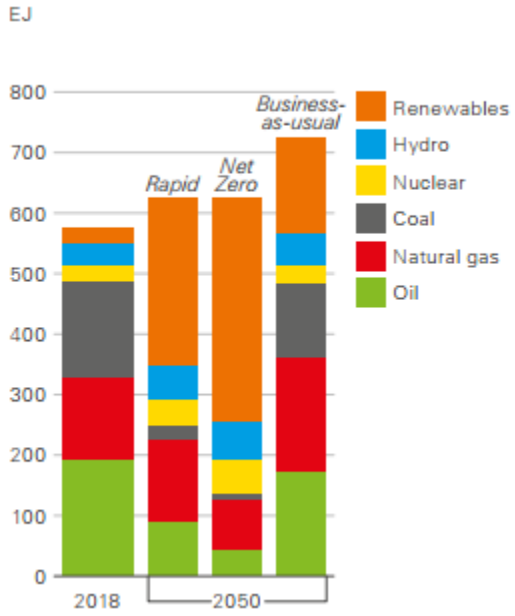

Figure 1.2: Primary energy consumption by source in the different forecast scenarios [2].[1]

The suggested scenarios focus on the issue of greenhouse gases emission that is pushing the world towards the energy transition, with the aim of reaching an almost fully renewable mix. During this period of evolution, the impactful changes are related mainly to coal, which consumption strongly decreases in all scenarios, gas, that has been addressed as the protagonist of clean energy transition, and renewables, which portion in the general mix increases significantly according to every forecast. Moreover, considering an upcoming relevant increase in the total energy required worldwide associated to population growth and global economy development, it is possible to state that oil will continue to play an important role sustaining the energy demand in the future, despite the assessed growing interest for renewables. As reported in *IEA* World Energy Outlook [3], oil demand shows a very slightly decline to 2050 in every proposed scenario but the Net Zero one, and its trend increases if petrochemical applications are analyzed (Figure 1.3).

[1] 1 EJ is around 0.5 mb/d of oil, 29 bcm of natural gas or 34 Mtce of coal according to IEA World Energy Outlook [3]

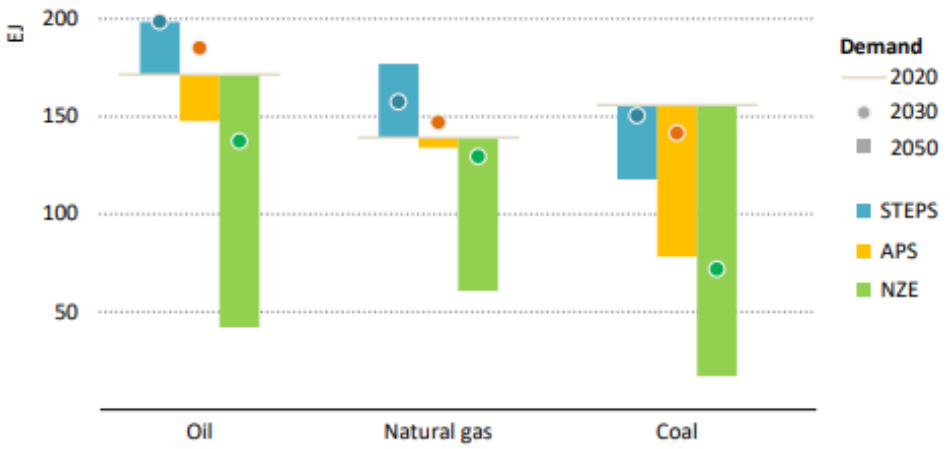

Figure 1.3: Fossil fuels use in each proposed scenario [3].

Given those considerations, the key concept to be introduced is the one of reserves: "reserves are those quantities of petroleum which are anticipated to be commercially recovered from known accumulations from a given date forward with a certain degree of uncertainty" [4]. The proved global reserves can grow either if new reservoirs are discovered or if an improvement in technology allows to increase the production from existing ones. In fact, when a new field is put into production, it undergoes different sequential strategies depending on the reservoir pressure [5,6].

1.2. Oil production mechanisms

Three different stages can be distinguished throughout the operation period of an oilfield.

The first stage (primary recovery) is based on the production of oil by natural drive mechanisms [7]:

- pressure difference between the reservoir and the well, which is capable to move hydrocarbons towards the well and then to the surface;
- expansion of fluid phases and compaction of rock formation;
- water drive, when the reservoir is in communication with an aquifer;
- depletion drive;
- gravity drainage.

However, during the field production life, the reservoir pressure decreases leading to a condition in which it is not enough to bring hydrocarbons to the surface or, if its value is below the bubble point pressure, dissolved gas comes out of solution and its production tends to prevail with respect to oil one. Once this situation is reached, the production is maintained with artificial lift techniques or reducing the

backpressure at surface facilities until the operation is no longer profitable. It can be considered that at the end of primary recovery 10 to 25% of the original oil in place (*OOIP*) should be recovered [5,8,9].

Primary recovery is followed by the second stage (secondary recovery) during which pressure maintenance is pursued with the injection of a fluid (typically water or an immiscible gas) acting as a displacing agent that sweeps oil from injection wells to producers. After some time from the injection, water breaks through the producing wells and hereinafter the percentage water produced, also called water cut (*WC*), increases. The contribution of secondary recovery is an additional 15-25% that sums up to the primary recovery giving an overall value of 50-55% of *OOIP* [5,8,9].

When the secondary recovery is no more exploitable, tertiary or enhanced oil recovery (*EOR*) is applied. The necessity of employing a third production stage originates from the general estimation that soon there will be no more significant discoveries of conventional oilfields [10,11]. For this reason, the continuous and growing request of energy, together with the depletion of oil and gas resources, lead to exploitation of reservoirs located in more critical environments where the primary source il less accessible and requires advanced recovery techniques. This stage of production relies on the injection of something different than water or immiscible gas to further improve oil recovery until the cumulative recovery factor reaches a value of 60-65% [12]. This mechanism will be further analyzed in the following sections.

In Figure 1.4 the oil production as a function of time is shown highlighting the different operating steps just described.

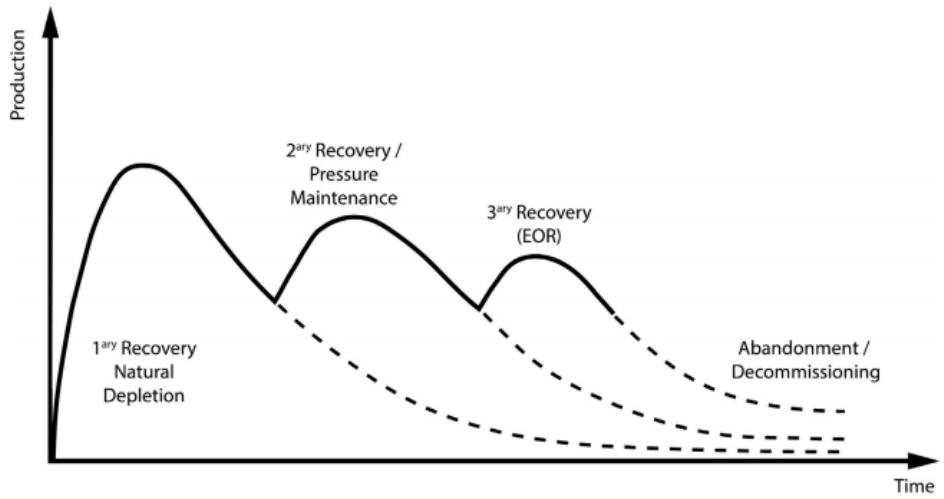

Figure 1.4: Production scheme as a function of time in an oilfield for the different recovery stages [13].

1.3. Enhanced Oil Recovery (*EOR*)

Enhanced oil recovery includes a series of actions during which the physical or chemical properties either of the fluids or the reservoir change with the aim of increasing the recovery.

The effectiveness of the enhanced mechanisms is often analyzed by looking at the recovery factor (*RF*), which stands for the ratio between the oil produced and the *OOIP* (both measured at surface conditions) [9].

$$RF = \frac{Cumulative\ oil\ produced}{Original\ Oil\ In\ Place} \tag{1.1}$$

Moreover, in case of secondary/tertiary oil recovery, it can also be defined as the product between the displacement efficiency (*ED*) and the volumetric sweep efficiency (*EV*) of the injected component:

$$RF = ED \cdot EV \tag{1.2}$$

where:

$$ED = \frac{Oil\ displaced\ by\ the\ injected\ component}{Oil\ contacted\ by\ the\ injected\ component} \tag{1.3}$$

$$EV = \frac{Oil\ contacted\ by\ the\ injected\ component}{Original\ Oil\ In\ Place} \tag{1.4}$$

Displacement efficiency expresses the efficiency of recovering mobile hydrocarbons [14] and depends on the initial conditions, the type and amount of displacing agent and also on rock properties [15]. Volumetric sweep efficiency expresses the efficiency of fluid recovery in terms of areal sweep efficiency and vertical sweep efficiency [14] and depends on the degree of heterogeneity of the rock properties (mainly permeability), mobility ratio, injection pattern and density difference between oil and selected component [16].

Equation (1.2) provides a simple way to calculate the recovery factor of a reservoir. However, there are several problems related to the factors involved, which depend on parameters or conditions unknown at the beginning, or during the exploitation. The incorrect consideration of any of them can lead to the failure of a project. In addition, during the *EOR* process, the injected fluids might affect more than one factor, in both positive and negative ways, thus rendering an accurate quantification of this almost impossible. Therefore, it is essential to know which is the phase

behavior in the chemical-oil-water system, considering the impact it has on all the parameters determining the oil recovery factor.

The production of the residual oil from the reservoir is achieved by application of various enhanced oil recovery (*EOR*) techniques [17]. Each of them employs one or more of the following concepts [18]:

- Increase the mobility of the displacement medium by increasing the viscosity of the water, decreasing the oil viscosity (or both simultaneously).
- Increase the oil recovery at a microscopic scale by means of using viscoelastic fluids, which displace in a more effectively way the oil trapped in the porous media.
- Extract the oil with a solvent.
- Reduce the interfacial tension (*IFT*) between oil and water and alteration of the reservoir rock wettability.

EOR techniques are majorly categorized as thermal, chemical, and miscible *EOR* and the selection of a particular method depends on the reservoir properties and subsurface conditions [19–21]. In the following map their classification is proposed Figure 1.5.

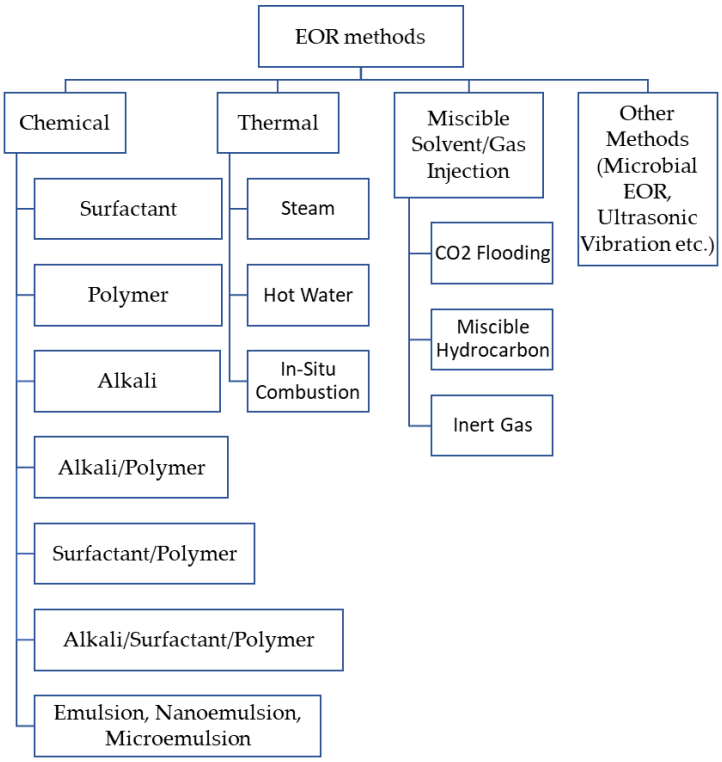

Figure 1.5: Classification of EOR methods [22].

Thermal Methods represent an important way to achieve good recovery in high viscous oil reservoir. Those processes are based indeed on the reduction of oil viscosity by means of thermal energy that is introduced into the reservoir. The improved physical characteristics of the oil allow it to flow more easily through the pores to reach the production wells. The principal thermal methods are Cycling Steam Stimulation (*CSS*) and steam drive. Other implemented processes are Steam-Assisted Gravity Drainage (*SAGD*), in-situ combustion, direct electrical resistive (*ER*) and electromagnetic radiation heating (*EM*) [23,24].

Chemical flooding methods act on one or more of the following factors: mobility (using viscosity-increasing water-polymer solutions), rock wettability and interfacial tension (*IFT*) (by adding surfactants and/or alkalis to the displacing agent) [25]. During polymer flooding, a viscous phase (polymer dissolved in water) is injected to increase the mobility of the oil phase toward the production well. In surfactant flooding, the purpose is to reduce the interfacial tension between the injected fluid and the fluid in place (oil). In alkaline flooding in particular, the surfactant is generated in-place from a chemical reaction between the injected alkali and naphthenic acids that are present in the reservoir oil. The three processes can also be combined in alkaline-surfactant-polymer (*ASP*) processes to simultaneously reduce the residual oil saturation and to ensure a good sweep efficiency.
Moreover, among the chemical flooding methods there are also foams and emulsions. The latter, and more specifically nanoemulsions, which are the object of the present thesis work, represent at the moment an innovative research topic. As a matter of fact, a unique scientific approved mechanism is not recognized yet for this technique, even if there are some accepted explanations of its behavior.

Miscible gas/solvent displacement processes are based on the miscible interaction between the injected gas and the oil in place. Usual choices for gas are carbon dioxide, flue gas, hydrocarbon solvents and nitrogen.

In the microbial injection, chemicals are generated in the formation by injection of microorganisms or nutrients to grow bacteria naturally present in the reservoir [5,26].

The purpose of the thesis is to understand the nanoemulsions key mechanisms of action used during the oil recovery process with the aim of developing a simulation workflow able to catch their behavior in porous media. The analysis starts from the description of nanoemulsion general formulation, which helps to identify the principal components acting during the oil mobilization and their physical and chemical characteristics. Then the laboratory experiments which represent the cases of interest for simulation are illustrated. The elaboration of the entire simulation workflow – performed using the STARS (CMG) simulator – has been explained in

detail starting from its application at laboratory scale. The built model is inspected through Global Sensitivity Analysis (*GSA*), which relies on the definition of a Polynomial Chaos Expansion (*PCE*) surrogate, to highlight the influence of each implemented parameter on Recovery Factor (*RF*) and Bottom Hole Pressure (*BHP*). Lastly the implementation at the field scale is performed with the construction of a sector model and a preliminary economic analysis.

2 Nanoemulsions overview

2.1. Composition and formulation

Emulsions are thermodynamically unstable, disperse multiphase systems of two or more immiscible liquids. They are formed by at least one continuous phase (outer phase) and one inner phase dispersed in droplets [27,28]. Most emulsions contain one aqueous phase conventionally indicated as "water", and one nonaqueous phase, generally the "oil".

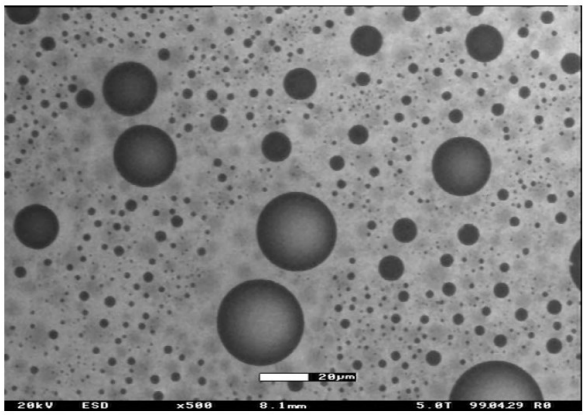

Figure 2.1: Environmental scanning electron microscopy image of squalene-in-water emulsion [29].

Emulsions can be classified according to the complexity of their structure and to the type of dispersed phase. In general, it is possible to distinguish:

- Normal or Simple emulsions, formed by one continuous phase and one dispersed phase. They can be oil in water (O/W) or water in oil (W/O) depending on whether the liquid droplets belong respectively to the oil phase or to the water phase (Figure 2.2 (a));
- Biemulsions, created in presence of a continuous phase and two different dispersed phases (Figure 2.2 (b));
- Multiple or Double emulsions whose structure is characterized by a continuous phase (the outer phase), a dispersed phase, which is an intermediate phase, and droplets of an additional inner phase that are spread across the intermediate one (Figure 2.2 (c)).

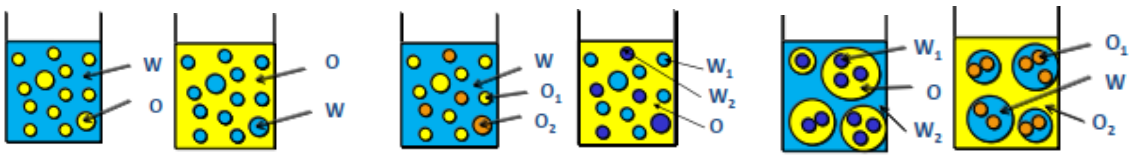

(a) Simple W/O and O/W emulsions. (b) O/W and W/O biemulsions. (c) $W_1/O/W_2$ and $O_1/W/O_2$ multiple emulsions.

Figure 2.2: Different types of emulsions.

When two immiscible liquids are placed in the same vessel, they are thermodynamically driven to minimize the contact area between the phases, forming two distinct layers [29,30]. Since the free energy of formation is positive, meaning that the increase in interfacial energy due to expansion of the interface is higher than the positive entropy of dispersion, an emulsion of the phases represents always a thermodynamically unstable system which formation is non-spontaneous [30] (Equation (2.1)):

$$\Delta G_{formation} = \gamma \, \Delta A - T \, \Delta S \gg 0 \tag{2.1}$$

where ΔA is the variation of the total surface area of dispersed particles and γ is the interfacial tension (*IFT*). Hence, $\gamma \, \Delta A$ is the amount of work required to form a new part of interface between two liquid phases [27].
The mixture of the two liquids is kinetically stabilized and forms a unique emulsified phase when mechanical energy is applied to the system in the presence of surfactants. During this process, termed homogenization, the two layers are broken, and mechanical dispersion occurs.

The preparation of an emulsion requires a sufficient mixing energy to spread one phase in the other one, creating additional surface area of the dispersed phase. Several procedures can be applied for emulsion formation. These can be classified mainly into two categories: high energy and low energy methods.
Among the high energy emulsification methods there are high shear stirring, high pressure homogenizers and ultrasound generators. These methods are highly demanding in terms of energy (~10^{10} W/kg) because the mechanical energy required for emulsification has to exceed the interfacial energy by several orders of magnitudes. This might pose an economical constraint for industrial purposes [31,32]. On the side of low energy methods (~10^{3} W/kg), the family of phase inversion processes is recalled. Phase inversion can be induced by changing either the composition at constant temperature (transitional phase inversion) or temperature at constant composition (phase inversion temperature method or *PIT*) [27,33,34].

PIT is based on the change of the system physical properties, starting from the preparation of a W/O emulsion at high temperature and then reducing it drastically below the *PIT* value to obtain a complete phase inversion (W/O emulsion) [32]. Additional details on emulsion preparation procedures can be found, e.g., in [32,35–37].

All of the preparation methods listed above require the presence of emulsifiers, that help to stabilize the suspension of one liquid within another one. In principle any compound that has the tendency to adsorb at the oil/water interface can be used. Nevertheless, surfactants are considered to be the main contributors to emulsion stabilization [38]. Surfactants (SURFace ACTive AgeNTS) are amphiphilic molecules formed by two parts, one hydrophilic and one hydrophobic (Figure 2.3) [29]. Due to their intrinsic structure, they are able to exhibit affinity for both polar and nonpolar substances at the same time. This characteristic brings them to place at the interface existing between the phases as shown in Figure 2.4. [31]. In this way the energy required to form a dispersion is reduced and emulsion breaking by coalescence is avoided. The effect of the alignment of those components on the interface is the reduction of the liquid interfacial tension, which constitutes one of the most important properties in the study of surfactants and related systems [31]. Still, the increase in surfactant concentration can saturate the free interface, thus pushing the emulsifier to migrate towards the solution inner part. These molecules are initially in the form of monomers. Above a certain concentration, denominated *C.M.C.* (critical micellar concentration), they tend to form aggregates known as micelles (Figure 2.4).

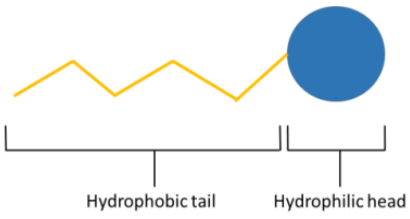

Figure 2.3: Surfactant molecule structure [31].

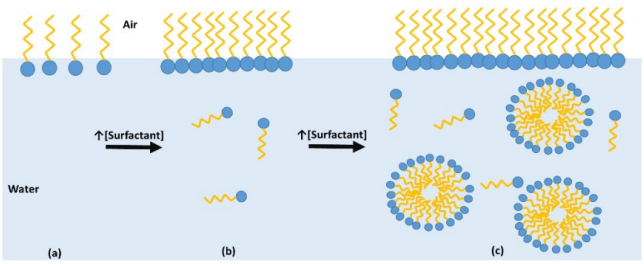

Figure 2.4: Process of micelle formation in aqueous phase [31].

Surfactants are characterized by the *HLB* (hydrophilic-lipophilic balance) parameter. The latter is an arbitrary scale indicating the tendency of the surfactant to solubilize in oil or water, and hence the tendency to form W/O or O/W emulsions. The scale ranges from 0 to 20. Low values correspond to hydrophobic surfactants with very long tails and little heads, while large values on the *HLB* scale indicate

hydrophilic surfactants with very large heads and short tales. In other words, surfactants with *HLB* < 6 are oil soluble and tend to form water-in-oil emulsions while if *HLB* > 8, surfactants are water soluble and will form oil-in-water emulsions [39]. The hydrophilic behavior of surfactants is due to the presence of polar functional groups, such as alcohols, ethers, esters, acids, and salts of carboxylic acids. Moreover, according to the nature of the charge of these groups, surfactants can be classified as cationic, anionic, non-ionic and zwitterionic.

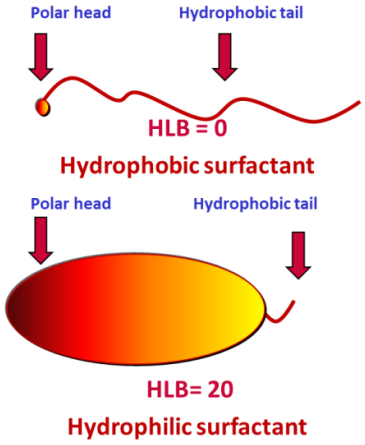

Figure 2.5: Characterization of surfactants according to *HLB* value.

In destabilizing conditions, emulsions may separate (or break) in various ways [28,38]:

- Sedimentation occurs when the droplets of dispersed phase sink to the bottom of the system due to their denser nature with respect to continuous phase. The larger the dimension of droplets, the more rapidly sedimentation occurs.
- Creaming appears when droplets of the dispersed phase, that is less dense than the continuous phase, float to the top of the system. It is the reverse process to sedimentation.
- Flocculation is a phenomenon that takes place when drops associate, without merging, forming larger "flocs" (aggregates). It is linked to van der Waals attraction forces that tend to exceed electrostatic repulsion forces when particles are within close proximity. The presence of these flocs structures enhances sedimentation or creaming.
- Coalescence is the process through which drops are pushed to merge forming larger ones. This could lead to eventual bulk separation of the phases given sufficient amount of time. In practice, stable emulsions show no tendency to coalesce over the duration of the experiment.

- Ostwald Ripening takes place due to the finite solubility of the oil phase in the aqueous phase. In fact, even if oils are referred to as immiscible with water, they often have very low solubility which can contribute to the breaking of emulsion. Smaller droplets will have a greater tendency to completely diffuse in water with respect to larger ones.

All these mechanisms are illustrated in Figure 2.6.

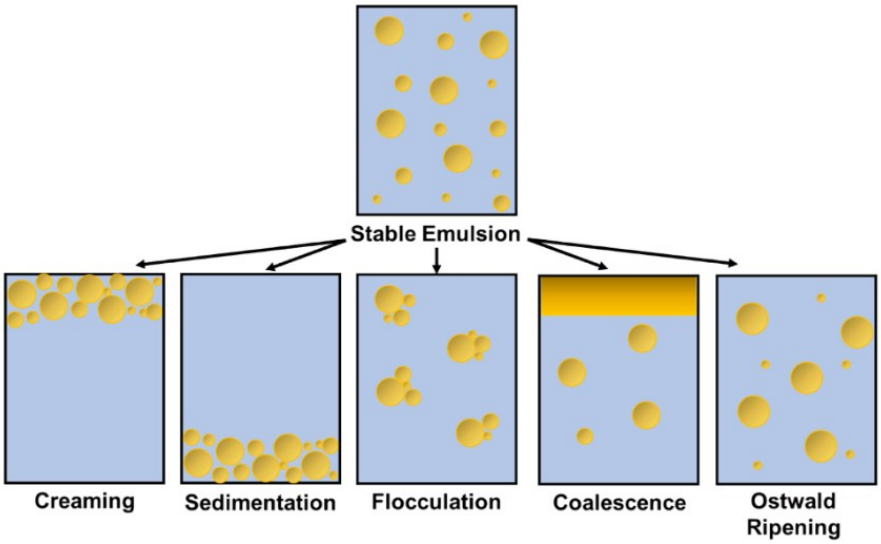

Figure 2.6: Diagram of creaming, sedimentation, flocculation, coalescence, and Ostwald ripening emulsion destabilization mechanisms [38].

A specific group of emulsions having a submicrometer droplet size is known as Nanoemulsions. Although no agreement exists in a drops size range to define them, most stated sizes in literature vary from 20 nm up to 500, 300, 200 or 100 nm [33]. These are kinetically stable colloidal systems that appear as translucent or transparent substances in opposition to macro emulsion that are optically opaque [40] (Figure 2.7).

Figure 2.7: Nanoemulsion (left) and macroemulsion (right) with droplet diameters of 35 nm and 1 μm, respectively [40].

They do not form spontaneously, and their characteristics and stability depend upon the preparation pathway which usually is performed in two steps. A macroemulsion is initially formed and it is then transformed into a nanoemulsion [34]. The functional aspects related to this technology are also influenced by the oleic component properties such as density, viscosity, interfacial tension value and refractive index [32,37]. For this reason, the selection of the proper solvent has been a relevant challenge as large volume of nanoemulsion slug is injected into the reservoir.

A major advantage in using nanoemulsion is that they are not subject to gravity-driven separation processes because of the small droplets size [27]. In fact, the Brownian motion and consequently the diffusion rate are higher than sedimentation (or creaming) rate induced by gravity. Ostwald ripening remains the main mechanism for nanoemulsion destabilization, as described by Tadros et al. [32,40]. The stabilization of nanoemulsion can be ensured also by the presence of polymers (and macromolecules) or solid particles. In these cases, they are not simply maintained by electrostatic repulsive forces of surfactant, but also by the steric hinderance effect of polymer chains. Moreover, polymer addition to the displacing fluid determines an improvement in rheological properties (viscosity and viscoelasticity) and a marked non-Newtonian behavior of the emulsion [37]. They also plug the high permeable zones, forcing the fluid to enter un-swept regions.

It is important to highlight that the formation of nanometric droplets is more difficult to attain than the formation of a macroemulsion and requires a larger amount of surfactants and/or energy [30]. Indeed, the average diameter of droplets is strictly correlated to surfactant presence and, in particular, to the solvent to surfactant ratio. As a matter of fact, at constant solvent concentration, a decrease in

surfactant concentration induces an increase in droplet size [41]. Smaller droplet size is indicative of a higher interfacial area, so it is expected that a greater amount of surfactants is needed to ensure a complete coverage [27]. For this reason, a deep understanding of nanoemulsion formation process is vital in controlling the droplet size of the system.

A more detailed description of emulsions structure and stabilization procedure is out of the scope of this thesis work.

2.2. Mechanisms of action

Several experiments demonstrate the effectiveness of nanoemulsions in enhanced oil recovery processes [31]. In order to assess the main mechanisms acting during oil recovery processes, it is important to keep into consideration the properties associated with this technology, as described in the previous paragraph [37]. When dealing with *EOR* performance analysis, the focus is on behavior at the microscale, concentrating mainly on mechanisms acting at the pore level [42].

The displacement promoted by this technology in porous media is based on different modes, that are similar to those of standard emulsions: reduction of interfacial tension between water and oil, wettability alteration of rocks, emulsification of trapped oil and mobility ratio improvement [31,37]. In addition to these mechanisms, the kinetic stability and improved rheological properties shown by nanoemulsions positively influence the oil recovery factor. An important factor which surely makes the difference with respect to standard emulsion is the high surface to volume ratio of the dispersed phase, that maximizes the interaction with the contacted fluids [42].

Emulsification and viscosity reduction of oil in place

The importance of mixing capability of nanoemulsions with other fluids (such as crude oil) has been studied by Kumar and Mandal [43] bringing to the conclusion that long term miscibility of crude oil with nanoemulsion is a desired property for better oil recoveries. The improvement of petroleum mobilization is ensured by the viscosity reduction obtained through the mixing of the low viscosity nanoemulsion solvent and the viscid oil in place. This process has been recognized as the 'solvent effect' [42]. On these bases, it is possible to state that the selection of a proper oleic dispersed solvent is of primary importance to attain enhanced emulsification of hydrocarbons.

Oil-water IFT reduction

Crude oil emulsification is possible thanks to the remarkable decrease in *IFT* at the interface of water and oil. In standard waterflooding the capillary number observed is very low ($10^{-7} – 10^{-6}$) [37] leaving an appreciable amount of petroleum due to high capillary forces withholding it. These forces are lowered by the interaction of the non-polar tails of surfactants with the oleic components, forming a film that is capable to reduce *IFT* by 40%, leading to an improvement in capillary number and to an easy mobilization of oil through capillaries [37].

Wettability alteration

The presence of surfactants has consequences not only on the value of *IFT* between liquid phases but also on another interfacial activity which involves the contact between liquid and solid: the wetting behavior. It is defined as the ability of a liquid to maintain contact with a solid surface, and it is controlled by the balance between the intermolecular interactions of adhesive type (liquid to surface) and cohesive type (liquid to liquid) [44]. Reservoir rock can show different wetting behavior depending on the type of formation and crude oil composition: oil-wet, intermediate-wet or water-wet. The aim of some *EOR* techniques involving wettability alteration is to change the behavior of the rocks from oil-wet to an intermediate-wet or even water-wet condition. This allows to reduce the adverse effect of capillary forces and detach the entrained oil thanks to the formation of a layer of emulsifier molecules on rock surface. Pal and Mandal recognized an enhanced wettability alteration capacity of nanoemulsion fluids on sandstone rocks with a reduction of the contact angle from 105° - 100° (non-wetting) to 9° - 6° (wetting) [45]. A similar result has been obtained by Kumar and Mandal [46] during the investigation of wettability alteration capability of non-ionic surfactants.

Numerous controversies exist about the predominance of one effect over the others, resulting from the fact that an accurate and precise expertise on the topic is not available at the moment. Indeed, different research groups have proposed contrasting theories on the mechanism driving recovery: as an example, Uchenna et al. [42] addressed the change in *IFT* to be the main process justifying nanomeulsion performance, Braccalenti et al. [47] indicated the solvent effect and the consequent viscosity reduction as responsible for improvement in *RF*, while Kumar and Mandal [48] attributed this enhancement to wettability modification.

Nanoemulsion injection is also beneficial when dealing with surfactant adsorption over the rock surfaces. Loss of surfactant in the reservoir is determinant to assess the economic viability of the surfactant-based flooding processes [49]. Nanoemulsions are capable to reduce it as the concentration of these components in the fluid is lower than the *C.M.C.*. This brings not only to a significant money saving but also to an improvement of the chemical carrying ability and blockage of

high permeable zones [37]. For this reason, knowledge of surfactant propagation and adsorption is key to design and development of this technology and could represent an improvement in its affordability.

During the analysis of nanoemulsions action in porous media it is important to keep in mind that they can show diverse rheological behaviors, including Newtonian fluid, non-Newtonian fluid (pseudo-plastic/shear thinning and dilatant/shear thickening) and viscoelastic fluid [50]. This tunable rheology can be controlled by the volume fraction of the dispersed phase, the droplets size, and the addition of viscosifying agents. Moreover, it also influences the seepage properties of nanoemulsions such as swept volume, pore blockage, migration and displacement efficiency.

2.3. State of the art and applications

Nanoemulsions, either oil-in-water or water-in-oil, have been recognized as promising technology for several industrial applications including chemical, pharmaceutical, food and oil and gas fields [31,37]. About the latter, they have been already applied for novel drilling, well completion, well remediation, well stimulation and formation fracturing, pipeline cleaning, oil tank and vessel cleanup and many others.

Concerning drilling process, nanoemulsions represent an advancement in deposit/mud removal, formation clean-up, scale inhibition and flow assurance thanks to their efficacy, achievable also with lower disposal volumes with respect to conventional methods [27,51]. Their use in wellbore cleaning has been triggered by the need to mitigate the challenges of the conventional chemicals (surfactants) in operation of oil and gas industry, such as the requirement of high turbulent flow and large volume together with the risk of formation contamination caused by unsuitable surfactants selection [37]. Nanoemulsions demonstrated an excellent cleaning efficiency when compared to conventional surfactant/detergents-based cleaning fluids on the basis of the mud removal efficiency (*MRE*).

A consistent number of studies have been conducted also on their application for production enhancement [52–54], and well stimulation, highlighting the huge success obtained by their use as cleanup additives in fracturing operations, allowing an easier flow-back of fracturing fluids.

The investigations in chemical *EOR* field suggested the possible employment of this technology to mobilize the residual crude oil after primary and secondary recovery. McAuliffe firstly encouraged emulsion application in light of the fact that surfactant flooding is made uneconomical by the loss of costly surfactants due to adsorption

over the rock surface, polymer flooding promotes pores/capillaries plugging leading to the creation of low permeable zones and Alkali-Surfactant-Polymer (*ASP*) flooding brings to scale formation polluting the oil. Deeper studies on this topic underlined that poor emulsion stability, which made them unsuitable for flooding, could be solved by nanotechnology. In particular, properly designed nanoemulsions are able to reduce *IFT* much lower than conventional emulsions, enhance wettability of the rock and solubilize large quantities of hydrocarbons, ensuring a better injectivity without phase separation due to the nanometric size of the droplets [37].

In this context, *EOR* applications of nanoemulsion is still at the beginning of its path, being investigated almost exclusively with laboratory experiments. Literature on nanoemulsion based *EOR* is not very rich [42,47,48,55–64], with the nearly complete absence of simulation works on the topic. In this context, the present thesis aims at blazing a trail in simulation of nanoemulsion *EOR* processes, providing a first approach to their modeling which can be possibly improved by future studies.

2.3.1. Challenges and future prospects

Currently, Nanoemulsions do not represent a mature technology and require a deeper global understanding together with relevant improvements to face challenges that are still evolving. For this reason, their application in oil industry is yet in research phase, where all the efforts are directed to overcome the existing limits to achieve successful operations. Some of the issues that are delaying their employment on field are here listed [37]:

- Stability in different reservoir environments: this is a crucial aspect influencing the effectiveness of nanoemulsions in field operations. The stability of emulsion could vary according to the type of environment in which it is injected, hence a suitable composition and preparation procedure should be applied. This can be done only after a precise study on the interaction between the nanoemulsion constituents and the reservoir environment which is lacking at the time.
- Recovery mechanisms understanding: this element represents the basis of simulation workflow and possible future improvements of this technology, therefore it is vital to learn more about the topic since the knowledge in this field is still at an early stage.
- Economic viability: there are differing opinions on the hypothetical advantage brought by nanoemulsion in economic terms. On one side a rational formulation of this particular fluid allows to reduce the concentration of really costly elements (such as solvent and surfactants) with respect to conventional chemicals. Otherwise, an expensive and specialized

equipment must be used for the preparation together with a consistent energy input. A series of laboratory tests on this matter have been carried out by Del Gaudio et al. [41].

- Environmental impact: the effect of this technology on health and environment is still unknown due to its novelty in the oil and gas field. The dominant concerns about the use of nanoemulsions in reservoir regard groundwater pollution with consequent effects on vegetation and living organisms.

3 Experimental campaign

In this chapter the general experimental workflow adopted by Eni is described with reference to nanoemulsion technique testing at the laboratory scale.

The *EOR* study and application process adopted by Eni is structured across various parallel activities among which the most important for the purpose of this thesis are laboratory experiments and simulation analysis. The parallel approach in an *EOR* technology application allows reducing costs and time with respect to a sequential one. The critical steps encountered during the assessment of technology efficacy are two: laboratory analysis and simulations. Moreover, establishing a cooperation between the two parts is of huge importance because it ensures, on one side, to have the right and updated input data coming from the laboratory, and, on the other side, to guide the experimental campaign in the tests and measures to be performed for the determination of all the parameters, required within the simulation. The fundamental importance of this cooperation between activities must be underlined in light of the observation that the present work represents a pioneering study of nanoemulsion *EOR* simulation.

In order to analyze the potential effectiveness of this technology, several flooding tests have been planned, consisting of two different phases: the first one involves coreflooding tests with slim tubes filled with crushed Berea and saturated oil, with the aim of evaluating the outgoing phases with respect to the injected formulation and the efficiency of displacement of the nanoemulsion slug, to obtain the highest oil recovery. In addition, the slim tube analyzes the behavior of nanoemulsion at long distances from the point of injection. The second phase involves flooding tests with reservoir oil plugs, to evaluate the injectivity of the nanoemulsion selected through the first phase and to optimize the efficiency of nanoemulsion formulation in terms of oil recovery. The plug tests analyze the nanoemulsion behavior in the near wellbore zone. In this thesis work two experiments are posed under study, one belonging to the first phase, one to the second.

The general coreflooding experimental workflow is summarized in Figure 3.1.

Figure 3.1: General coreflooding experimental workflow.

3.1. Field selection for nanoemulsion *EOR* application

The application of nanoemulsion injection follows the typical workflow adopted by Eni to develop an *EOR* project. First, there is the screening phase, during which a specific field is selected and an *EOR* technique is chosen to be evaluated. Then, laboratory analyses are performed, consisting of rock and fluid characterization, displacement tests on core plugs and determination of the principal input parameters for the following simulation phase. The reservoir simulations aim to interpret the results coming from the previous activities representing a selected area of the chosen field through sector modelling and to perform forecast scenarios with the purpose of understanding if the selected *EOR* technique can bring possible benefits when applied. If the *EOR* technique results effective in the performed reservoir simulations, field tests are proposed [65]. The field tests are the Single Well Chemical Tracer Test (*SWCTT*) and the Pilot inter-well test. The former is a widely applied test to measure the residual oil saturation after waterflooding and a subsequent *EOR* process. In the *SWCTT* an ester is injected into a selected well and it partially reacts with water to form an alcohol (hydrolysis reaction). Then, the well is switched to production mode and the concentration of produced ester and alcohol are measured. Since the ester partitions into oil and water while alcohol is only present in the water phase, the residual oil can be deducted, if the partition coefficient is known, from the relative arrival times of the ester and alcohol [66]. The Pilot inter-well test consists in the injection of the *EOR* technology through an injector well and monitor the connected producers. If positive results are encountered with the field tests, the *EOR* technique is designed to be applied on a full-field scale.

The Beta field, a reservoir located in North Africa, is selected during the screening phase for the application of the nanoemulsion technique. Note that the activity conducted on slim tube is a pioneering test aimed at assessing the feasibility of nanoemulsion *EOR* specifically on Beta field, while the plug test is not referred to the same application.

3.2. Plug application

The first experiment taken into consideration was carried out in 2017 by Del Gaudio et al. [47]. Their goal was to evaluate the effectiveness of the nanoemulsions as displacing fluid for enhanced oil recovery and to investigate the mechanisms of mobilization of the residual oil in comparison with the classical chemical *EOR* methods.

3.2.1. Fluid data

Water

Brine A is chosen to approximate the specific field conditions. It is characterized by a salinity level that is listed in Table 3.1.

NaCl [mg/l]	64500
$CaCl_2$ [mg/l]	14100
Salinity as NaCl [mg/l]	77300

Table 3.1: Brine A salinity.

Oil

The properties of the crude oil used for the experiments are summarized in Table 3.2.

°API	Asphaltenic	Viscosity @ RC [cP]	Density @ 77°C [g/ml]
12.5	highly	23	0.9158

Table 3.2: Crude oil characteristics.

Note that the viscosity listed in Table 3.2 refers to the live oil condition; in the case of dead oil its value corresponds to 64 cP when the temperature is 77°C (reservoir temperature).

Nanoemulsion

For this particular application, the nanoemulsion has been prepared using 8% of Xylene as organic phase, a surfactant package containing 4 commercial surfactants (at different concentrations) and brine, as reported in Table 3.3.

Phase	Brine (continuous phase)	Solvent (dispersed phase)	Surfactants
Name	Brine A	Xylene	Glucopon 600, Atlox 4913, Span 80
Concentration	87.01%	8%	4.99%

Table 3.3: Nanoemulsion composition.

3.2.2. Coreflooding experimental setup

The core flooding experimental apparatus is depicted in Figure 3.2. It consists of three main sections: (i) pumps for fluids injection, (ii) a core holder and (iii) an effluent collector system.

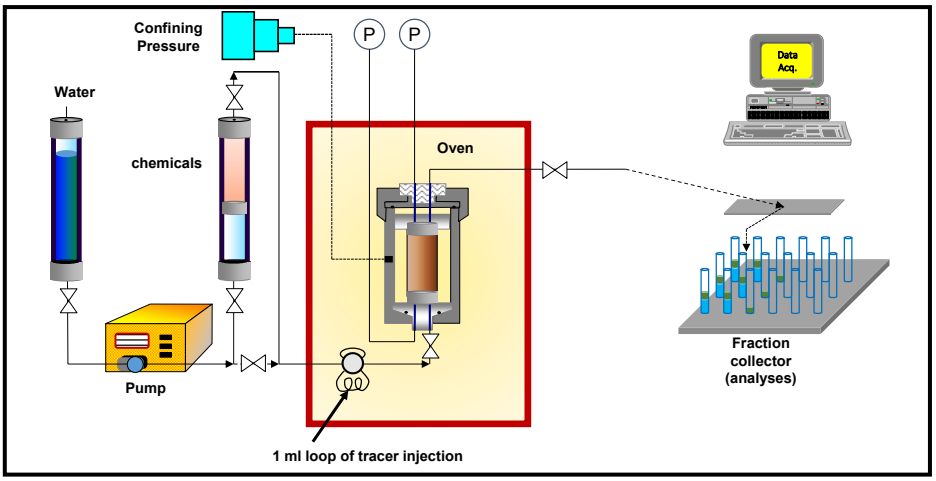

Figure 3.2: Core flooding experimental apparatus.

Pumping system

The pumping system consists of two piston pumps (Figure 3.3). The upper one is used to pump water, the lower one is used to pump the nanoemulsion. An additional water pumping system is used to apply the confining pressure to the core. The pumped flow rate accuracy is ± 1% of the set point.

Figure 3.3: Pumping system.

Sample

The sample is placed in an oven to mimic the reservoir temperature, inserted in a hassle-type core holder set under pressure by the confining pressure line.

Two tubes, representing the injection and production endpoints, are connected at the bottom and at the top of the sample, respectively. Two other tubes, related to pressure transducers (P circled in Figure 3.2), are connected to the sample as the previous ones. The pressure transducers accuracy is ± 0.5% of the full scale (40 bar at the inlet and 2.5 bar at the outlet).

Effluent collection system

During the core flooding test the effluents are automatically collected from the outlet tube in the effluent collector system, characterized by a set of test tubes. On the outlet line, before the effluent collection system, a heater is used to prevent the oil clamping in the line. The collection frequency is defined in minutes and in fraction of pore volume. By performing the collection in this way, it is possible to define a more accurate recovery curve. The effluent collection system is illustrated in Figure 3.4.

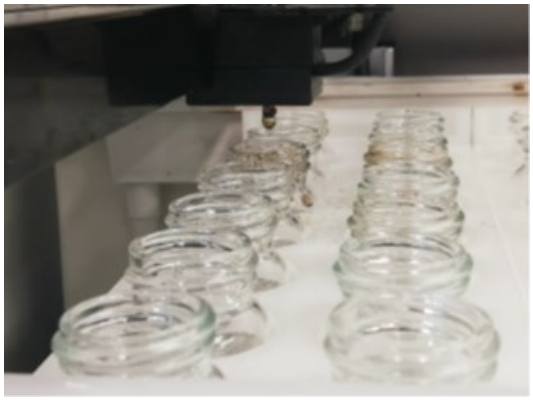

Figure 3.4: Effluent collection system.

3.2.3. Core preparation and installation

The test has been carried out on a Berea sandstone plug whose characteristics are listed in the following table.

Length [cm]	Diameter [cm]	Porosity [%]	Permeability [mD]	Pore volume [ml]
9.72	5.01	22.56	360	43.508

Table 3.4: Core sample characteristics.

The preliminary phase to a flooding test is the core preparation that is aimed at reproducing ideally the reservoir conditions in terms of initial oil saturation. It proceeds with brine saturation (injecting water to fully saturation (100%)), following brine displacement with oil until initial water saturation conditions (S_{wi}) and a following ageing phase. The initial water saturation for this case is estimated

as 27.2%. The ageing phase consist of placing the plug in the reservoir oil for a period of four weeks to reproduce as best as possible the original reservoir wettability. After the ageing period, the core is cleaned superficially, and it is ready to be mounted on the core holder.
The installation is then performed with the use of a bench clamp, by covering the core with a rubber sleeve in which it is inserted, starting from the bottom and following the same direction of the flooding done during the preparation phase.

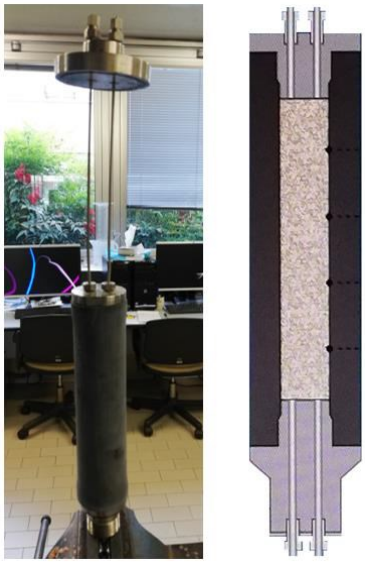

Figure 3.5: Core covered with rubber sleeve.

Then the top head is attached, and the core is fixed in the hassler-type core holder. The gap between the sleeve and the core holder inner wall is filled with distilled water or gas as illustrated in Figure 3.6.

Figure 3.6: Core holder fixing.

At the end the core is placed in the oven, where it is subjected to a confining pressure of 40 bar that makes it ready for the flooding.

Figure 3.7: Core positioning in the oven.

The saturation and ageing processes go in parallel with the weight check procedure, which is needed to assess the petrophysical properties of the core. In this context, the effective permeability calculation is executed through the use of Darcy law, knowing the geometrical features of the sample and the pressure drop across it as reported in Equation (3.2).

$$q = \frac{kA}{\mu}\frac{\Delta P}{L} \tag{3.1}$$

From Equation (3.1) it is possible to obtain k:

$$k = \frac{q \cdot \mu \cdot L}{A \cdot \Delta P} \tag{3.2}$$

3.2.4. Test execution and calculations

Once the plug has been prepared, the standard fluid injection sequence has been followed to carry out the experiment in tertiary mode:

1. Brine injection (~80 PV[2]; 0.7 ml/min);
2. Nanoemulsion injection (0.3 PV; 0.7 ml/min);
3. Brine Injection (0.7 ml/min).

It is important to highlight the complexity of the switch between different solutions which is carried out by operating the respective pumps and valves, paying attention

[2] PV = Pore Volume, part of the internal void volume of a porous material occupied by oil in place.

to reduce as much as possible the destabilization of the system that may be triggered by dead volumes, pressure oscillations and lag times.

As flooding proceeds, effluents are collected in test tubes and analysed to determine the quantity of oil present in each of them. The total mass of oil is then computed considering the sum of the produced oil and the residual one extracted from the core through a cleaning procedure made with toluene and methanol. This value is critical to obtain a reliable value of the recovery factor at the end of the coreflooding procedure.
The total recovery factor (RF_{Total}) can be calculated considering the sum of the contribution of the oil recovered after water flooding and the oil recovered after nanoemulsion flooding displacement process.

As a consequence, to isolate the contribution of nanoemulsion on oil recovery, the results have been expressed as follows:

$$\Delta RF\ (\%) = RF_{Total}(\%) - RF_{wf}(\%) \tag{3.3}$$

where RF_{Total} is the overall cumulative recovery factor and RF_{wf} is the recovery factor associated to the water flooding.

In addition, the Bottom hole Pressure is recorded considering pressure signals coming from the transducers located at the inlet and at the outlet of the sample. The pressure at the outlet of the sample is set at a constant value of 1 bar (atmospheric pressure).

3.2.5. Results

The computed RF and the ΔP recorded during the experiment are illustrated in Figure 3.8. As can be noted, the recovery factor curve presents a fast increase in the initial part that is related to water flooding. The rising trend slows down after roughly 10 PV, bringing to a waterflooding recovery of 63.6%. This value is useful for the calculation of Residual Oil Saturation (S_{or}) according to:

$$RF = \frac{S_{oi} - S_{or}}{S_{oi}} \tag{3.4}$$

$$S_{or} = S_{oi} - RF \cdot S_{oi} = 0.265 \tag{3.5}$$

where S_{oi} is computed as $1 - S_{wi}$.

The effect of the nanoemulsion becomes clear after 81 PV when the recovery experiences a steep growth. Looking at the pressure chart, this moment is highlighted by a peak reaching 2.1 bars.

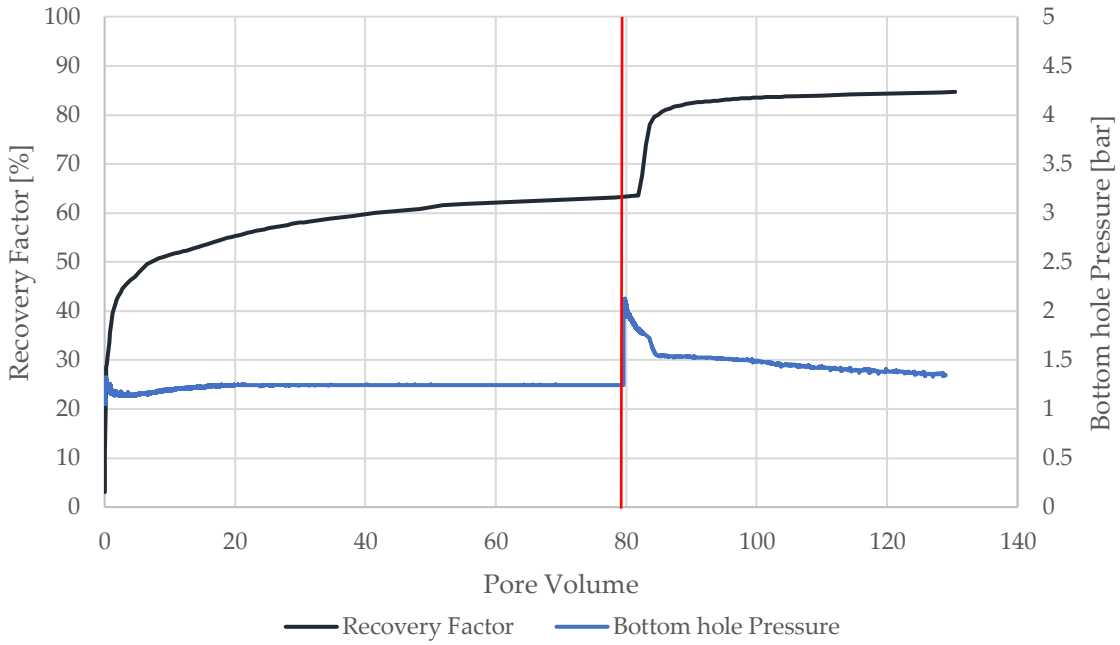

Figure 3.8: Experimental results for Recovery Factor and Bottom hole Pressure.

Following the flooding of the nanoemulsion, an additional oil recovery (~21%) was achieved (as compared against the water flooding). This result is consistent with what observed and reported in literature for conventional chemical *EOR* processes, i.e., polymer flooding (8-10%) and surfactant flooding (20-40%).

System	RF_{Total} [%]	RF_{wf} [%]	ΔRF [%]
Nano A	84.67	63.6	21.07

Table 3.5: Recovery results from flooding experiment.

3.3. Slim tube application

The goal of this experiment was to verify the composition of the outgoing phases with respect to the injected formulations and the contribution of the displacement of the nanoemulsion slug to yield the highest oil recoveries.

3.3.1. Fluid data

Water

The synthetic water employed in this test is a laboratory product used both for the waterflooding phase and for the formulation of the nanoemulsion. To prepare the synthetic injection water the carbonate and sulphate anions have been excluded to avoid having insoluble precipitates during the test. The brine composition is listed in Table 3.6.

NaCl [mg/l]	9410
$CaCl_2$ [mg/l]	3050
KCl [mg/l]	151
$MgCl_2$ $6H_2O$ [mg/l]	1825
Equivalent salinity as NaCl [mg/l]	13789.66

Table 3.6: Brine salinity.

Oil

Due to the lack of reservoir oil in the laboratories, it was decided to use an analogue. For this reason, a deep analysis has been conducted to select the potential oil suitable for coreflooding purposes.

The research of the analogue oil to be used was carried out by setting the following as parameters of comparison:

- °API,
- Reservoir temperature (Tres),
- Molecular weight (MW),
- Composition,
- Viscosity at ambient pressure and reservoir temperature (μ @Pamb, Tres).

Parameter	Field Oil	Test Oil
Tres [°C]	112.8	75
Pres [bara]	384.38	252.62
°API	40	40.6
μ_{oil} @Pamb, Tres [cP]	1.55	2.2
MW [g/mol]	74.66	73.35

Table 3.7: Oil characteristics comparison.

Nanoemulsion

For this flooding tests, synthetic brine has been selected as continuous phase in which the solvent Solvesso 150 is dispersed. The surfactant package utilized for solvent droplet stabilization is composed by 4 commercial surfactants: Glucopon

600, Span 80 and Zephrym (ex Atlox) 4913. Nanoemulsion formulation is summarized in Table 3.8.

Phase	Brine (continuous phase)	Solvent (dispersed phase)	Surfactants
Name	Synthetic brine	Solvesso 150	Glucopon 600, Zephrym 4913, Span 80
Concentration	88.346%	8%	3.654%

Table 3.8: Nanoemulsion composition.

3.3.2. Slim tube experimental setup

The experimental setup used in this case is very similar to the one used for the flooding test on core (Figure 3.2) described in Section 3.2.2. The innovative aspect of this test is the employment of a slim tube instead of a core. A slim tube is a 2 m long aluminium duct filled with unconsolidated Berea sand in the range 75-160 micron. Given its length, that makes it impossible to keep it vertically extended, the slim tube is wrapped in large coils and inserted into the oven where it is held at a constant temperature of 90°C.

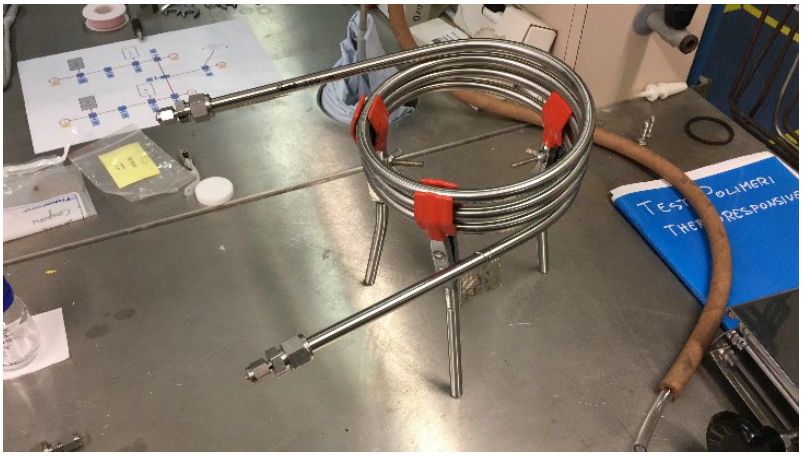

Figure 3.9: Slim tube aluminum duct.

No confinement pressure is applied because of the difficulty in maintaining it constant during the whole experiment.

The principal characteristics of the tube are summarized Table 3.9.

Length [cm]	External diameter [cm]	Internal diameter [cm]	Tube volume [ml]	Porosity [%]	Pore volume [ml]	Absolute Permeability [mD]
200	0.953	0.77	94.2	41	38.62	2900

Table 3.9: Slim tube characteristics.

3.3.3. Slim tube preparation and installation

The procedure followed to carry out the trial is illustrated in Figure 3.10.

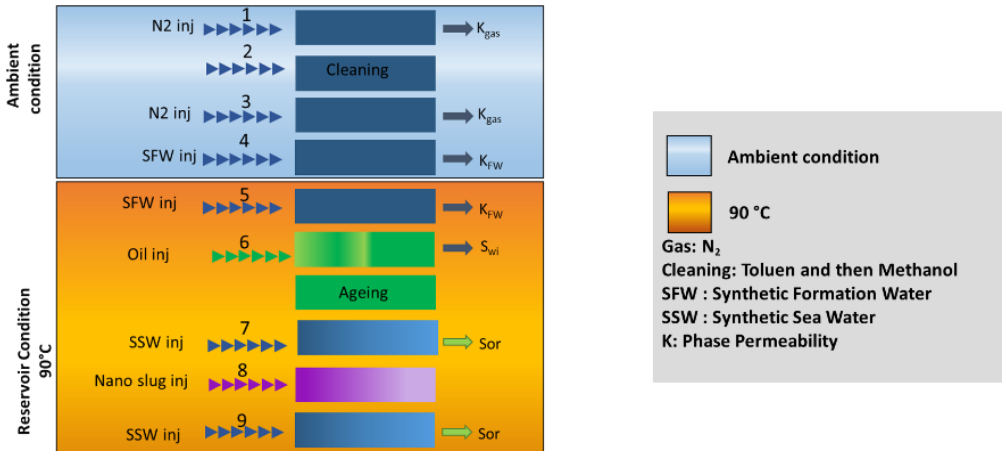

Figure 3.10: Experimental workflow followed during flooding in slim tube.

Preparation of the slim tube for the flooding starts with N_2 injection. The latter has a dual purpose, corresponding to sand drying and determination of gas permeability. In this case, brine saturation is attained twice, first at ambient and then at reservoir temperature. The value of effective permeability to water computed through Darcy's law is obtained from the second flushing as:

$$q = \frac{kA}{\mu}\frac{\Delta P}{L} \tag{3.6}$$

Knowing the slim tube geometric parameters, the pressure drop across the tube (1.5 bar) and the water viscosity (0.28 cP), from Equation (3.6) it is possible to obtain the value of gas permeability:

$$k = 677\ mD \tag{3.7}$$

The slim tube preparation phase is then concluded with brine displacement by mean of oil injection, through which the value of S_{wi} has been estimated (S_{wi} = 38%). This last step is followed by 40 days ageing in the oven at 90°C aimed at obtaining the most reliable reproduction of the original system in reservoir.

In contrast to what explained for the core case, the slim tube is not inserted in a rubber sleeve and is placed in the oven without any confining pressure.

Figure 3.11: Coiled slim tube inside the oven.

3.3.4. Injection procedure

The injection procedure consists of:

1. water is firstly flooded into the tube at 0.5 ml/min to reproduce secondary recovery until no more oil is produced.
2. Afterward a nanoemulsion slug corresponding to 1/3 of the total pore volume is injected at the same rate and lastly chase water is used to clean the tube from eventual residuals before calculating again the final S_{or} value.

The bottom hole pressure and oil recovery data are collected as previously discussed and are reported in Figure 3.12.

3.3.5. Results and discussion

As shown in Figure 3.12, the recovery factor curve displays a steep slope at the beginning of waterflooding that tends to stabilize around a value of 73% in less than 1 PV. At this state the S_{or} value is found to be equal to 0.17.

The plateau that starts from this point, continues until nanoemulsion effects become appreciable, i.e., roughly 1 PV after injection. The curve then starts again to smoothly increase until it reaches the maximum value of 88.44%. Oil recovery due to the injection of nanoemulsion slug is about 16%. Table 3.10 summarizes the *RF* obtained during the slim tube flooding.

RF_{wf} [%]	RF_{Total} [%]	ΔRF [%]
72.58	88.44	15.86

Table 3.10: Recovery results from flooding experiment.

Pressure is stable during the water injection; then, it is perturbed by the arrival of the nanoemulsion which is able to move the oil in a more efficient way with respect to water. This causes a strong increase in pressure, attaining a value of about 10 bars, stabilizing at about 8 bars after 4 PV.

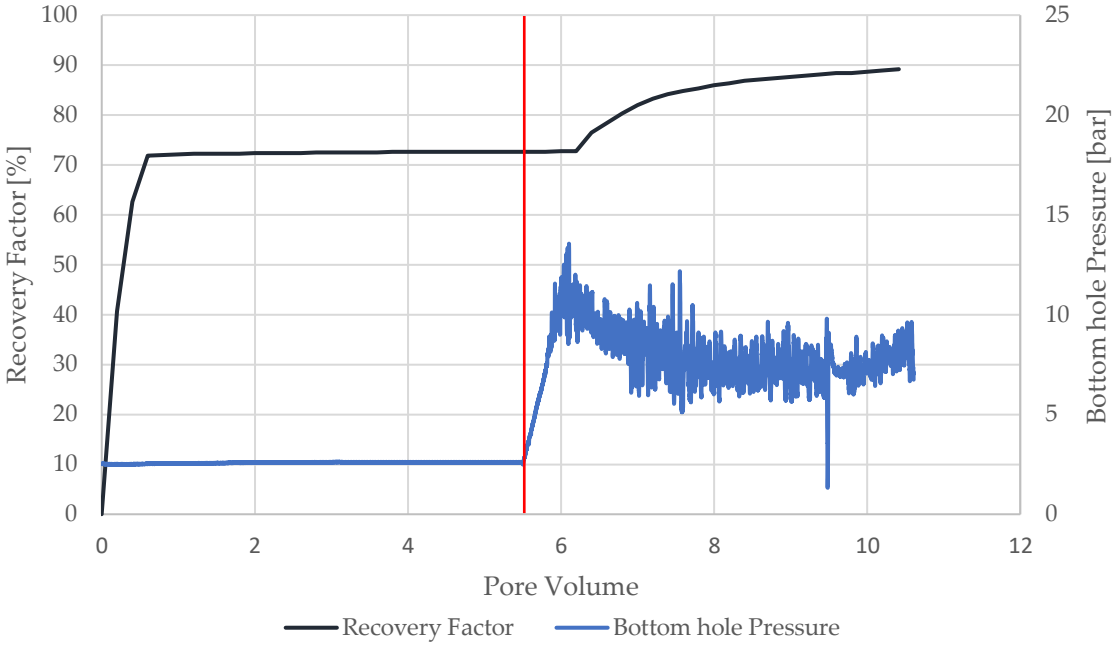

Figure 3.12: Experimental results for Recovery Factor and Bottom hole Pressure.

4 Simulation workflow

4.1. Choice of the simulator

The application of simulation tools to fluid flow across porous/fractured reservoirs has been applied in oil and gas industry since the 1950s [21].

It is of primary importance to assess the efficacy of new/advanced *EOR* techniques through experimental modelling activities prior to their implementation in field applications. Preliminary experimental investigations act as input data for simulator; the following laboratory experiments simulation help interpreting the achieved results in terms of rock-fluid interactions during fluid flow through porous media, oil recoveries and effectivity of different *EOR* methods providing an insight about the relevance of the selected injecting fluid and determination of parameters required for upscaling at field/reservoir level [67–75].

Despite reservoir simulators are widely used, it is appropriate to state that the porous media structure and the flow through it are impossible to describe, leading to a marked degree of uncertainty behind the results a given software provides [76].

Industries nowadays are engaged in employing reservoir simulators such as ECLIPSE by Schlumberger (SLB), UTCHEM by University of Texas (UT Austin), REVEAL by Petroleum Experts (Petex), VIP (Landmark, Halliburton), IMEX and STARS by Computer Modelling Group (CMG) which accurately/realistically predict the chemical flooding processes [68,77].

The simulation tool selected to model the nanoemulsion experimental activity is STARS (Steam, Thermal and Advanced processes Reservoir Simulator) by CMG. It is a three-phase advanced simulator known for its ability to model both laboratory and field scale applications while also having the capability to handle complicated chemical behavior [69,77,78].

4.2. Mathematical model and conservation equations

CMG STARS is a finite difference numerical simulator that describes mathematical equations for fluid flow in a petroleum reservoir. It solves a set of conservation

equations, consisting of material balance equations, flow equations, chemical reactions, heat exchange equations and phase equilibrium equations [79]. The mathematical model is structured as follows: one conservation equation is implemented for each chemical component for which a separate accounting is desired, along with some equations describing phase equilibrium between phases. A set of such equations is applied for each region of interest, which is usually a discretized grid block. An equation describing the operating conditions of each injection and production well is also included [78].

The basic governing equations relate the conservation of mass and energy for the elementary volume of the region of interest, where the change for each component in the volume is related to the fluids entering and leaving the volume [80,81]. The principle of conservation states that the accumulated quantity within a region depends on the rate of net-inflow and net-outflow according to:

$$R_{change,acc} = R_{net\ inflow,adj\ reg} + R_{net,add} \tag{4.1}$$

where:

- $R_{change,acc}$ = Rate of change of accumulation
- $R_{net\ inflow,adj\ reg}$ = net rate of inflow from adjacent regions
- $R_{net,add}$ = net rate of addition from sources and sinks

The governing conservation equation is applied for each component along with the energy of the system. The mass conservation equation for component i is defined as:

$$\begin{aligned}\frac{\partial}{\partial t}[V_f(\rho_w S_w w_i + \rho_o S_o x_i + \rho_g S_g y_i) + V_v A d_i] \\ = \sum_{k=1}^{n_f}[T_w \rho_w w_i \Delta\Phi_w + T_o \rho_o x_i \Delta\Phi_o + T_g \rho_g y_i \Delta\Phi_g] \\ + V \sum_{k=1}^{n_r}(s'_{ki} - s_{ki})\, r_k \\ + \sum_{k=1}^{n_f}[\varphi D_{wi} \rho_w \Delta w_i + \varphi D_{oi} \rho_o \Delta x_i + \varphi D_{gi} \rho_g \Delta y_i] \\ + \rho_w q_{wk} w_i + \rho_o q_{ok} x_i + \rho_g q_{gk} y_i + \delta_{iw} \sum_{k=1}^{n_f} \rho_w q a q_{wk}\end{aligned} \tag{4.2}$$

where $\frac{\partial}{\partial t}[V_f(\rho_w S_w w_i + \rho_o S_o x_i + \rho_g S_g y_i) + V_v A d_i]$ is the accumulation term for a flowing and adsorbed component i, with V_f representing the total fluid volume and V_v the void volume. w_i, x_i and y_i refer to mole fraction of component i in water, oil, and gas respectively, whereas ρ and S stand for density and saturation of different phases. $V\sum_{k=1}^{n_r}(s'_{ki} - s_{ki})\, r_k$ is the reaction source/sink term for component i, in which r_k is the volumetric rate of reaction k, s_{ki} and s'_{ki} are reactant and product stoichiometric coefficient of component i in reaction k. In addition, $\rho_w q_{wk} w_i + \rho_o q_{ok} x_i + \rho_g q_{gk} y_i$ is the well source/sink term for the flowing component i. In those terms quantity q_{jk} is the well rate of phase j in layer k. $\sum_{k=1}^{n_f}[T_w \rho_w w_i \Delta\Phi_w + T_o \rho_o x_i \Delta\Phi_o + T_g \rho_g y_i \Delta\Phi_g] + \sum_{k=1}^{n_f}[\varphi D_{wi} \rho_w \Delta w_i + \varphi D_{oi} \rho_o \Delta x_i + \varphi D_{gi} \rho_g \Delta y_i]$ is the flow term for the flowing component i, where T is the transmissibility of the component between two regions, which accounts for cross sectional area, distance between the elementary volumes and fluid permeability. Moreover, it is related to the volumetric flow rate v as follows:

$$v_j = T\left(\frac{k_{rj}}{\mu_j r_j}\right)\Delta\Phi_j \qquad j = w, o, g \tag{4.3}$$

where, k_{rj} is relative permeability, r_j is the phase resistance factor and μ_j is the viscosity of the phase j. $\Delta\Phi_j$ is the potential difference of phase j and its positive or negative value corresponds to the inflow or outflow from the elementary volume. D_{wi}, D_{oi}, and D_{gi} are the respective dispersibility of the component in water, oil, and gas phases. The term $\sum_{k=1}^{n_f} \rho_w q a q_{wk}$ corresponds to a source/sink term for the water component where $q a q_{wk}$ represents the volumetric water flow rate through a block face to/from the adjacent domain.

Energy conservation is written as:

$$\begin{aligned}\frac{\partial}{\partial t}[V_f(\rho_w S_w U_w + \rho_o S_o U_o + \rho_g S_g U_g) + V_v c_s U_s + V_r U_r] \\ = \sum_{k=1}^{n_f}[T_w \rho_w H_w \Delta\Phi_w + T_o \rho_o H_o \Delta\Phi_o + T_g \rho_g H_g \Delta\Phi_g] \\ + \sum_{k=1}^{n_f} K\Delta T + \rho_w q_{wk} H_w + \rho_o q_{ok} H_o + \rho_g q_{gk} H_g \\ + V \sum_{k=1}^{n_r} H_{rk}\, r_k + \sum_{k=1}^{n_r} HL_k + HL_v + HL_c \\ + \sum_{k=1}^{n_f} (HA_{CV} + HA_{CD})_k\end{aligned} \tag{4.4}$$

Here $\frac{\partial}{\partial t}[V_f(\rho_w S_w U_w + \rho_o S_o U_o + \rho_g S_g U_g) + V_v c_s U_s + V_r U_r]$ is the term related to energy accumulation, in which $U_j, j = w, o, g, s$ is the internal energy as a function of temperature and phase composition, U_r is the energy per rock volume and c_s is the total solid concentration. $\sum_{k=1}^{n_f}[T_w \rho_w H_w \Delta\Phi_w + T_o \rho_o H_o \Delta\Phi_o + T_g \rho_g H_g \Delta\Phi_g] + \sum_{k=1}^{n_f} K\Delta T$ is the energy term for flow between two regions, where H_j denotes the enthalpy of the respective phase. $\rho_w q_{wk} H_w + \rho_o q_{ok} H_o + \rho_g q_{gk} H_g$ is the well source/sink term for energy while HL_k, HL_v, HL_c represent the total heat transfer rate from adjacent formation, heat transfer rate calculated from a convective model and constant heat transfer model respectively. The chemical reaction source/sink term for energy is $V \sum_{k=1}^{n_r} H_{rk}\, r_k$ where H_{rk} is the enthalpy of reaction k. The last term is referred to as thermal aquifer sources/sinks, HA_{CV} and HA_{CD} are the rates of heat transferred by convection and conduction to/from the adjacent aquifer.

Apart from the basic conservation equations, STARS employs additional equations to generate relative permeability curves, to account for alterations of rock-fluid interaction and to model solvent injection processes by using solubility equilibrium values (K values). They will be presented in the following paragraphs.

With an appropriate set of initial/boundary conditions, the governing models are applied to develop an understanding of simultaneous flow of two or more fluid phases.

4.3. Core flooding simulation

The experimental simulation study includes the precise description of volumetric dimensions, fluid compositions, fluid flow through porous media and water/oil saturation [82–85]. The first step of the modeling part is to create a simulation grid reproducing the core sample. To do this, a series of assumptions has been made to simplify the problem:

- A two-phase system is considered, comprising water and crude oil with no presence of gas phase.
- The sample is portrayed to be homogeneous without any geological heterogeneity.
- Flow of fluids in radial direction is negligible in comparison to the flow in the axial direction of the core (1-D model).
- The fluids are considered Newtonian and Darcy's law is considered.
- The effect of chemical reactions and salinity is disregarded.

The data representing the basic properties of the model are categorized into sections as follows:

1. Rock data,
2. Fluid components data,
3. Rock-fluid interaction,
4. Initial conditions,
5. Wells data.

Hereafter the implementation of the core flooding activity described in the previous chapter is described.

Rock data

The first step of the modeling path is the rock sample design. Despite the cylindrical shape of the Berea core, it is a common practice to adopt a Cartesian squared section grid for the grid model, where the extent of the area is the same as the real one. The longitudinal direction of the sample (assumed as the flow direction) is divided into 100 cells. The grid geometrical properties are listed in Table 4.1.

N. cells	100x1x1
Length (i dimension) [cm]	9.72
Height and depth (j and k dimension) [cm]	4.44
Area [cm^2]	19.71
Volume [cm^3]	191.62

Cell i dimension (Δi) [cm]	0.0972
Cell j dimension (Δj) [cm]	4.44
Cell k dimension (Δk) [cm]	4.44

Table 4.1: Core grid dimensions.

The sample used for flooding experiment is characterized by a porosity φ of 22.56% and a permeability k = 360 mD, both assessed through laboratory tests. The pore volume of the system is then $4.323 \cdot 10^{-5}$ m^3 (obtained from the product of φ and the total plug volume).

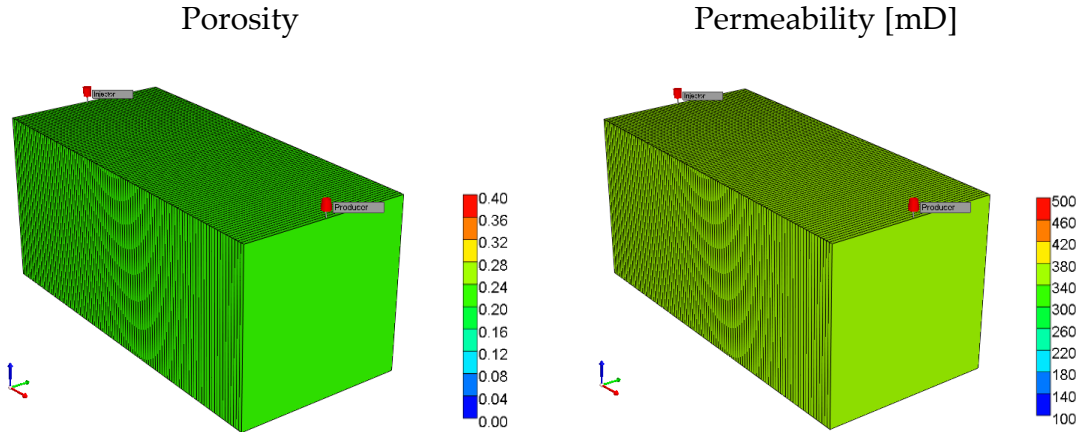

(a) Core sample porosity φ. (b) Core sample permeability k.

Figure 4.1: Grid petrophysical properties on the simulator interface.

Fluid components data

Water and oil are the two phases initially present within the system. Absence of gas is assumed. Fluid properties (i.e. molecular weight, density and viscosity) must be specified according to the experiment at reservoir temperature, that is equal to 77°C. Many of these are directly obtained from laboratory measurements except water viscosity at the reservoir temperature that is extrapolated trough a regression on experimental value obtained at lower temperature. The results of the regression procedure are shown in Table 4.2 and Figure 4.2. A second order polynomial regression curve has been used to get the value at 77°C.

Temperature [°C]	Water Viscosity [cP]
50	0.547
60	0.466
70	0.404
80	0.354
90	0.314

Table 4.2: Water viscosity values.

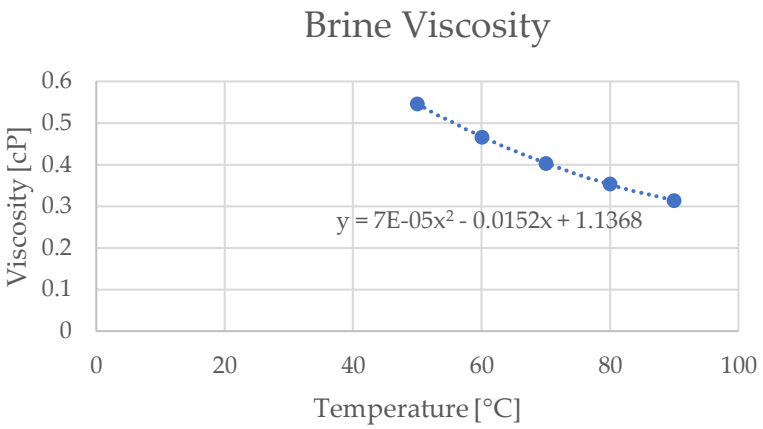

Figure 4.2: Brine viscosity interpolated values.

The values of fluid parameters used for each fluid are listed in Table 4.3.

	MW [kg/mol]	Density @ 77°C [kg/m^3]	Viscosity @ 77°C [cP]
Brine	0.018	973.61	0.381
Oil	0.210	915.8	64

Table 4.3: Oil and water features.

Since the test is carried out under isothermal conditions, these parameters remain constant during the test simulation.

Rock-fluid interaction

The saturation function curves are defined in the following. These refer to relative permeabilities and capillary pressure as a function of water saturation. Capillary pressure is set to zero since it is commonly considered to be negligible in 1D simulations (e.g., [86,87]).

Relative permeabilities are defined following Corey's model [88], i.e.:

$$k_{ro} = k_{ro,max}\left(\frac{S_o - S_{or}}{1 - S_{or} - S_{wi}}\right)^{n_o} \tag{4.5}$$

$$k_{rw} = k_{rw,max}\left(\frac{S_w - S_{wi}}{1 - S_{or} - S_{wi}}\right)^{n_w} \tag{4.6}$$

Here, $k_{ro,max}$ and $k_{rw,max}$ are the values of oil relative permeability at connate water saturation and water relative permeability at irreducible oil saturation respectively; S_o and S_w are oil and water saturations; S_{wi} is the initial water saturation and S_{or} is the residual oil saturation and n_w and n_o are the Corey's exponents. In order to define the relative permeability curves, that is the values of k_{ro} and k_{rw}, it is

necessary to know all these parameters. The initial water saturation and the residual oil saturation are already known from the laboratory evaluations, while $k_{ro,max}$, n_o and n_w undergo a tuning process to fulfil the history matching of the experimental data, once the entire model is specified. $k_{rw,max}$ can be calculated from the value of effective permeability obtained in Chapter 3 by the use of Darcy's law. The end-point relative permeability of water, referring to residual oil saturation conditions, is expressed, indeed, as the ratio between the effective permeability and the absolute permeability:

$$k_{rw,max} = \frac{k_{effective}}{k_{absolute}} = 0.0258 \tag{4.7}$$

All the values of the described parameters already known are reported in Table 4.4.

S_{wi}	0.272
S_{or}	0.265
$k_{rw,max}$ $(@S_{or})$	0.0258

Table 4.4: Data required for the computation of relative permeability curves.

Initial conditions

Initial water saturation is set to 0.272 (as discussed in Chapter 3), initial salt concentration to 77300 mg/l and initial pressure to 1 atm. Fluid properties are defined according to the experiment at a reservoir temperature of 77°C, as previously explained. In this case two phases are present, oil and water that are considered immiscible.

The sand-pack system flooding studies are simulated in two main steps: water flooding and a subsequent nanoemulsion flooding. To better understand the nanoemulsion effect on the system, the latter has been divided into two subsections, each of which aimed at reproducing a specific mechanism of action (solvent and surfactants). In addition, in order to reproduce the complete laboratory experiments, an additional step for chase water injection has been considered.

Wells data

Boundary conditions, at the inlet and the outlet of the sandpack are set via two fictitious wells, an injector and a producer, located in the first and in the last cell of the grid (i direction), respectively. Each point well has a radius of 0.00414 m and is associated with an operating constraint:

- Injector: constant injection rate equal to 0.7 ml/min;
- Producer: bottom-hole pressure equal to 1 bar.

4.3.1. Water flooding

The experimental data to be simulated are discussed in Chapter 3 (see also Figure 3.8).

The coreflooding experiment is simulated through a classical History Matching (*HM*) procedure. Laboratory data are matched by modifying the oil and water relative permeability curves (*KRs*). The *KRs* are modeled through the Corey's formulation, defined in Equation (4.5) and (4.6).
The tuning process on the Corey's exponents is structured according to the procedure described in the following:

1. Guess n_o, n_w and $k_{ro,max}$ to generate the *KRs*;
2. Implement the *KRs* in the simulator;
3. Run the simulation;
4. Do the simulated *RF* and ΔP match the experimental results? If YES, the guessed n_o and n_w are correct to match the experimental results. If NO, restart the procedure from point 1.

A sufficiently satisfactory agreement is achieved with the Corey parameters values listed in Table 4.5. The corresponding relative permeability curves are depicted in Figure 4.3.

$K_{ro,max}$ (@ S_{wi})	0.1
n_w	3
n_o	1.8

Table 4.5: Parameters for Corey correlation.

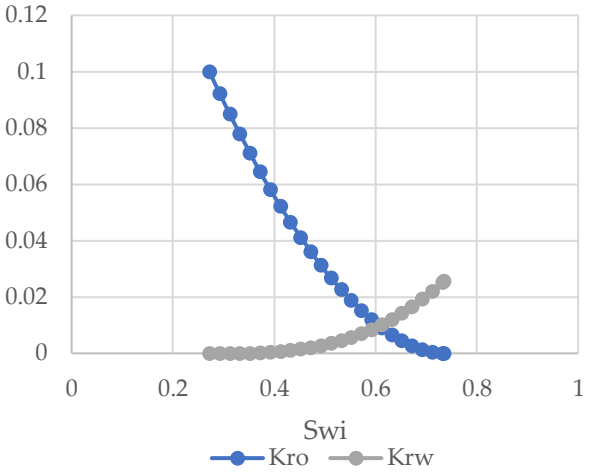

Figure 4.3: Oil and water relative permeabilities at variable water saturation.

At the end of the waterflooding simulation run, the results shown in Figure 4.4 and Figure 4.5 have been obtained.

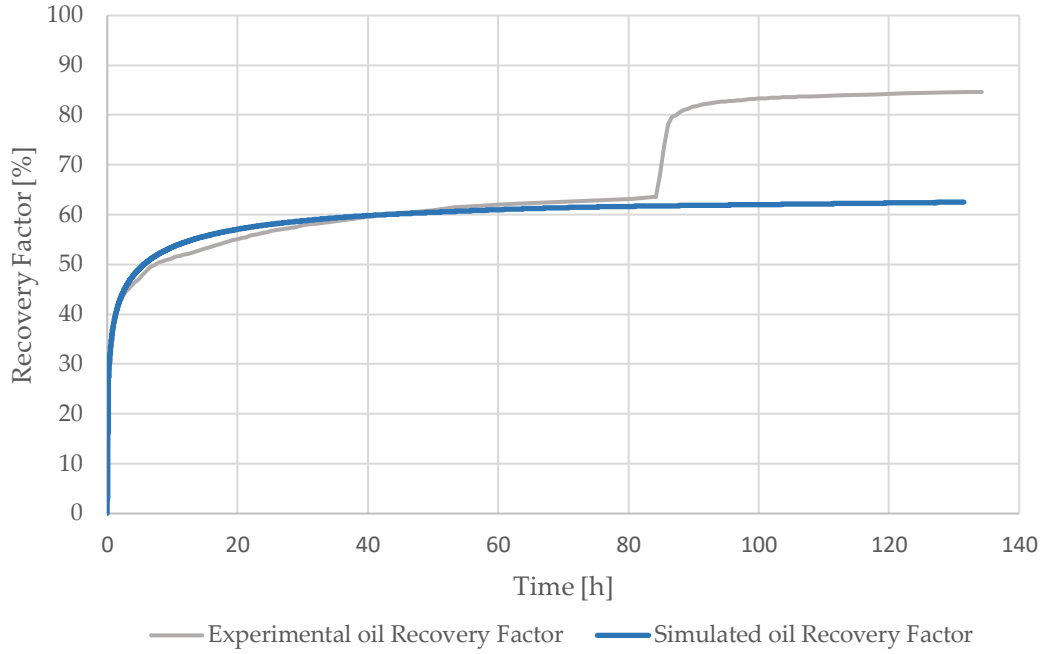

Figure 4.4: Experimental and modeled Recovery Factor.

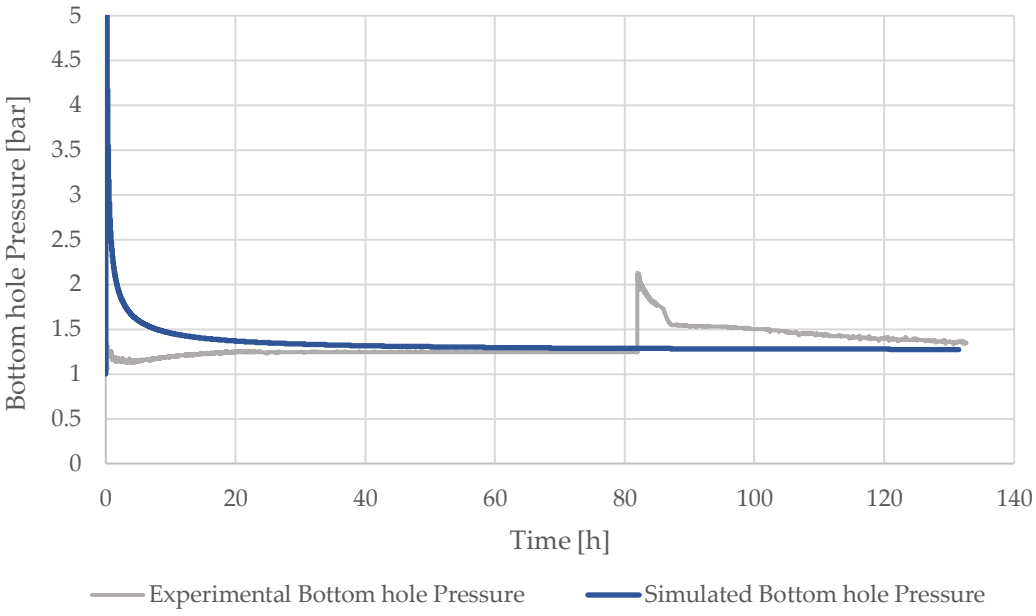

Figure 4.5: Experimental and modeled Bottom hole Pressure.

4.3.2. Nanoemulsion flooding – Solvent effect analysis

After the water flooding stage, the nanoemulsion injection is performed. The main effect of nanoemulsion application seems to be linked to the diffusion process of the solvent towards the crude oil residing within the reservoir. For this reason, this

mechanism has been "isolated" and analyzed, neglecting, in a first step, the other potential mechanism identified. In particular, the presence of surfactant has been neglected in this preliminary analysis.

As stated in Chapter 3, the solvent used in this experiment is xylene, which is intended as a mixture of O-Xylene, M-Xylene and P-Xylene. In order to find the properties of this blend, each type of solvent is firstly analyzed singularly in terms of density and viscosity, starting from literature data [89,90] to find the properties at the desired temperature. Average values are then considered to account for the combination of the three fluids. The dependence of density and viscosity of O-Xylene, M-Xylene and P-Xylene on temperature are depicted in Figure 4.6 and Figure 4.7 respectively.

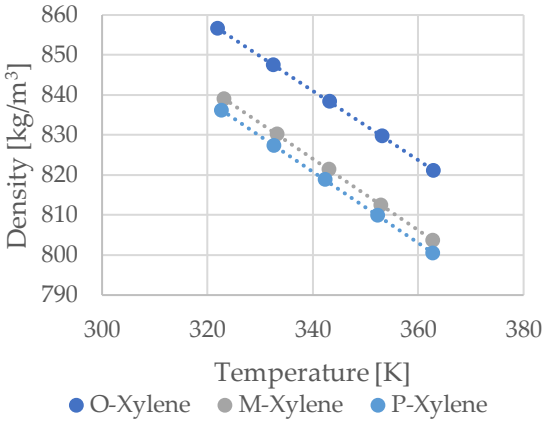

Figure 4.6: Density of different xylene blends.

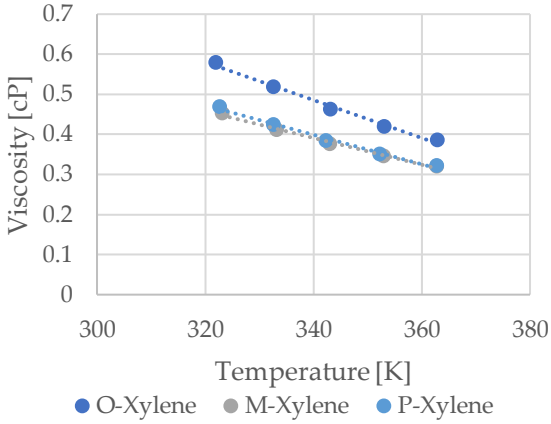

Figure 4.7: Viscosity of different xylene blends.

Table 4.6 summarizes viscosity and density of each xylene component at 77°C.

	Density [kg/m³]	Viscosity [cP]
O-Xylene	832.25	0.449
M-Xylene	814.97	0.372
P-Xylene	811.81	0.353

Table 4.6: Density and viscosity numerical values of different xylene blends.

Finally, to find the properties (Table 4.7) of xylene mixture an equal contribution from each one is assumed in average values calculations.

MW [kg/mol]	Density @ 77°C [kg/m³]	Viscosity @ 77°C [cP]
0.106	819.673	0.391

Table 4.7: Xylene physicochemical properties.

Since the solvent is expected not to cause alteration in rock wettability, rock-fluid properties remain unaltered with respect to waterflooding. However, in order to simulate the migration of the solvent towards the crude oil, an additional feature is added, i.e., the partition coefficient. The partition describes the process of transferring a dissolved substance from a liquid phase to another one (immiscible or partially miscible) in contact with it [91]. For this reason, the partition coefficient (or partition/distribution ratio) is defined as the ratio of the concentrations of a given compound in two immiscible solvents at equilibrium. In other words, considering x_i as the i-th component (solvent) mole fraction in oil and w_i as i-th component (solvent) mole fraction in water, the partition coefficient for the solvent in the nanoemulsion can be defined as:

$$K_i^{ow} = \frac{x_i}{w_i} \tag{4.8}$$

It is possible to define in STARS the reference phase for the fluids involved upon distinguishing components as water-like, oil-like and non condensable gases. Hence, the partition coefficient can be expressed according to the type of fluid considered. In other words:

- For water-like components water is the reference phase and

$$K_i^{ow} = \frac{x_i}{w_i} \tag{4.9}$$

- For the oil-like components, oil is the reference phase and

$$K_i^{wo} = \frac{w_i}{x_i} \tag{4.10}$$

These coefficients are set equal to 0 if no partitioning of liquid is experienced in other phases. The partition coefficient is implemented specifying the element subjected to partition - solvent in this case - and a table representing the variation of the coefficient as a function of temperature and pressure. However, to keep the model simple in this preliminary simulation, the dependence over temperature and pressure is not taken into account, hence the partition coefficient has a unique value. Given the absence in literature of detailed information regarding this parameter and having no information from laboratory experiments, a first attempt value equal to 100 has been considered. This value is then subjected to a matching procedure in order to find the most appropriate value for this specific case, aiming at finding the match with experimental data.

In order to capture the exact moment of the nanoemulsion injection, it is possible to analyze at the pressure drop diagram (Figure 3.8). Since an increase in pressure is clearly noted at 79.62 PV, this value is assumed to be the moment of nanoemulsion

injection. Then, knowing the volume of the slug injected (0.3 PV), it is possible to determine also the end of the slug injection and the beginning of the chase water phase, which role is to clean the core after the passage of the nanoemulsion. Considering ai injection rate of 0.7 ml/min = 0.97 PV/h, Table 4.8 reports the period, in hours, of nanoemulsion injection.

	PV	Time [hours]
Injection start up	79.62	81.95
Injection end	79.92	82.26

Table 4.8: Timing of nanoemulsion injection.

Finally, the weight fraction of solvent and water present in the nanoemulsion have been defined (0.8 and 0.92, respectively).

The results obtained with this preliminary model are displayed in Figure 4.8 and Figure 4.9.

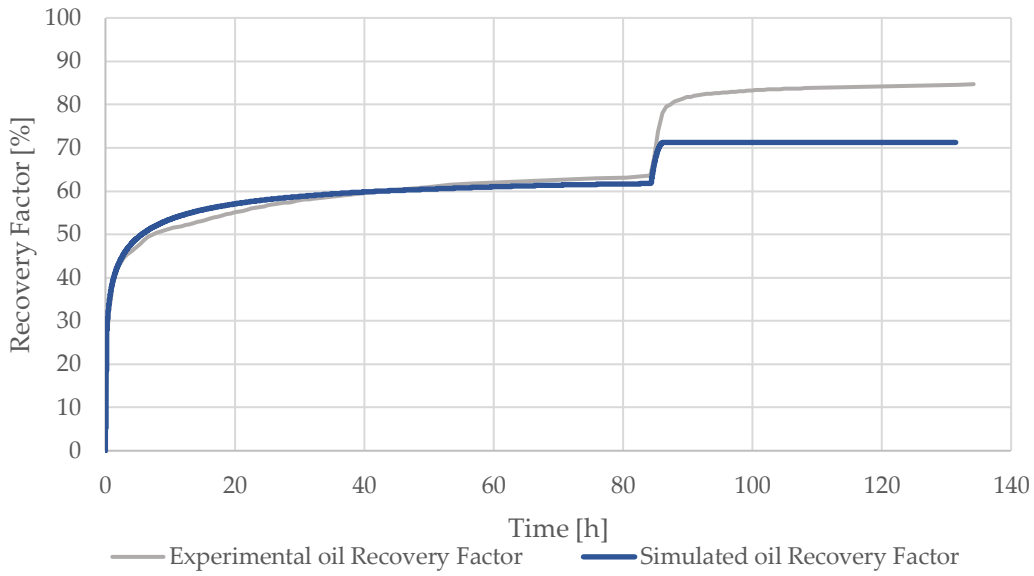

Figure 4.8: Experimental and modeled Recovery Factor.

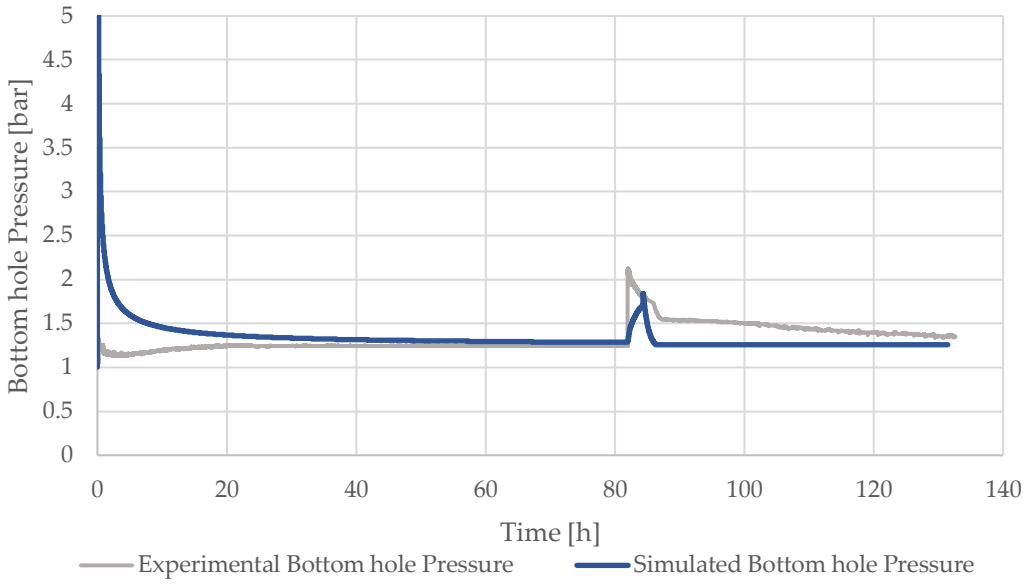

Figure 4.9: Experimental and modeled Bottom hole Pressure.

As it is possible to state from Figure 4.8, the *RF* curve obtained from the simulation run does not coincide with the experimental one. This suggests that the implementation of the solvent partition coefficient inside the model is not sufficient to reproduce accurately the laboratory result, leading to the need of an additional step in the simulation workflow. A supplementary feature, i.e., the surfactant effect, is inserted in the model as detailed in the following paragraph.

4.3.3. Nanoemulsion flooding – Surfactant effect analysis

With the aim to improve the match with the experimental data, the second step of the nanoemulsion injection is to introduce the presence of the surfactant within the nanoemulsion and, as a consequence, to design its effect on the final oil recovery. It is modeled as a mixture of 3 components; hence its properties (i.e the molecular weight, density and viscosity) are obtained as a weighted average of the properties of the singles products. Table 4.9 summarizes the surfactants used and their percentage in the final mixture.

	MW [g/mol]	Percentage (z)
Glucopon 600	386	0.029
Span 80	428.62	0.0056
Atlox 4913	393.14	0.00194

Table 4.9: List of surfactants employed in nanoemulsion stabilization.

The values of density of the single components at 77°C have been obtained with a linear interpolation between known data, as shown in Figure 4.10, Figure 4.11 and Figure 4.12 [92–95].

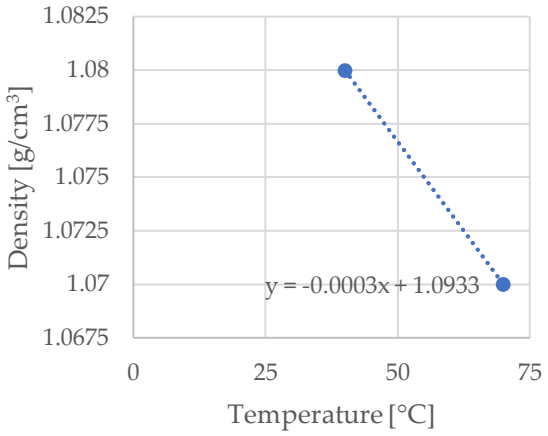

Figure 4.10: Glucopon 600 density at variable temperature.

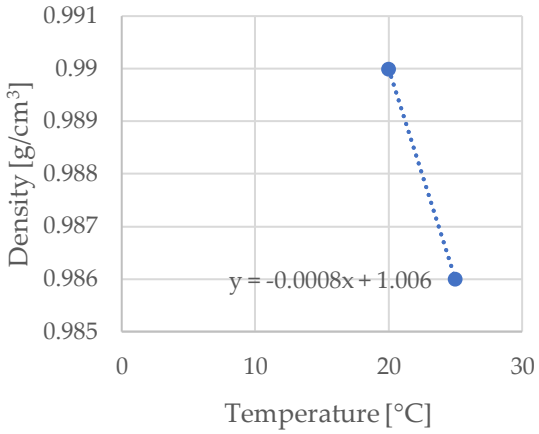

Figure 4.11: Span 80 density at variable temperature.

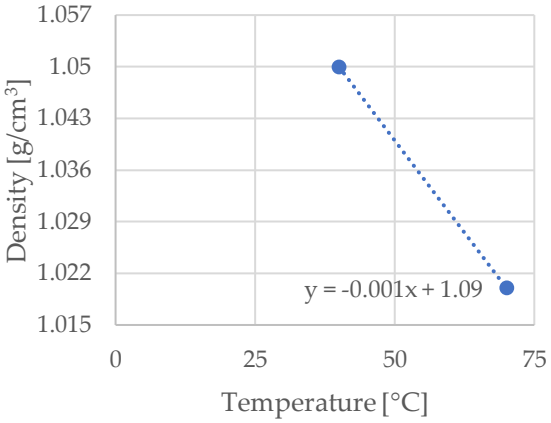

Figure 4.12: Atlox 4913 density at variable temperature

With reference to viscosity, an average value from laboratory measurements has been considered. Table 4.10 summarizes the properties of the final surfactant mixture used within the simulator.

MW [kg/mol]	Density @ 77°C [kg/m³]	Viscosity @ 77°C [cP]
0.393	1049.84	52

Table 4.10: Surfactant package characteristics.

As already discussed in Chapter 2, surfactant presence may affect in a threefold way the model simulation. Their action, indeed, can alter the wettability of the rock, can lower the interfacial tension (*IFT*) between oil and water, while a significant adsorption of the components can take place during the flooding.

Alterations occurring within physicochemical properties of reservoir fluids due to the presence of chemicals i.e., surfactants, polymer and/or nanoparticle lead to varying fluid flow profile during *EOR* [96,97]. Under those circumstance the assumption that rock fluid properties are only functions of fluid saturations and fluid saturation history is not sufficient to accurately describe flow behavior. In these cases, the ability to interpolate basic relative permeability as function of concentration or capillary number can prove very useful [78]. The first process is in fact implemented in the model thanks to the integration of an additional set of relative permeability curves that takes into account a modification of rock wettability towards a more water wet condition with respect to the one used in the waterflooding simulation and first-step of nanoemulsion injection. Interpolation of relative permeability curve available sets is then performed by corresponding to relative permeability datasets in-between high and ultralow *IFT* conditions [96–98]. Among the different available options in STARS, the interpolation is settled as a function of surfactant (defined in this case as *key component*) composition in a specified phase. Further improvements in the study could be achieved, e.g., by assuming capillary number based interpolation criterium which requires direct measurements of *IFT* changes between water and oil due to the presence of surfactants.

The new set of curves is built considering a new value of residual oil saturation coming from the ending part of the experimental recovery curve. Knowing that the ultimate recovery factor is equal to 86% it is possible to compute S_{or} as in (4.11).

$$RF = \frac{S_{oi} - S_{or}}{S_{oi}} \tag{4.11}$$

Exponents of the new set of relative permeability curves have been varied during the *HM* phase.

S_{wi}	0.272
S_{or}	0.1116
$k_{rw,max}$ (@S_{or})	0.0258
$k_{ro,max}$ (@S_{wi})	0.1
n_w	3
n_o	1.8

Table 4.11: Parameters for Corey correlation.

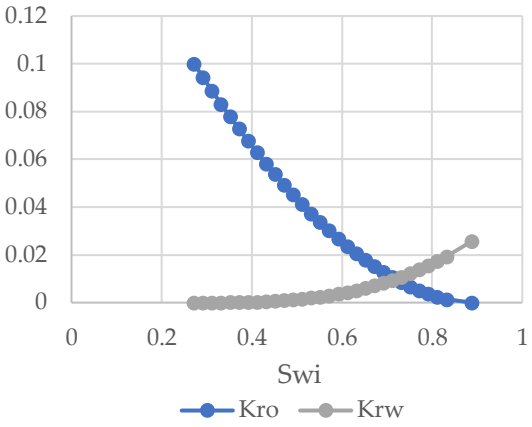

Figure 4.13: Oil and water relative permeability at different water saturations.

This new wettability condition of the rock is associated with the presence of an ultralow value of *IFT* between phases, hence to a massive presence of surfactants in the injected fluid. For this reason, those curves are employed by the software when the maximum concentration of surfactants is detected inside the cell. On the opposite, the original relative permeability curves introduced in previous paragraph, remain valid to represent the condition in which no surfactant presence is encountered inside the cell. As the nanoemulsion invades the core sample, the concentration of surfactant in each cell progressively changes and the software automatically performs an interpolation between the two limiting sets so that a proper couple of curves is used for the calculations at each timestep.

The second aspect which is strictly related to this additive is adsorption onto rocks. STARS allows a phenomenological description of this phenomenon by using a set of adsorption isotherms. Such isotherms are based on Langmuir correlation.

$$Ad = \frac{K_1 \cdot c_a}{1 + K_2 \cdot c_a} \tag{4.12}$$

Where:

- Ad = moles of adsorbed component per unit volume;
- K_1 and K_2 are two constants;
- c_a = fluid component concentration.

These curves relate the adsorbed moles of component per unit pore volume to the mole fraction of that component in a specific phase [78]. The two constants K_1 and K_2 are generally temperature dependent and related each other thanks to maximum rock adsorption capacity. Indeed, the maximum adsorption level associated with this formula is K_1/K_2.

Permeability alteration is often a consequence of adsorption (especially if adsorption is mechanical). The simulator accounts for this occurrence via region dependent residual resistance factors parameters (*RRF*) which allow correlation of local permeability with local adsorption levels. The *RRF* is defined as the ratio of the mobility of brine to that of a single-phase surfactant solution flowing under the same conditions.

$$RRF = \frac{\lambda_{aq}}{\lambda'_{aq}} = \left(\frac{k_{aq}}{\mu_{aq}}\right)\left(\frac{\mu'_{aq}}{k'_{aq}}\right) \tag{4.13}$$

For each phase, permeability reduction factors are defined as follows:

$$RK_j = 1 + (RRF - 1)\frac{Ad(c,T)}{Ad_{max,T}} \qquad j = w, o, g \tag{4.14}$$

The way they affect permeabilities of phase *j* in block *i* is shown in (4.15).

$$k'_{j,i} = k_i \cdot \frac{k_{rj}}{RK_{j,i}} \qquad j = w, o, g \tag{4.15}$$

where k_i is the block permeability.

The values of parameters requested to implement these correlations are taken from the literature [49,99–104].

Results obtained with the use of the implemented model (solvent plus surfactant effect) are depicted in Figure 4.14 and Figure 4.15. Results stemming from the simulation with only solvent is also depicted, to allow a clear comparison between the two simulations.

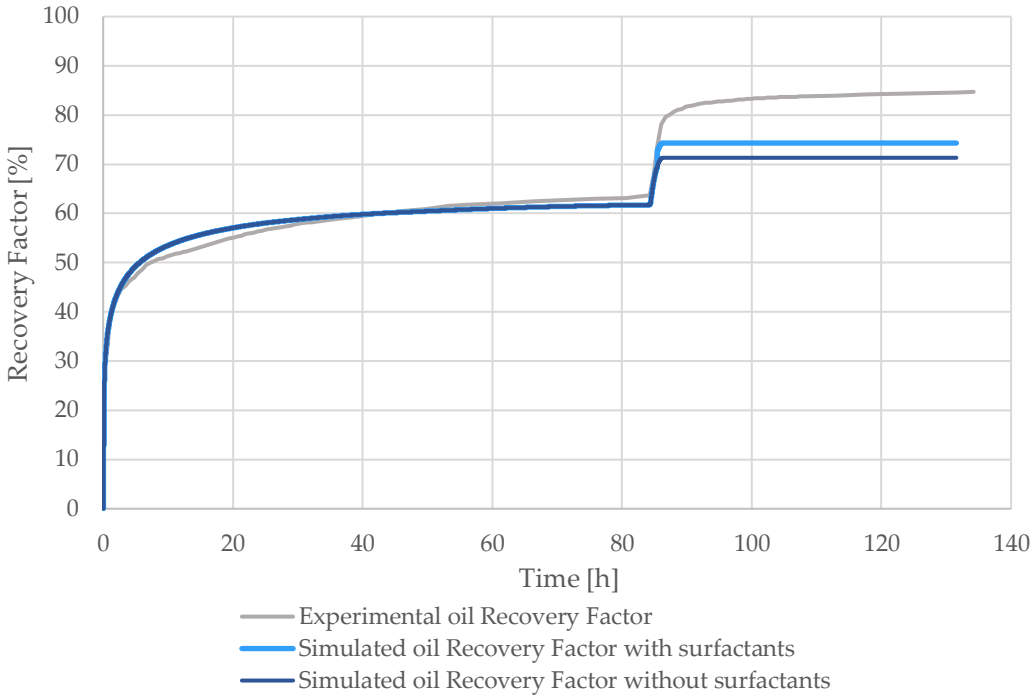

Figure 4.14: Experimental and modeled Recovery Factor.

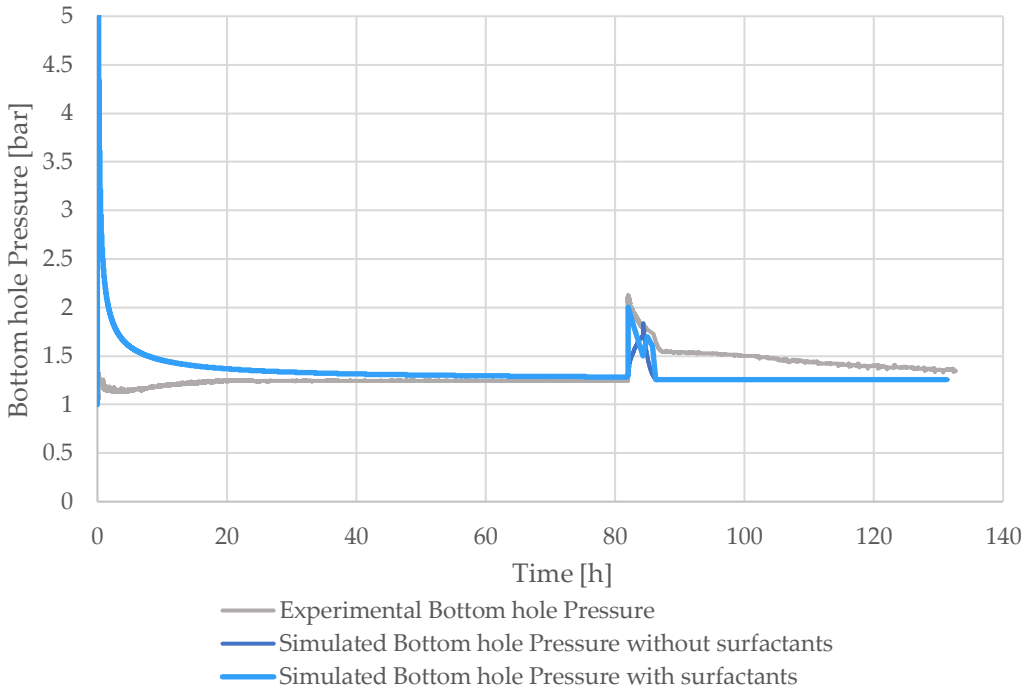

Figure 4.15: Experimental and modeled Bottom hole Pressure.

4.3.4. CMG History matching

Coreflooding history matching aims at interpreting the observed experimental results of recovery factor and pressure by tuning model uncertain parameters. History matching is carried out using CMG-CMOST simulator, where 400 model runs are performed with various combinations of model parameters values. The latter are generated by CMG's proprietary optimizer *DECE* (Designed Exploration and Controlled Evolution). The model obtained with the set of data corresponding to the least deviation from experimental results is retained as the best one, for the purpose of our analysis. Software-assisted *HM* has been carried out only for the nanoemulsion injection simulation, given the remarkable amount of unknown parameters, while a manual history matching procedure has been applied for the waterflooding simulation step as described in Section 4.3.1. The parameters whose values are determined by history matching are listed in Table 4.12 (including their initially adopted values). Here, n_w and n_o correspond to the Corey's correlation exponents of the 2nd set of relative permeability curves (Table 4.11), K_i^{ow} is the solvent partition coefficient, K_1 and K_2 are Langmuir constants, and *RRF* is the residual resistance factor acting in permeability reduction.

Parameters	Initial value	Lower limit	Upper limit	*HM* value
n_o	1.8	1	6	1.1
n_w	3	1	6	2.815
K_i^{ow}	100	1	500	271.73
K_1	0.000284 mol/m^3	0.0002 mol/g	0.055 mol/g	0.26 mol/m^3
K_2	100	0.50	500	20.4
RRF	5	1	15	3.8
$Ad_{max,T}$	2.84e-06 mol/m^3	0.5e-6 mol/g	10e-6 mol/g	0.3 mol/m^3

Table 4.12: Parameters subjected to history match procedure together with their values before and after the match.

Figure 4.16 shows the complete set of models generated by the CMG *DECE* optimizer. As stated above, the model with the lowest error will be further used for the analysis related to the optimization of the injected slug.

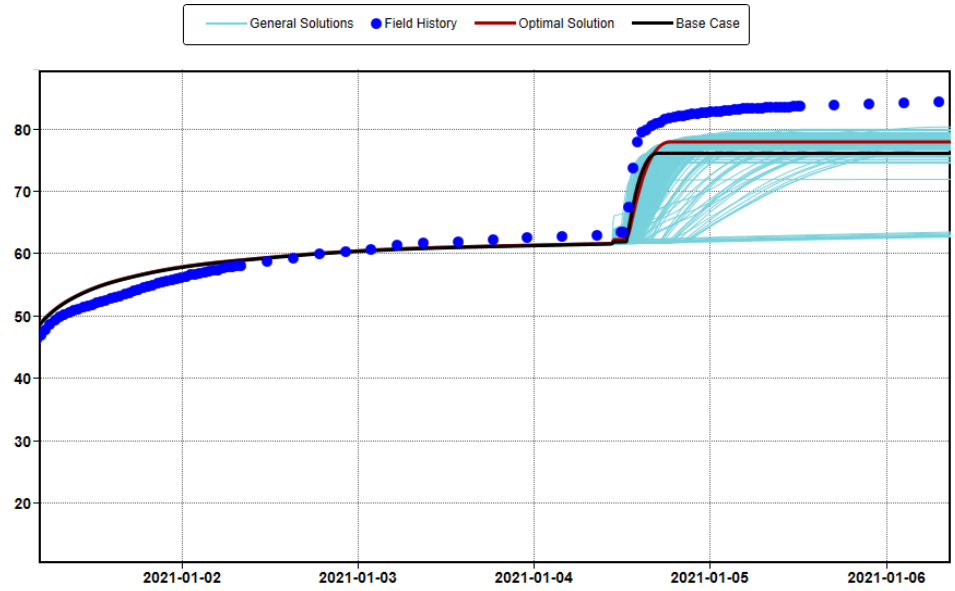

Figure 4.16: CMOST optimization output.

The validated model is reproduced in Figure 4.17 and Figure 4.18.

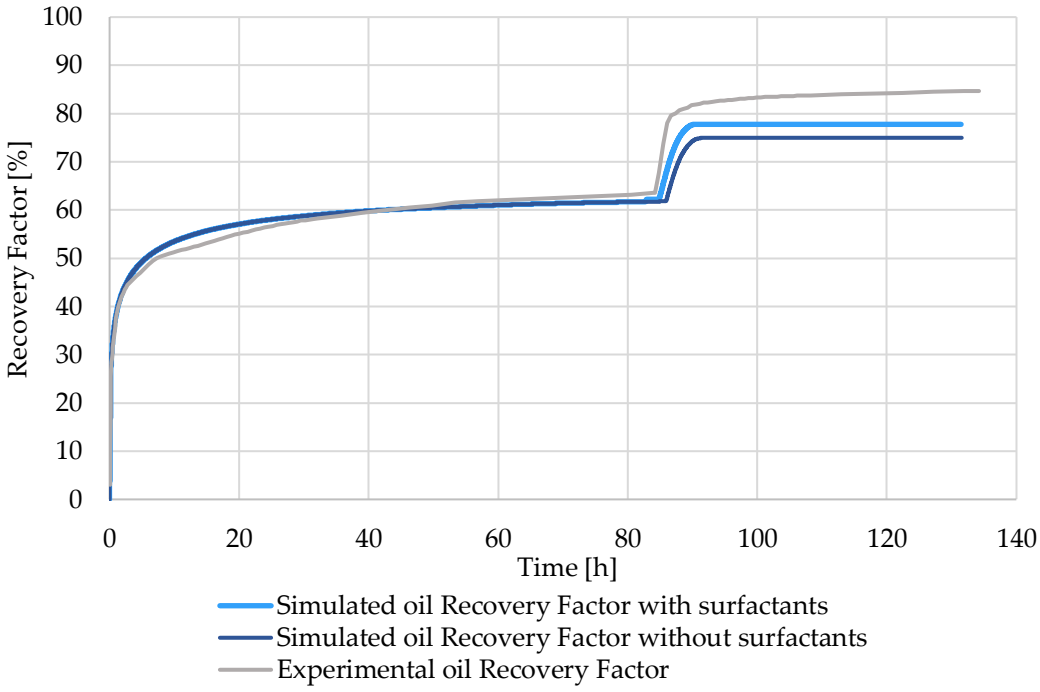

Figure 4.17: Experimental and modeled Recovery Factor.

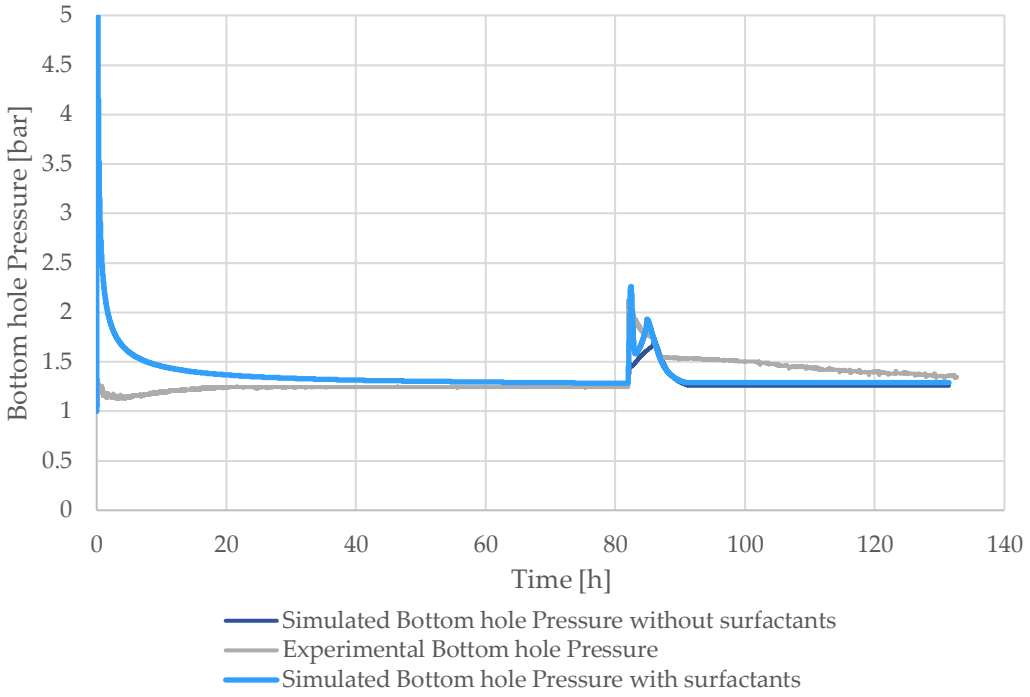

Figure 4.18: Experimental and modeled Bottom hole Pressure.

4.3.5. Final considerations

The study on nanoemulsion simulation has been complemented with an analysis on the oil saturation maps. These are generated for different timesteps:

1. At initial conditions – start-up of the waterflooding phase;
2. At an intermediate timestep – during the waterflooding phase;
3. At the end of the simulation.

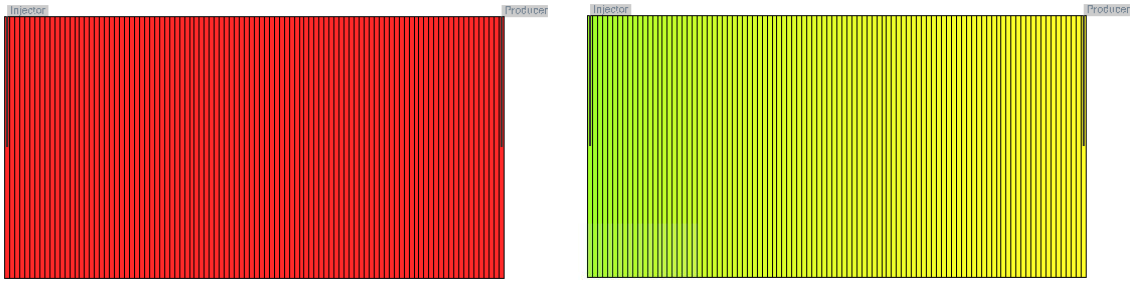

(a) (b)

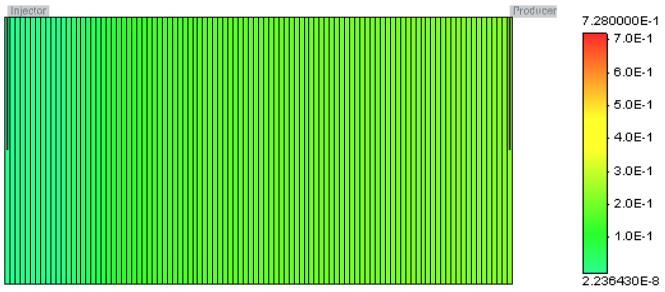

(c)

Figure 4.19: Oil saturation in the core sample at different simulation timesteps: (a) at initial conditions; (b) during waterflooding; (c) at the end of simulation, after nanoemulsion and chase water flooding.

Looking at Figure 4.19, it's possible to notice that at the beginning of the simulation the initial oil saturation is homogeneously distributed within the whole grid. When water is injected inside the core it pushes oil from the injector well (first cell of the grid) to the production well (last cell of the grid).

Oil saturation becomes no more uniform at this point (Figure 4.19 (b)): it is possible to identify the formation of an oil bank at the flood front. A similar oil bank is then formed when nanomeulsion is injected, showing its contribution in sweeping the oil. Figure 4.19 (c) shows that the region near the injection well, when the flooding has been completed, has very low residual oil saturation, leading to an average S_{or} in the core lower than 20%, despite the initial S_{or} of 0.728, confirming the effectiveness of the nanoemulsion technology.

Moreover referring to Figure 4.20 it is clear that nanoemulsion injection has a strong effect in reducing oil viscosity. This is due to the presence of the solvent, that, thanks to its low viscosity, is capable of dilute oil mobilizing it. After all, the impactful role of the solvent has been already confirmed looking at the oil recovery curves. In Figure 4.17 is possible to recognise that the contribution to recovery linked to surfactants presence is smaller in this application with respect to the case of the solvent-alone implementation. This could be explained remembering that the purpose of surfactant addition to the nanoemulsion slug is basically the stabilization of solvent droplets within the brine phase. For this reason these components are present in very small amounts. Hence, their formulation and their concentration is not optimized to bring major changes in rock wettability and in the oil recovery.

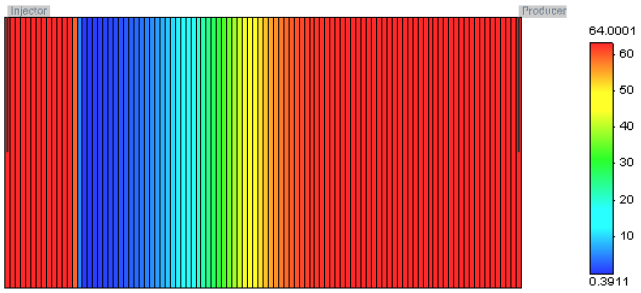

Figure 4.20: Oil viscosity after nanoemulsion injection.

The last consideration to be made about recovery curve is linked to impossibility to the simulator to catch perfectly the ultimate oil recovery: the difference between the experimental (where final *RF* is equal to ~85%) and simulated curves (where final *RF* is equal to ~78%). could be caused by several elements:

1. The strength of nanoemulsion structure lies in the enlarged contact area guaranteed by the solvent through the droplet-like arrangement. This aspect enhances the efficacy of the nanoemulsion if compared to the case of a single and simple solvent slug. Possibly a more accurate modelling of this feature could guide the simulation to a better result.
2. The main process involved in the simulation is surely the solvent partition into the crude oil. However, in real flooding, probably a bilateral migration of solvent into crude oil and vice versa could take place. This could in principle bring to improvements in recovery match; on the other hand, this possibility should be considered during the experimental application, for example estimating the partitioning coefficient of the involved phases.

4.4. Slim tube simulation

Rock data

The simulation phase starts with the definition of the grid to reproduce the 1-D flooding experiments presented in Chapter 3. The features of the grid employed in the numerical simulations are summarized in Table 4.13.

N. cells	100x1x1
Length (i dimension) [cm]	200
Height and depth (j and k dimension) [cm]	0.6824
Area [cm^2]	0.466
Volume [cm^3]	94.2
Cell i dimension (Δi) [cm]	2
Cell j dimension (Δj) [cm]	0.6824

Cell k dimension (Δk) [cm]	0.6824

Table 4.13: Slim tube simulation grid characteristics.

Homogeneous petrophysical properties of the sample are considered.

Porosity [%]	41
Permeability [mD]	2900

Table 4.14: Permeability and porosity assumed in the grid.

Porosity

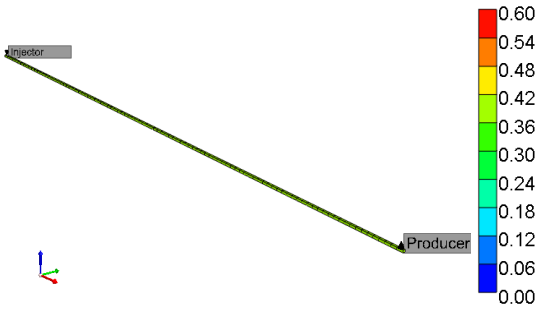

Figure 4.21: Porosity of slim tube grid

Permeability [mD]

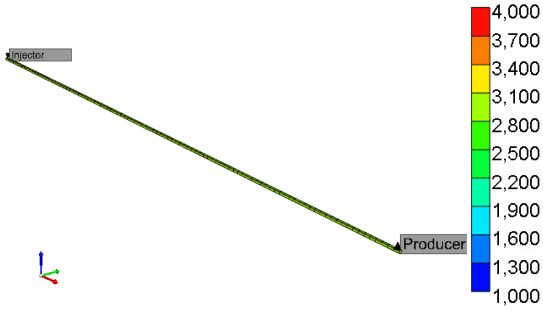

Figure 4.22: Permeability of slim tube grid

Fluid components data

Similar to the scenario associated with the plug, the first step of the simulation is waterflooding, where oil is displaced by water. Key parameters of the fluids are evaluated at reservoir temperature and summarized in Table 4.15.

Components	Brine	Oil
Reference phase	Aqueous	Oleic
MW [kg/mol]	0.018	0.07335
Mass density [kg/m^3]	965.3	822
Viscosity [cP]	0.28	1.7

Table 4.15: Oil and water physical and chemical properties.

Rock-fluid interaction

Relative permeability curves for both oil and water are obtained from the Corey model (Equations (4.5) and (4.6)). While some parameters are taken from laboratory tests, such as the initial water saturation (see Chapter 3), others are computed analytically or through a matching procedure.

As previously described the value of residual oil saturation can be assessed knowing the value of the recovery at the end of waterflooding:

$$RF = \frac{S_{oi} - S_{or}}{S_{oi}} \tag{4.16}$$

To calculate $k_{rw,max}$ and $k_{ro,max}$, the values of effective and absolute permeabilities are needed. In the case of water these values are already defined in the previous chapter. Hence:

$$k_{rw,max} = \frac{k_{effective}}{k_{absolute}} = 0.233 \tag{4.17}$$

For the oil it is possible to determine $k_{ro,max}$ considering the preliminary flooding needed to saturate the slim tube with the oil for the ageing. In this phase the pressure drop is registered and used in the Darcy law for the relative permeability evaluation. Considering a pressure drop of 6.5 bar, the final value for $k_{ro,max}$ equal to 0.654.

S_{wi}	0.38
S_{or}	0.17
$k_{rw,max}$ $(@S_{or})$	0.2334
$k_{ro,max}$ $(@S_{wi})$	0.6541

Table 4.16: Parameters for Corey correlation.

Initial conditions

Initial conditions are imposed through the specification of initial water and oil saturation, $S_{wi} = 0.38$ and $S_{oi} = 0.62$. Gas presence has been disregarded during this simulation.

The simulation is isothermal, and temperature is set to 90°C (reservoir temperature).

Wells data

Boundary conditions are imposed by the use of wells operating constraints:

- Injector: constant injection rate equal to 0.5 ml/min;
- Producer: bottom-hole pressure equal to 1 bar.

4.4.1. Water flooding

The experimental data to be simulated are discussed in Chapter 3, (see Figure 3.12).

The slim tube experiment is simulated by performing the History Matching (*HM*) procedure. The laboratory measurements are matched by tuning the oil and water relative permeability curves (*KRs*).
The tuning process on the Corey's exponents is performed in way similar to what has been illustrated in Section 4.3.1, i.e.:

1. Guess n_o, n_w to generate the *KRs*;
2. Implement the *KRs* in the simulator;
3. Run the simulation;
4. Do the simulated *RF* and ΔP match the experimental results? If YES, the guessed n_o and n_w are correct to match the experimental results. If NO, restart the procedure from point 1.

A sufficiently satisfactory result is achieved with the Corey parameters values summarized in Table 4.17. The corresponding relative permeability curves are shown in Figure 4.23.

S_{wi}	0.38
S_{or}	0.17
$k_{rw,max}$ $(@S_{or})$	0.2334
$k_{ro,max}$ $(@S_{wi})$	0.6541
n_w	4.5
n_o	1.3

Table 4.17: Parameters for Corey correlation.

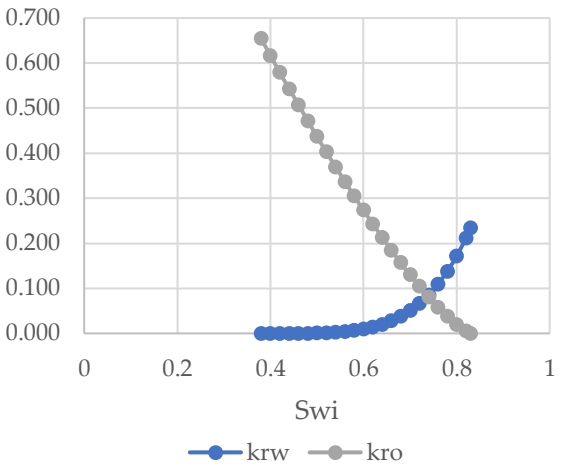

Figure 4.23: Oil and water relative permeability at different water saturations.

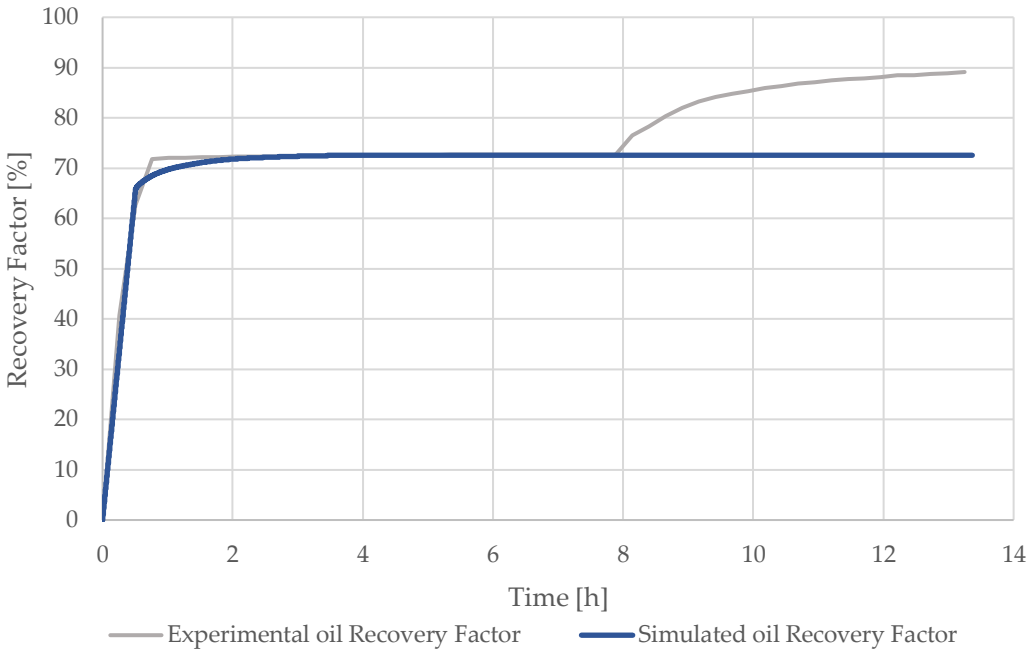

Figure 4.24: Experimental and modeled Recovery Factor.

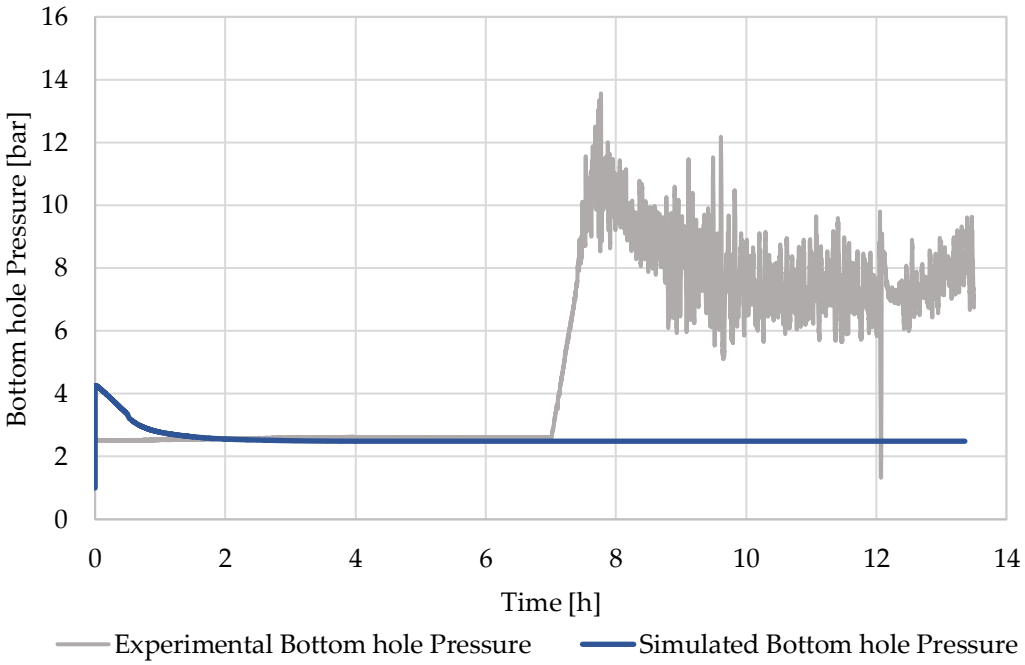

Figure 4.25: Experimental and modeled Bottom hole Pressure.

4.4.2. Nanoemulsion flooding – Solvent effect analysis

The modeling approach conducive to the assessment of the solvent features is described together with the ensuing results.

Since direct measurements of Solvesso 150 chemical properties at 90°C are not possible due to the high temperature, an interpolation on known data of density and viscosity is performed [105] (Figure 4.26 and Figure 4.27). Table 4.18 summarizes the Solvesso 150 properties obtained according to such a procedure.

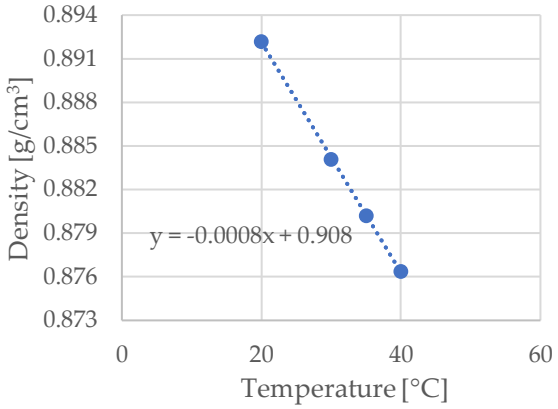

Figure 4.26: Solvent density chart.

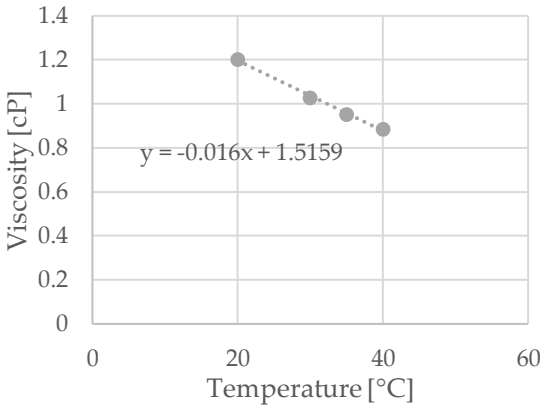

Figure 4.27: Solvent viscosity chart.

Given the linear tendency of the points on the charts the values at 90°C are found.

Temperature [°C]	Density [g/cm³]	Viscosity [cP]
90	0.836	0.0759

Table 4.18: Density and viscosity of Solvesso 150 at 90°C.

As introduced in Section 4.1.2, the mobilization of oil by the action of the solvent is considered through the introduction of the partition coefficient. Its value is not known from experimental application neither from literature. A first attempt value has been assumed to be adjusted through a matching procedure.

Nanoemulsion injection starts after 5.48 PV corresponding to about 7 h, Then the injection lasts for 0.3 PV, until 7.36 h.

The results obtained with this preliminary model are displayed in Figure 4.28 and Figure 4.29.

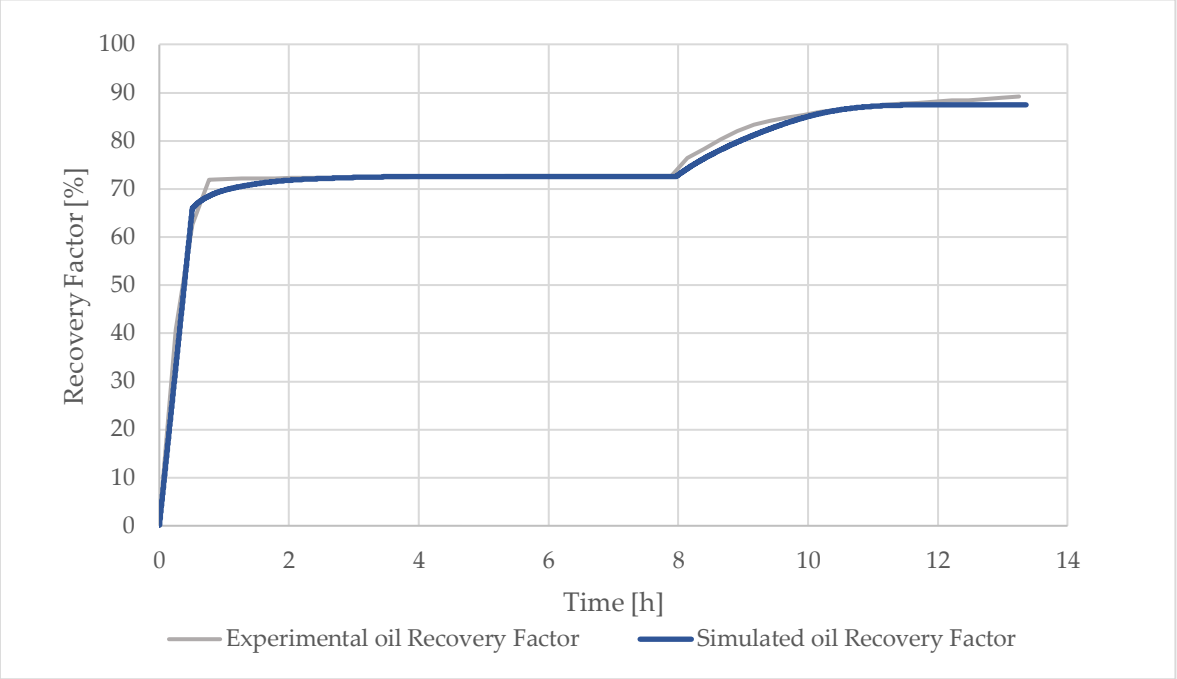

Figure 4.28: Experimental and modeled Recovery Factor.

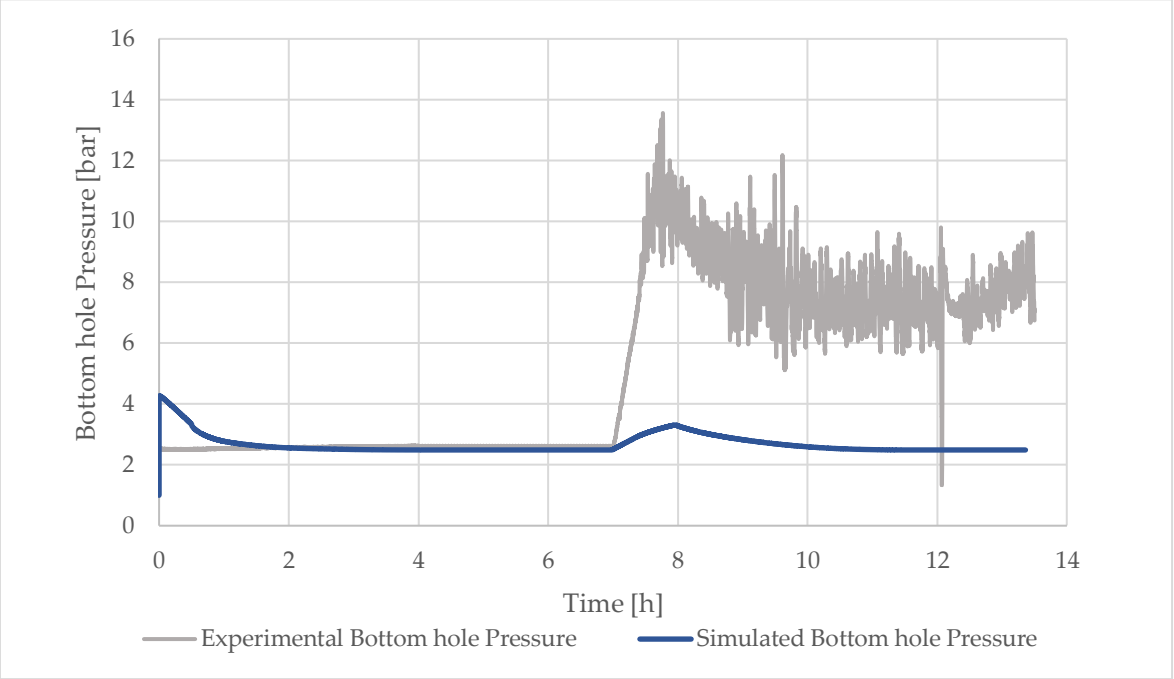

Figure 4.29: Experimental and modeled Bottom hole Pressure.

4.4.3. Nanoemulsion flooding – Surfactant effect analysis

The surfactants package used in this experiment is the same illustrated with reference to the coreflooding application (see paragraph 4.3.3). The only difference

lies in the temperature at which the experiment is performed (from 77°C to 90°C). Table 4.19 reports the surfactant properties at 90°C.

MW [kg/mol]	Density @ 90°C [kg/m³]	Viscosity @ 90°C [cP]
0.393	1044.89	50

Table 4.19: Surfactants package characteristics.

The design of surfactant introduction, as already explained, relies on the modelling of rock wettability alteration and adsorption phenomena.

The additional ultralow *IFT* set of relative permeability curves is computed starting from the calculation of the residual oil saturation after nanoemulsion injection:

$$S_{or} = S_{oi} - RF \cdot S_{oi} = 0.067 \tag{4.18}$$

S_{wi}	0.38
S_{or}	0.0672
$k_{rw,max}$ $(@S_{or})$	0.2334
$k_{ro,max}$ $(@S_{wi})$	0.6541
n_w	4
n_o	1.3

Table 4.20: Parameters for Corey correlation.

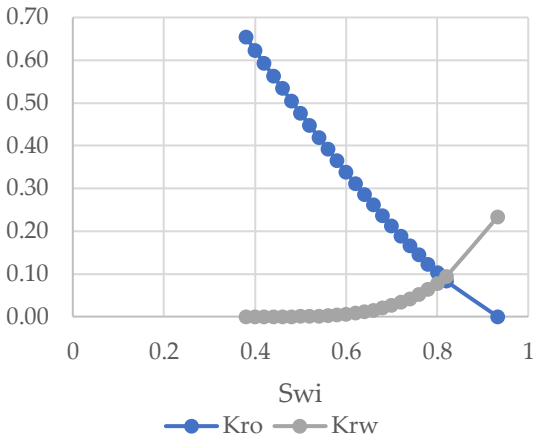

Figure 4.30: Oil and water relative permeability at different water saturations.

Given the absence of specific adsorption studies on slim tubes, assumptions are made on the values of the two constants present in Langmuir correlation. In particular, such parameters have been taken equal to the core case, since the type of rock used in the two tests is similar exception made for the state of compaction.

Results of the model run are shown in Figure 4.31 and Figure 4.32.

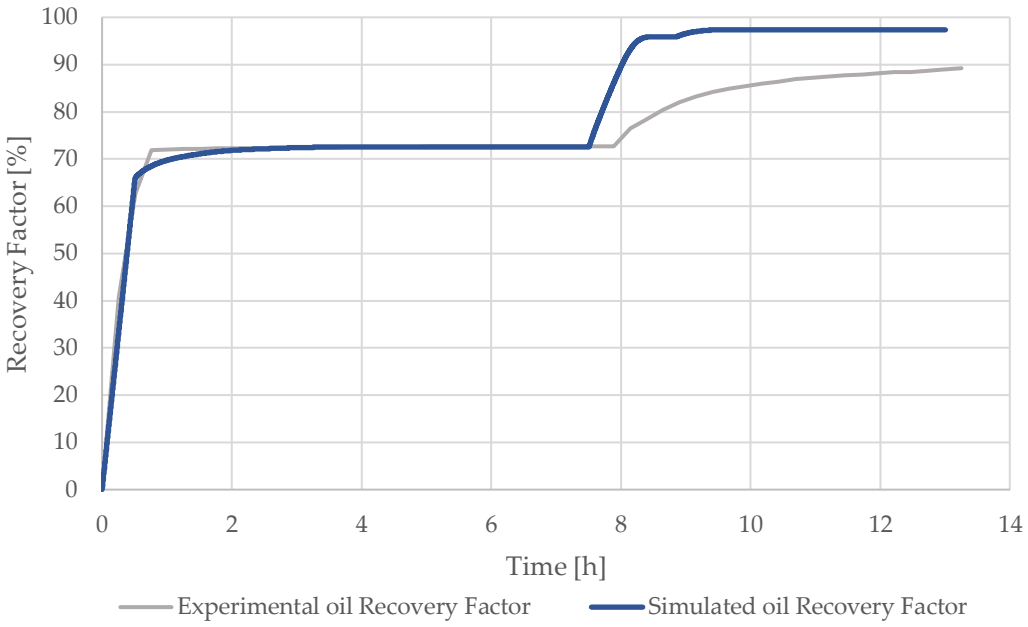

Figure 4.31: Experimental and modeled Recovery Factor.

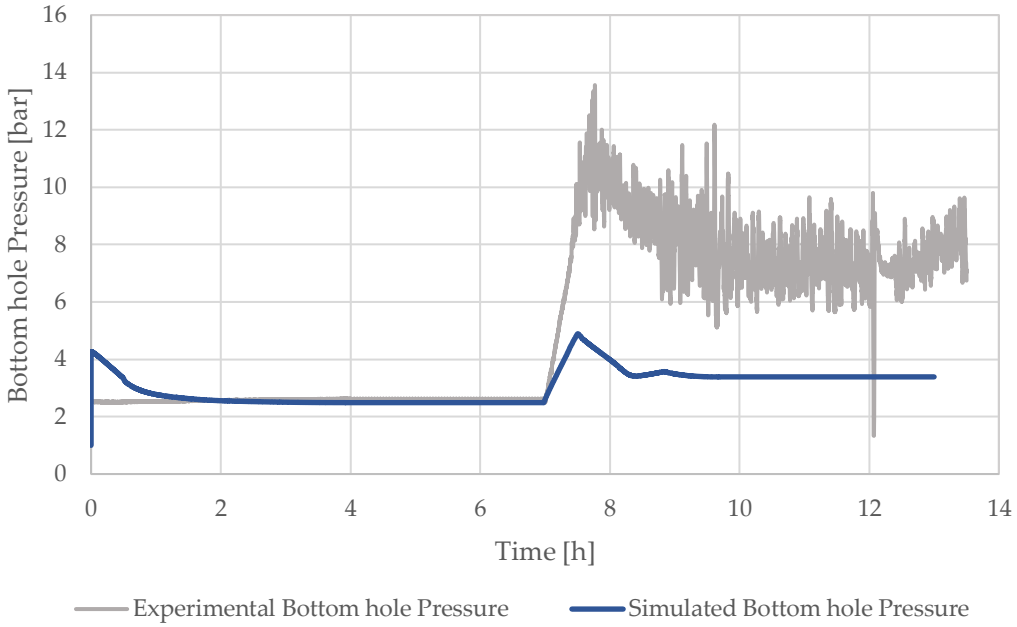

Figure 4.32: Experimental and modeled Bottom hole Pressure.

4.4.4. Final considerations

Analysis of Figure 4.31 and Figure 4.32 is conductive to some final considerations about the role of surfactants and solvent in slim tube application. Comparing Figure 4.31 and Figure 4.28, suggests that the shape of the curve obtained considering only

the solvent effect is more similar to recovery data collected from laboratory tests. The smoother increase in recovery due to solvent contribution follows more accurately the experimental trend with respect to the abrupt rise given by surfactants presence. This tendency of simulated data could be related to the instantaneous change in wettability condition encountered when surfactants are detected by the software. When the impact of relative permeability curves modification is reduced (hence considering a second set of permeabilities similar to the initial set) the steep increase appearing in the curve is less evident. As extreme condition, a case in which there is no wettability alteration and an optimized partition coefficient having a value of 120, has been considered with the following results for recovery curve.

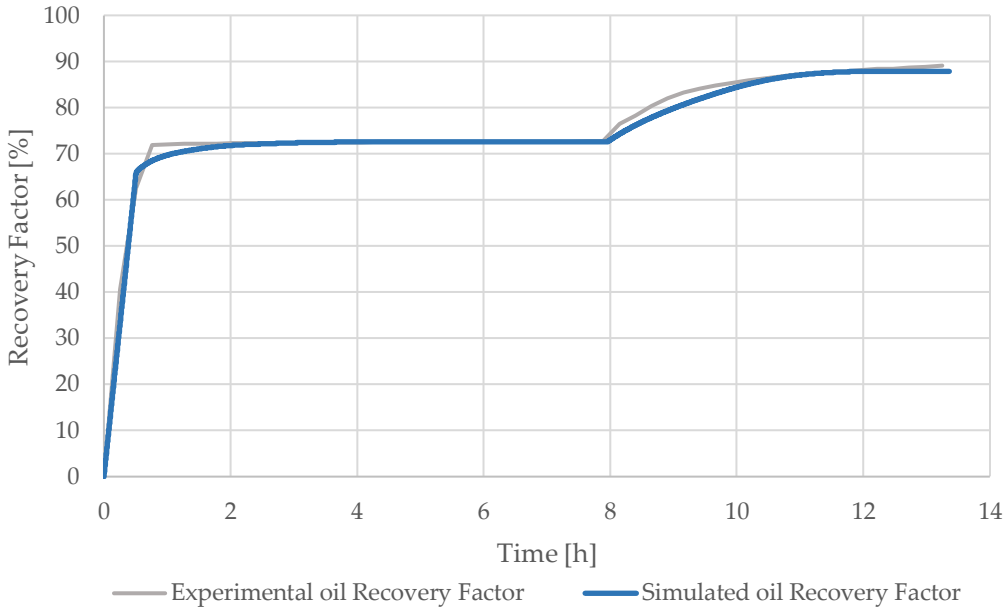

Figure 4.33: Experimental and modeled Recovery Factor.

When dealing with pressure it's possible to affirm that surfactant adsorption and the consequent permeability reduction has a great outcome. Comparing Figure 4.29 and Figure 4.32 suggests that including the surfactant presence in the model favors reproducibility of the experimental data, even if it is still not enough to perfectly match these values. The presence of such intense pressure fluctuations in emulsion flooding tests is confirmed also by literature [106]. The attachment (interception) and detachment (entraining) of the emulsions or snapped-off macro-emulsions as well as the straining (blocking pore throat) are responsible for such a behavior. Also, the pressure fluctuation might be also attributed to instantaneous micelles' stability. It should be mentioned that even if the emulsion is stable within the timeframe of

the experiments, the fluctuations will still exist [106]. Anyway, the overall trend shown by the simulated curve is analogous to the experimental one.

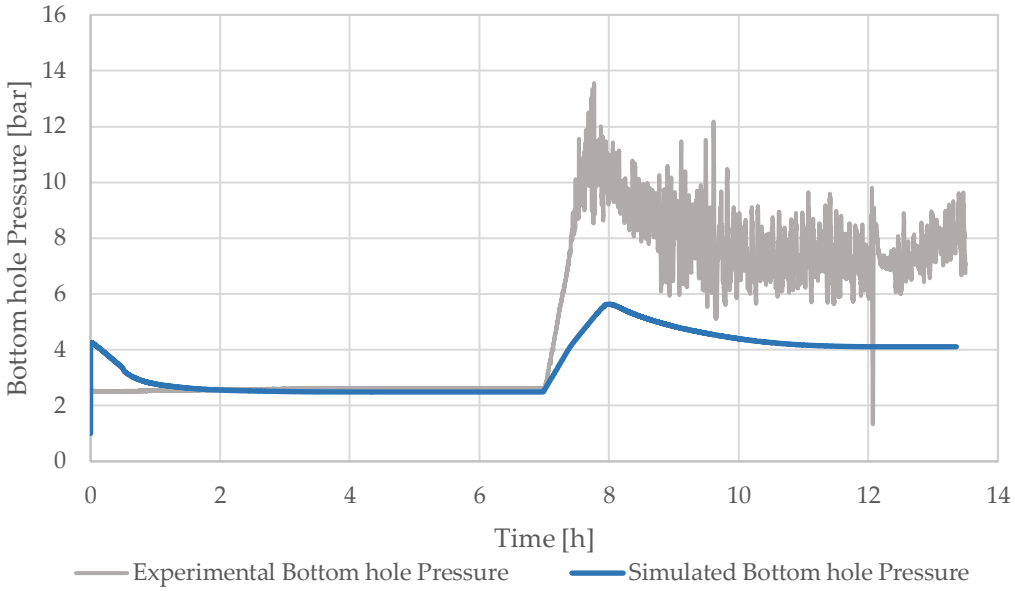

Figure 4.34: Experimental and modeled Bottom hole Pressure.

A more detailed analysis on the impact on the final match of each parameter implemented in this model is performed in the following chapter, with the aim of exploring which among the emulsion behaviors are responsible of recovery and pressure profiles.

The study on nanoemulsion simulation has been completed with an analysis on the oil saturation maps. These are generated for various timesteps:

1. At initial conditions – start-up of the waterflooding phase;
2. At an intermediate timestep – start-up of the nanoemulsion flooding phase;
3. At the end of the simulation.

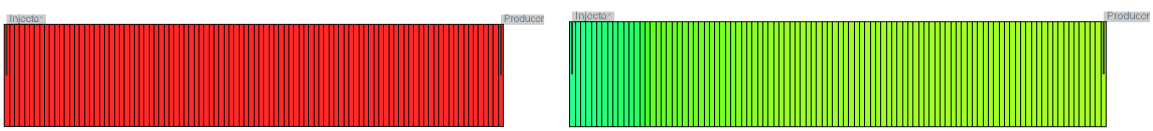

(a) (b)

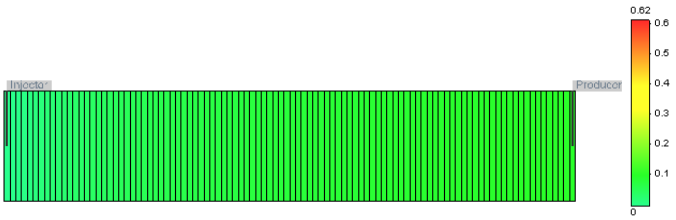

(c)

Figure 4.35: Oil saturation in the core sample at different simulation timesteps: (a) at initial timestep; (b) at the startup of nanoemulsion injection; (c) at the end of simulation, after nanoemulsion and chase water flooding.

As already observed for the core case, nanoemulsion injection has an important impact in residual oil saturation reduction. Oil saturation is homogeneously distributed at the beginning of simulation and equal to 0.62, then oil is displaced first by water then by nanoemulsion until S_{or} becomes less than 0.15 at the end of flooding. The lower value is in any case assessed in the proximity of injection well as it's clearly visible in Figure 4.35 (b) and (c).

5 Global Sensitivity Analysis

The importance of Sensitivity Analysis (*SA*) stems from the observation that a model, which is a mathematical representation of physical phenomena, typically has input parameters whose values are affected from uncertainty. Sensitivity Analysis of a model aims at quantifying the relative importance of model uncertain parameters. Moreover, it is a valuable tool to improve our ability to quantify uncertainty, enhance our understanding of the relationship between model input and outputs and deal with the challenges of model- and data-driven design of experiments. Results of *SA* analysis also offer insights to guide model simplification, for example, through the identification of model input parameters that have negligible effects on target output [107]. *SA* techniques are usually classified into two categories [108]:

- Local Sensitivity Analysis (*LSA*) techniques measure the impact that small variations of model input parameters have on the outputs of the model.
- Global Sensitivity Analysis (*GSA*) techniques try to quantify the influence that variations of the uncertain parameters across their entire range of variability have in the outputs of a model. In this way it is possible to distinguish parameters having a major impact on the variability of a model output and those who are relatively less influential.

Many studies have been devoted to the latter topic in the last thirty years [108]. *GSA* techniques are grounded on diverse approaches among which it's possible to find:

- Regression-based methods: the standardized regression coefficients (*SRC*) are based on a linear regression of the output on the input vector. The input/output Pearson correlation coefficients measure the effect of each input variable by the correlation it has with the model output. Those coefficients are significative if the model is linear, while in case of nonlinearity, they fail to represent properly the response sensitivities.
- Variance-based methods: these methods aim at decomposing the variance of the output as a sum of contributions of each input variable, or combinations thereof. They are sometimes called *ANOVA*, techniques for "Analysis Of Variance" [108].

In addition to those already described, a moment-based *GSA* approach has been recently introduced by Dell'Oca et al. [107]. This method quantifies the relative contribution of uncertain model parameters to the model output probability density function, as described by statistical moments [109].

In this section, the moment-based *GSA* introduced by Dell'Oca et al. [107] is applied to the numerical slim tube flooding model described in Chapter 4, with the purpose of understanding which, among the uncertain parameters used in the simulation, affects in a dominant way two of the outputs of the model, recovery factor and pressure. In particular, paragraph 5.1 presents the set of parameters (and their corresponding space of variability) chosen for the *GSA* analysis because of our imperfect knowledge of their true value.
As a general approach, once defined such parameters, it would be necessary to run the model a sufficient number of times to create realizations to be used in the *GSA* analysis. Given the consistent computational time required by the CMG software to complete one run of the full numerical model, the construction of a simplified surrogate model is required. In this way the computational effort is notably reduced, with simulation runs duration becoming negligible. For the construction of the surrogate two diverse methods are used in the present work: Sparse Grids (*SG*) and Quasi Monte Carlo (*QMC*), both illustrated in Section 5.2. In part 5.3 there is the formulation of surrogate models obtained through Polynomial Chaos Expansion (*PCE*), while in 5.4 the moment-based *GSA* is explained in detail and applied to the results produced by surrogates. In Figure 5.1 the complete *GSA* workflow is shown in a clear way.

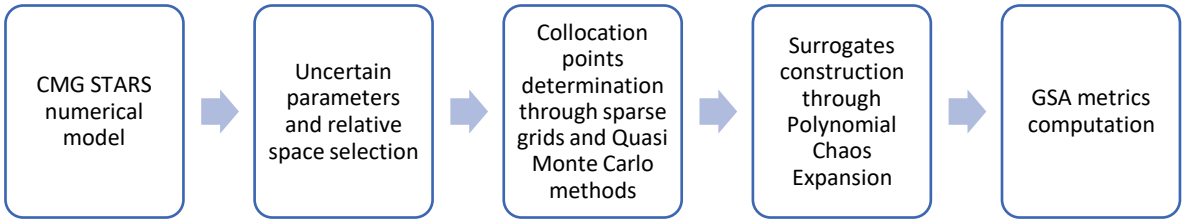

Figure 5.1: GSA complete workflow.

5.1. Parameter selection and parameter space

The first step required during this type of analysis is to consider all the parameters embedded in the model described in Chapter 4 and define which are the ones representing a significant source of uncertainty. Unpredictability of parameters could in general be associated to:

- Variability of physical or chemical conditions;

- Intrinsic variability of that specific parameter;

All the parameters have been considered as independent random variables, each characterized by a uniform probability density function (pdf). This choice can be translated in the idea of assigning equal weight to each value of the parameter distribution.

The parameters chosen for the *GSA* analysis are the ones for which no measurements from laboratory are available. Hence the values assumed for simulations could be majorly affected by uncertainty with respect to others. The variability range of each parameter is specified through the definition of upper and lower boundaries summarized in Table 5.1.

	n_o	n_w	K_i^{ow}	K_1	K_2	RRF	$Ad_{max,T}$
Min	1	1	0	0.48	400	1	0.0012
Max	6	6	500	132	5500	15	0.024

Table 5.1: Range of variability of model parameters.

The range of variability of Corey correlation exponents for the second set of relative permeability curves (n_o and n_w) has been derived from literature publications in which several wetting conditions of different rock types are investigated [110].

Since as an effect of the innovation of the present study, no laboratory measurements or literature value are available for partition coefficient (K_i^{ow}), its value is allowed to vary over several orders of magnitude.

Regarding *RRF*, its values has been chosen in light of different research works on the topic [111–113].

The parameters related to adsorption are usually determined through the use of static and dynamic measurements. In this case values from literature have been used to select the range of variation of K_1, K_2 and $Ad_{max,T}$ [49,99–101,103,104]. Even considering reliable sources, the assumed values are mainly referred to situations which are similar and not exactly equal to the experimental conditions assumed for this study. It would be of primary importance for future developments to assess maximum and minimum values of these parameters in a more accurate way referring to the same surfactants package and rock type.

5.2. Collocation points

Once uncertain parameters are selected, it is necessary to construct the surrogate, which scope is to create realizations of the model with a reduced computational time with respect to the full numerical model. This procedure is aimed at the

construction of the set of scenarios examined in the sensitivity analysis and in this work, it will be based on two diverse methods: sparse grids (*SG*) and Quasi Monte Carlo (*QMC*). These two techniques have gained great attention during the years [114] as alternative algorithms to the robust but computationally demanding Standard Monte Carlo method (*MC*). Although the conceptually simple approach in fact, *MC* typically requires several realizations to achieve statistical convergence [114].

5.2.1. Sparse grids method

This methodology allows to obtain grids that are able to optimize the number of collocation points for the computation of statistical parameters.

SG methods originate from the study of multivariate polynomial interpolation and achieves fast convergence to the solution when it has sufficient smoothness in random space, offering high accuracy with convergence rate depending weakly on dimensionality [114].

The construction of sparse grids is based on a superposition of tensorial grids which are defined through a summation of Lagrange polynomial approximations. The solution of the considered numerical model can be written as [115]:

$$u_{SG}(\boldsymbol{y}) = \sum_{\boldsymbol{i} \in TD(w)} u_{TG,\boldsymbol{i}}(\boldsymbol{y}) \tag{5.1}$$

Where $u_{TG,\boldsymbol{i}}$ is the solution of the model evaluated in tensorial grid points, $\boldsymbol{i} = \{i_1, \dots, i_n\}$ is multiindices vector, hence the grid would be formed by i_1 points in direction 1, i_2 points in direction 2 and so on. Moreover, TD stands for Total Degree which represents the chosen space of multivariate polynomials, and w is the grid level, thus the maximum degree of the interpolating polynomial in every direction.

When all the tensorial grids associated to different multiindices have been generated, the final sparse grid is created from their summation, deleting those collocation points that are repeated more than one time. An example of the construction of a bidimensional sparse grid of level w = 3 is shown in Figure 5.2 [116].

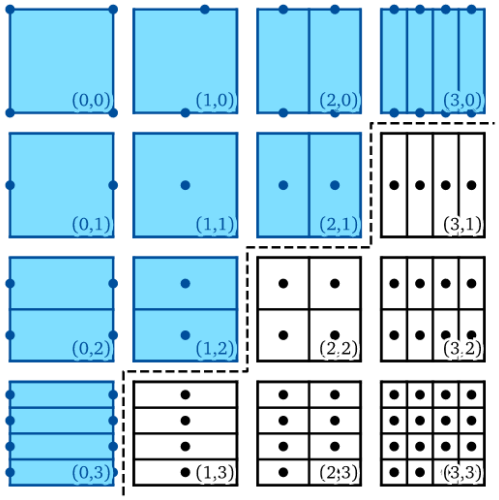

Figure 5.2: Construction of the regular bidimensional sparse grid of level w = 3 [116].

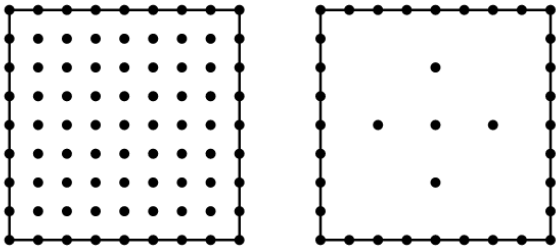

Figure 5.3: Full grid and regular sparse grid of level w = 3 in 2 dimensions [116].

The level of the grid determines the number of points present in it. An increment in the level w brings to increase the collocation points and hence the accuracy of the approximation.

For each tensorial grid a Lagrange interpolating polynomial referred to the numerical model is built:

$$u_{TG,\boldsymbol{i}}(\boldsymbol{y}) = \sum_{\boldsymbol{y}_i \in TG} u(\boldsymbol{y}_i)\, L_{\boldsymbol{i}}(\boldsymbol{y}_i) \tag{5.2}$$

Where $\boldsymbol{y}_i$ are the points belonging to the i-th grid TG, and $L_{\boldsymbol{i}}$ is the Lagrange function of the ith grid centered in $\boldsymbol{y}_i$.

Starting from the realization obtained in sparse grid collocation points, it's possible to directly obtain a surrogate model of the system formed by a summation of polynomial Lagrange approximations. Each polynomial is referred to a specific tensor grid. From this approximation is then possible to get a polynomial chaos expansion (*PCE*) capable to reproduce the output response of the numerical code.

To achieve this, the solution obtained from sparse grid approach is converted in a summation of Legendre polynomials as described in the following Section 5.3.

In the present work the sparse grid level has been set to two different values, w = 2 and w = 4, while keeping the number of unknown parameters constant, to investigate which of the resulting surrogates, obtained through *PCE*, provides the best representation of the output recovery factor and bottom hole pressure simulation results. The number of collocation points for each selected grid level is listed in Table 5.2.

Grid level	Number of collocation points
2	113
4	2437

Table 5.2: Grid levels and their collocation points.

5.2.2. Quasi Monte Carlo method

Another sampling strategy to generate distributed sample points is Quasi-Monte Carlo technique. It can be described as a deterministic version of *MC* sampling method based on the low discrepancy sequences which provides an improved convergence rate with respect to the standard *MC* [117].

This method is able to approximate the integral of a generic function f on the hypercube $[0,1]^M$ (a normalized integration domain) by an equally weighted average of deterministic, uniformly distributed points:

$$\int_{[0,1]^M} f(\boldsymbol{X}) d\boldsymbol{X} \approx \frac{1}{N_r} \sum_{k=1}^{N_r} f(\boldsymbol{X}^{(k)}) \tag{5.3}$$

The deterministic points $\boldsymbol{X}^{(1)}, \boldsymbol{X}^{(2)}, .., \boldsymbol{X}^{(N_r)} \in [0,1]^M$ are chosen as elements of a low-discrepancy sequence [114]. This means that unlike random numbers. Quasi-random points are sequences that know the position of previously sampled points and are built to avoid the presence of gaps and clusters (discrepancies) as much as possible [118].

5.3. Formulation of surrogate models

The computational cost related to high order moments evaluation for complex models may represent a remarkable problem when *GSA* is performed. To overcome this difficulty, we can rely on the use of surrogate models which allow to represent the full model response reducing computational onus [107,119].

Among the different techniques available to build a surrogate model, this work concentrates on the use of the Polynomial Chaos Expansion (*PCE*). It was first proposed by Wiener [117] for problems with Gaussian random inputs and late extended to non-Gaussian random inputs by using polynomials of Askey scheme (generalized *PCE*) [120]. It recreates the outcome of the model as a function of the unknown independent parameters with set probability distribution.

In general, considering a computational model M whose input parameters are represented by a random vector $\mathbf{x}$, it's possible to express the associated random quantity of interest $Y = M(\boldsymbol{x})$ as the infinite series shown in Equation (5.4) [119], [121]:

$$Y = \sum_{j=0}^{\infty} c_j \, Z_j \tag{5.4}$$

in which $\{Z_j\}_{j=0}^{\infty}$ is a numerable set of random variables (which form a basis of the Hilbert space) and $\{c_j\}_{j=0}^{\infty}$ are coefficients. In the specific context of polynomial chaos expansions, the basis terms are multivariate orthonormal polynomials in the input vector $\mathbf{x}$. Furthermore, if the input parameters have a uniform distribution inside the assigned range, the multidimensional polynomials are Legendre type and the *PCE* is commonly defined as generalized [120]. The representation of the random response increases its accuracy as the number of terms in the series approach infinite. However, in practice, only a finite number of terms may be computed, hence it is legitimate to consider a truncated series made of all polynomials up to a certain degree P [119]. Consequently, surrogate models are formulated as follows:

$$Y = \sum_{p}^{P} \alpha_p \, L_p(\boldsymbol{x}) \tag{5.5}$$

where Y is the output of the surrogate (i.e., oil recovery factor and bottom hole pressure), P is the number of terms of the surrogate model, α_p is the coefficient of the p-th surrogate term (also called multi-index); and $L_p(\boldsymbol{x})$ is the p-th multivariate Legendre polynomial expressed as

$$L_p(\boldsymbol{x}) = \prod_{n=1}^{N} L_{n,p_n}(x_n) \tag{5.6}$$

Here, x_n is the n-th parameter of the surrogate and L_{n,p_n} is the Legendre p_n degree polynomial of the parameter x_n.
The number of unknown coefficients α_p in Equation (5.5) is computed as [117,119]:

$$P = \frac{(N+p)!}{N!\ p!} \tag{5.7}$$

This procedure allows to exploit the optimization of collocation point selections given by sparse grids on one side and advantages linked to *PCE* for the surrogate formulation on the other side.

Several surrogate models for each quantity of interest, i.e. Recovery Factor (*RF*) and Bottom hole Pressure (*BHP*), at different timesteps have been created.

Since parameters selected for the *GSA* analysis are linked to nanoemulsion flooding modeling, they do not influence recovery and pressure output at early times (due to waterflooding only). For this reason, the timesteps chosen for surrogates construction are subsequent to nanoemulsion injection startup.

At first *PCE* based on sparse grids of different levels (2 and 4) have been developed for each of the two model outputs and tested over 10 additional random sets of parameters to determine the more appropriate choice for the reproduction of simulations results. The suitability of these surrogates has been assessed via:

- Scatterplots, in which surrogates' predictions are plotted against results of full numerical simulations. A perfect surrogate would render points on the chart aligned on the 45-degree diagonal. This would imply a perfect match between surrogate and numerical model behavior. Some examples at specific timesteps are shown in Figure 5.4.
- Mean Absolute Error (*MAE*), computed between the simulation results and the surrogate's one as in Equation (5.8).

$$MAE = \frac{1}{n}\sum_{i=1}^{n}|x_{sim} - x_{surr}| \tag{5.8}$$

Where:

- n is the number of available data;
- x_{sim} are simulation results values;
- x_{surr} are surrogate results values.

Hereafter some of the plots are shown together with their associated *MAE*.

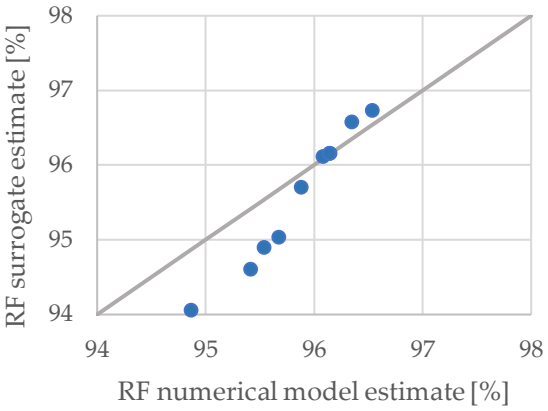

$MAE = 0.3569$

(a) Testing of *RF* surrogate obtained with sparse grid level w = 2

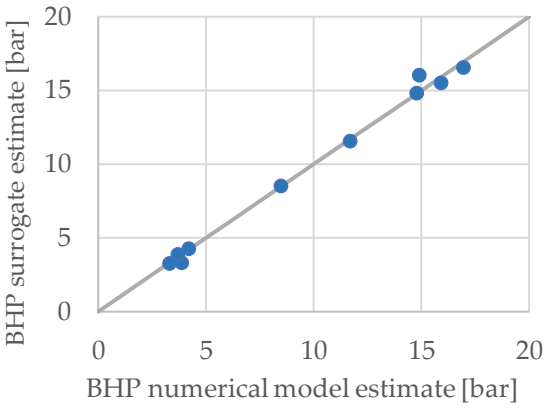

$MAE = 0.2979$

(b) Testing of *BHP* surrogate obtained with sparse grid level w = 2

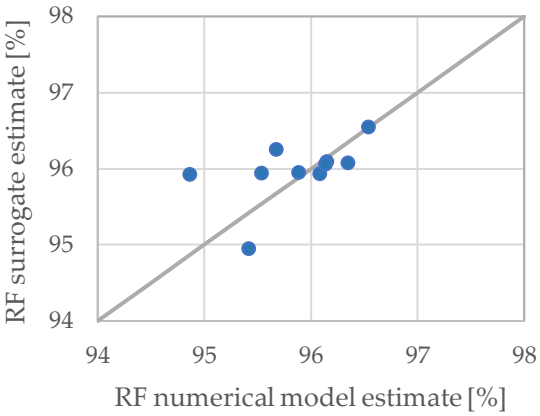

$MAE = 0.3142$

(c) Testing of *RF* surrogate obtained with sparse grid level w = 4

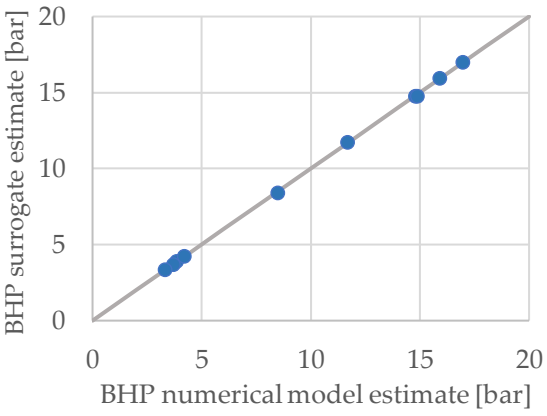

$MAE = 0.0483$

(d) Testing of *BHP* surrogate obtained with sparse grid level w = 4

Figure 5.4: Scatterplots showing the results of sparse grids-based surrogates testing procedure.

By looking at Figure 5.4 (a) and (c) it is possible to observe a deviation of points from the 1:1 line, meaning that the model implemented in the simulator is not well represented by the created surrogate. This is confirmed for all the surrogates representing recovery factor also by the associated error. To improve the accuracy of the *RF* surrogate, *PCE* based on *QMC* method have been analyzed with the same procedure, giving the following outcomes.

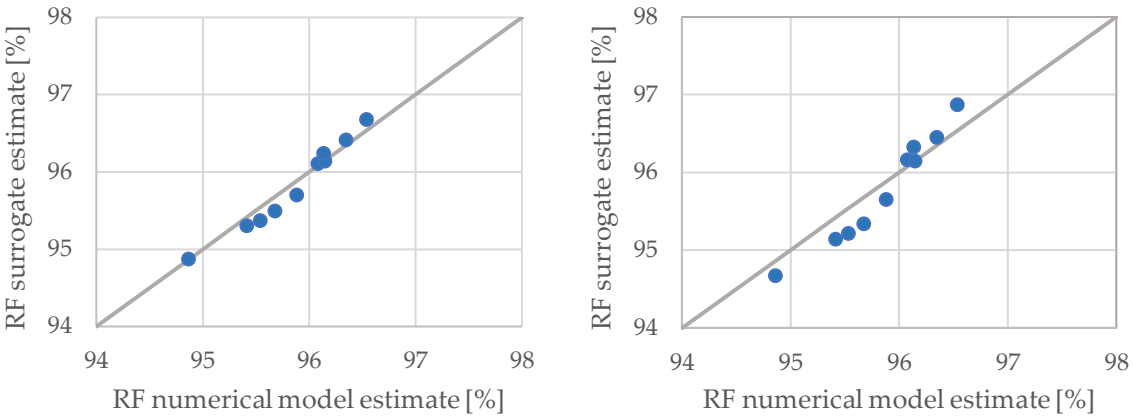

$MAE = 0.0999$

(a) Testing of *RF* surrogate obtained with *QMC* level w = 2

$MAE = 0.2979$

(b) Testing of *RF* surrogate obtained with *QMC* level w = 4

Figure 5.5: Scatterplots showing the results of *QMC*-based surrogates testing procedure.

Both from *MAE* computation and from scatterplots has been highlighted that the best candidate for the description of recovery factor response is *PCE* based on *QMC* with w = 2 while for bottom hole pressure *PCE* based on sparse grid with w = 4.

1000000 Monte Carlo realizations have been produced letting the values of the seven unknown input parameters vary randomly inside the selected ranges. So, the realizations obtained through the use of surrogates offer an evaluation of the two quantities of interest at different timesteps of the simulation starting from casual different sets of parameters. The final purpose is to use this information to analyze the probability density function of recovery and pressure in terms of their first four statistical moments as explained in the next section.

5.4. Moment-based *GSA*

The moment-based Global Sensitivity Analysis aims at overcoming the key limitation of the so-called variance-based methods that is the assumption according to which the uncertainty of the output can be fully characterized by its variance [107]. These methods could in fact provide an incomplete idea of a system response to model parameters. For this reason, the new metrics for *GSA* proposed by Dell'Oca et al. are here introduced to quantify changes in the statistical moments of the probability density function of a target state variable y. This function is assumed to be dependent on N random parameters collected in vector $\boldsymbol{x} = (x_1, x_2, \dots, x_N)$ and defined in the parameter space $\Gamma = \Gamma_{x1} \times \Gamma_{x2} \times \dots \Gamma_{xN}$, $\Gamma_{xi} = [x_{i,min}, x_{i,max}]$ being the

support of the i-th random variable x_i. Changes in the pdf of y are described through its first four statistical moments, i.e., mean, $E[y]$, variance, $V[y]$, skewness $\gamma[y]$ and kurtosis $k[y]$. Therefore, the following quantities are introduced:

$$AMAE_{x_i} = \begin{cases} \dfrac{1}{|y_0|}\displaystyle\int_{\Gamma_{xi}} |y_0 - E[y|x_i]|\rho_{\Gamma_{xi}} dx_i \\ = \dfrac{1}{|y_0|} E[|y_0 - E[y|x_i]|] & \text{If } y_0 \neq 0 \\ \displaystyle\int_{\Gamma_{xi}} |E[y|x_i]|\rho_{\Gamma_{xi}} dx_i = E[|E[y|x_i]|] & \text{If } y_0 = 0 \end{cases} \tag{5.9}$$

$$AMAV_{x_i} = \frac{1}{V[y]} \int_{\Gamma_{xi}} |V[y] - V[y|x_i]|\rho_{\Gamma_{xi}} dx_i = \frac{E[|V[y] - V[y|x_i]|]}{V[y]} \tag{5.10}$$

$$AMA\gamma_{x_i} = \begin{cases} \dfrac{1}{|\gamma[y]|}\displaystyle\int_{\Gamma_{xi}} |\gamma[y] - \gamma[y|x_i]|\rho_{\Gamma_{xi}} dx_i \\ = \dfrac{1}{|\gamma[y]|} E[|\gamma[y] - \gamma[y|x_i]|] & \text{If } \gamma[y] \neq 0 \\ \displaystyle\int_{\Gamma_{xi}} |\gamma[y|x_i]|\rho_{\Gamma_{xi}} dx_i = E[|\gamma[y|x_i]|] & \text{If } \gamma[y] = 0 \end{cases} \tag{5.11}$$

$$AMAk_{x_i} = \frac{1}{k[y]} \int_{\Gamma_{xi}} |k[y] - k[y|x_i]|\rho_{\Gamma_{xi}} dx_i = \frac{E[|k[y] - k[y|x_i]|]}{k[y]} \tag{5.12}$$

Where $y_0 = \int_{\Gamma} y(\boldsymbol{x})\, \rho_{\Gamma_x} d\boldsymbol{x}$ and ρ_{Γ_x} is the pdf of $\boldsymbol{x}$.

It is important to clarify the meaning of these indices recalling that $M[y|x_i]$ (where M = E, V, γ, k) denotes the statistical moment M conditional to a known value of parameter x_i. Therefore, the scope of these quantities is to analyze the expected distance between a given statistical moment of y conditional to values of a model parameter and its unconditional counterpart.

5.5. Results and discussion

The charts presented in this paragraph represent the results of the *GSA* metrics computation for both recovery factor (Figure 5.6) and bottom hole pressure (Figure 5.7). In each graph one index is plotted in logarithmic scale versus the timestep at which it has been computed, providing an outlook of the temporal evolution of those indices. The different colors of the curves highlight the diverse impact that every parameter has on the considered metric.

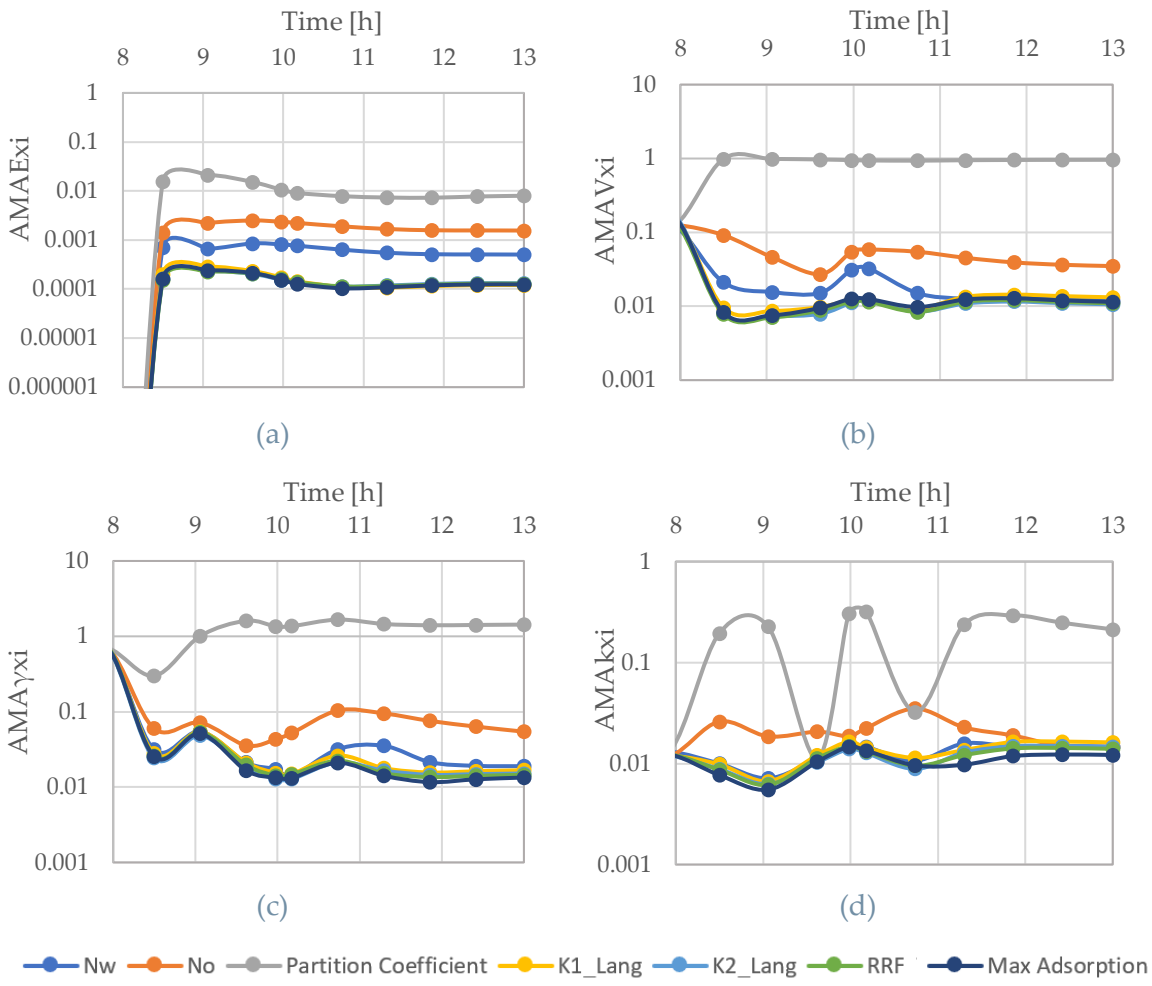

Figure 5.6: Time evolution of the global sensitivity index (a) $AMAE_{x_i}$ (b) $AMAV_{x_i}$ (c) $AMA\gamma_{x_i}$ (d) $AMAk_{x_i}$ of recovery factor.

Figure 5.6 suggests that statistical moments of recovery factor are very sensitive to partition coefficient during the whole flooding. This is consistent with the hypothesis made during model implementation, according to which solvent migration towards the oil in place drives the oil recovery process. Another

contribution that becomes evident when evaluating changes from unconditional to conditional mean value (Figure 5.6 (a)) is the one given by the exponents of the relative permeabilities. This would suggest that also wettability alteration process plays a role in oil mobilization although its impact is lower with respect to the previously cited one.

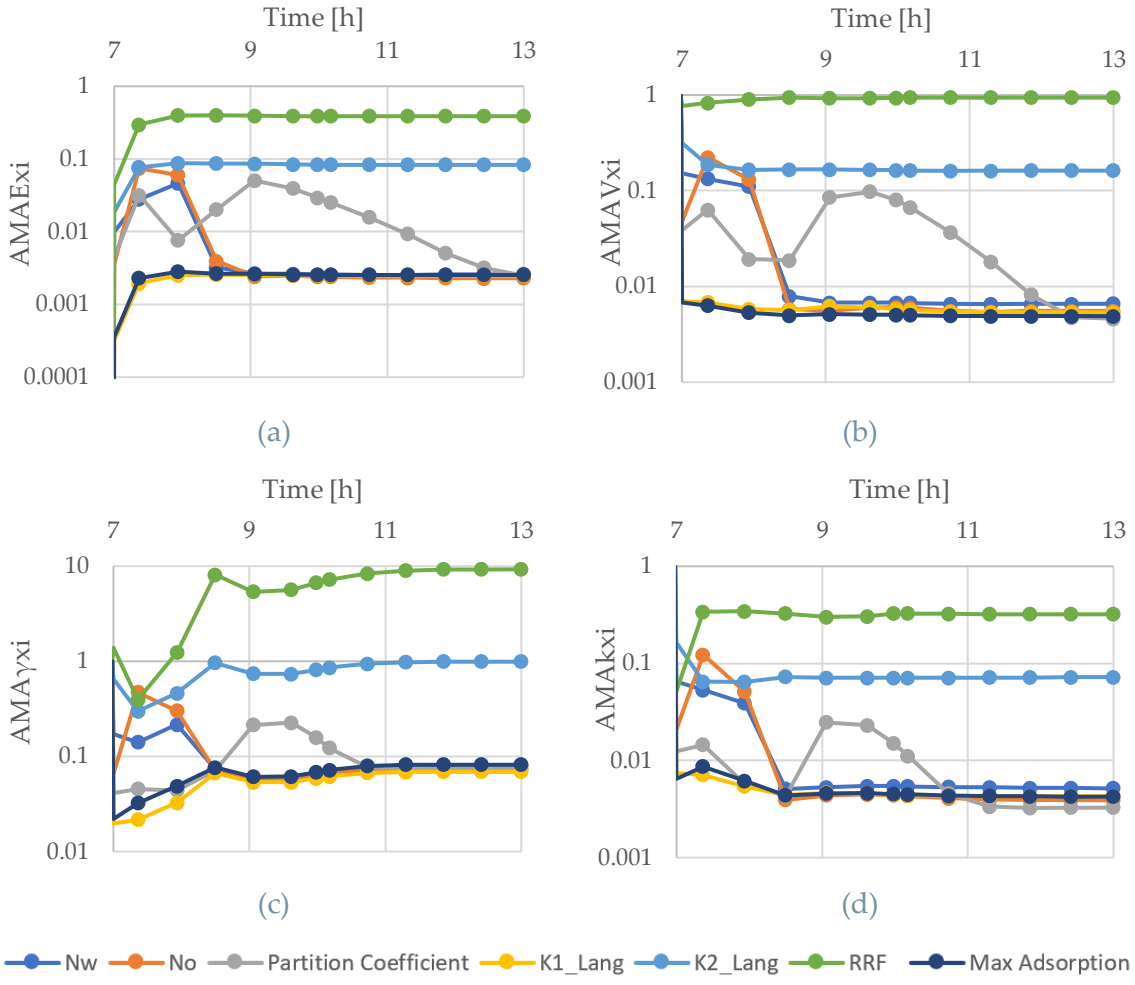

Figure 5.7: Time evolution of the global sensitivity index (a) $AMAE_{x_i}$ (b) $AMAV_{x_i}$ (c) $AMA\gamma_{x_i}$ (d) $AMAk_{x_i}$ of bottom hole pressure.

Concerning bottom hole pressure, it's possible to notice that the parameter governing *BHP* pdf is *RRF*. This appears reasonable if we keep into account that this variable describes the reduction of permeability caused by adsorption of surfactants onto rocks. According to Darcy law, a change in permeability causes in fact an inversely proportional modification in pressure drops across the sample, keeping all the other parameters constant. This is linked also to the second variable in order of importance: K_2 appearing in Langmuir isotherm. The trend shown by the two

parameters is very similar except for the very first timestep. Moreover, at early time also Corey exponents have a significative impact on *BHP* statistical moments.

6 Upscaling for Future Applications

Nanoemulsion flooding has been found to be an effective *EOR* technique at the laboratory scale, giving an incremental oil recovery of roughly 21% over the conventional water flooding. The History Matching (*HM*) procedure of both the flooding in slim tube and reservoir plug brought positive outcomes, showing how the different mechanisms involved in nanoemulsion application can contribute to the overall oil recovery.
Basing on the encouraging results obtained at the laboratory scale, reservoir simulations at the field scale are performed to assess the benefits in terms of *EOR* purposes of this innovative technique.
The Beta field, located in North Africa, has been selected to run the simulations, with the implementation of the nanoemulsion technique within the software STARS. Following the consolidated Eni workflow, if positive results are obtained, the first field application is represented by *SWCTT* and successively by a Pilot inter-well test as mentioned in Chapter 3 and illustrated in Figure 3.1.
Firstly, a sector has been built according to the Beta full-field model characteristics and it has been initialized to implement nanoemulsion options. The results obtained from the slim tube flooding *HM* and the previously defined nanoemulsion model are set as inputs to the sector model.
Then, forecast analyses has been performed, consisting in the comparison of different injection strategies scenarios to evaluate the differential production gained from an *EOR* technique with respect to waterflooding (*HSW*).
At the end, a preliminary economic analysis is performed to find the most convenient *EOR* technique.

6.1. Sector model

Model Setup

The full-field model, from which the sector is extracted, was created using the Eclipse simulator (Schlumberger). Since this tool lacks necessary features to reproduce nanoemulsion behavior, STARS (CMG) is once again chosen to implement forecast analysis. Therefore, the sector model has been built in STARS making sure to reproduce faithfully the production history belonging to the area of

interest. The latter corresponds to the area chosen to operate the single well chemical tracer test (*SWCTT*).

Rock data

The sector model construction starts with the definition of a 3-D grid (which dimensions are reported in Table 6.1) made of 12 layers, each 0.5 m thick. To reproduce the thermodynamic and fluid dynamic characteristics of the reservoir, the grid is located at a depth of 3370 m. In Figure 6.1 it's shown the entire grid together with the depth associated to each layer.

N. cells	20x16x12
Length (i dimension) [m]	2000
Height (j dimension) [m]	1600
Depth (k dimension) [m]	6
Volume [m^3]	$192 \cdot 10^5$
Cell i dimension (Δi) [m]	100
Cell j dimension (Δj) [m]	100
Cell k dimension (Δk) [m]	0.5

Table 6.1: Sector grid dimensions.

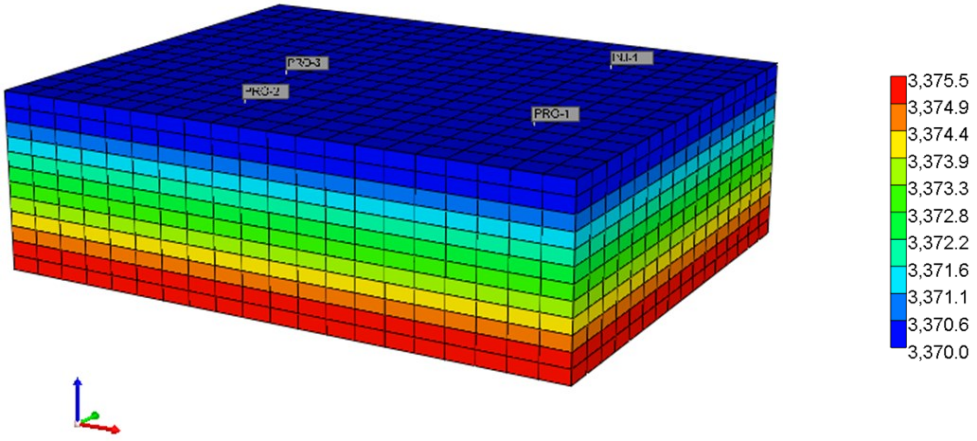

Figure 6.1: Sector model grid.

The petrophysical properties of the sector (Table 6.2) are assumed to be homogeneous on each layer but a vertical heterogeneity (z direction) is considered. The model has been filled with average field measurements value.

Layer	1	2	3	4	5	6	7	8	9	10	11	12
Porosity	0.21	0.20	0.20	0.20	0.19	0.20	0.20	0.19	0.18	0.17	0.13	0.12
Permeability (i direction) [mD]	82.3	80.1	80.4	86.4	91.1	90.4	86.5	82.5	82.7	75.9	64.7	55.4

Permeability (i direction) [mD]	82.3	80.1	80.4	86.4	91.1	90.4	86.5	82.5	82.7	75.9	64.7	55.4
Permeability (i direction) [mD]	8.23	8.01	8.04	8.64	9.11	9.04	8.65	8.25	8.27	7.59	6.47	5.54
Transmissibility (i direction) [mD m]	55.1	56.3	56.3	59.8	63.3	62.2	59.8	57.5	58.6	53.9	44.6	35.2
Transmissibility (j direction) [mD m]	68.0	69.2	65.7	70.4	73.9	76.2	72.7	70.4	71.5	64.5	53.9	42.2
Transmissibility (k direction) [mD m]	1834 75.5	1810 19.9	1869 37.1	1989 43.9	2032 92.1	1994 41.1	1896 06.1	1828 14.1	1757 92.2	1490 33.5	1273 51.2	1255 78.1

Table 6.2: Reservoir petrophysical properties.

Figure 6.2, Figure 6.3 and Figure 6.4 give a visual representation of porosity and permeability distribution within the model.

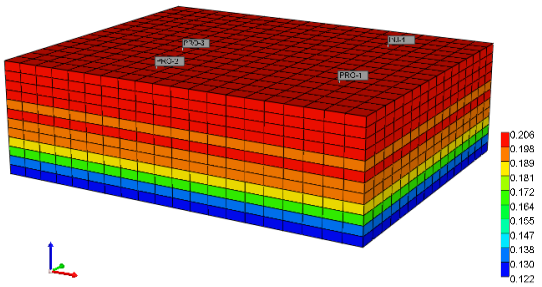

Figure 6.2: Reservoir porosity

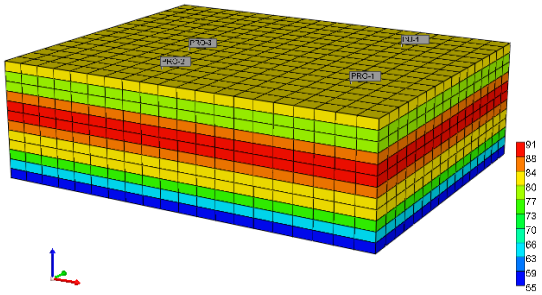

Figure 6.3: Reservoir permeability in i and j directions.

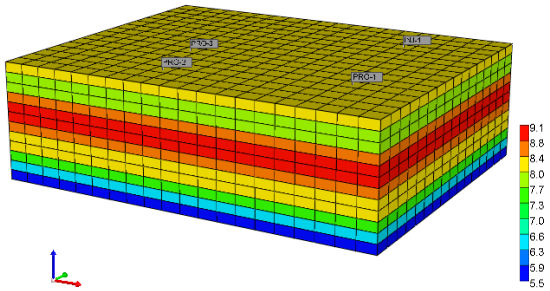

Figure 6.4: Reservoir permeability in k direction.

Fluid components data

Water and oil are the two phases present within the model since reservoir pressure is above the bubble point and hence free gas does not exist. Each phase is characterized by a set of properties that includes molecular weight, density, and viscosity. The oil is the same as in slim tube experiment. Fluids properties are listed in Table 6.3.

Fluid	MW [kg/mol]	Density [kg/m³]	Viscosity [cP]
Water	0.018	1209	0.253
Oil	0.07335	818	$\mu_o = f(T_{res}, P)$

Table 6.3: Fluids characteristics.

Moreover, it is essential to recall that in field operation modeling oil phase is still in "live" conditions, meaning that it contains dissolved gas in solution that may be released at surface conditions, contrary to what happens in laboratory activity (where dead oil is used). For this reason, it must be provided by a detailed design of its thermodynamic behavior.

To describe this behavior, a Black Oil model has been implemented in STARS. The software allows to specify the way oil and the eventual dissolved gas coming out of solution react when brought from reservoir to surface conditions. This is possible by using the following parameters, known from field tests [122]:

- R_s: it is the solution gas to oil ratio, defined as the number of standard cubic feet of gas which dissolve in one stock tank barrel of oil when both are taken to reservoir pressure. Figure 6.5 shows how the solution gas oil ratio of field Beta oil changes as a function of reservoir pressure at constant reservoir temperature.

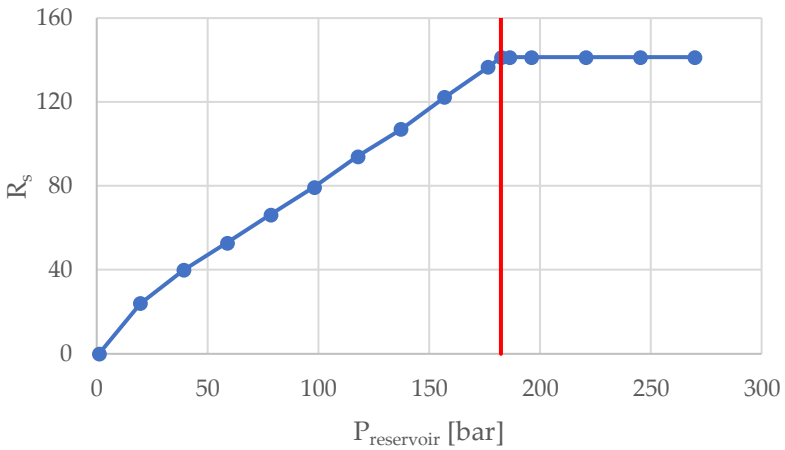

Figure 6.5: Solution gas to oil ratio trend.

R_s obtained from field data follows the typical trend of solution gas to oil ratio where it's possible to recognize:

1. A plateau from very high pressures until the bubble point pressure (indicated in the chart by the vertical line occurring at 182.4 bar) which suggests that the gas is in solution and the ratio has a constant value.

2. A decreasing part from bubble point pressure until 0, meaning that the amount of gas in solution is reducing in favor of an increase of free gas.

- B_o: it is the oil formation volume factor, which describes the shrinking of oil volume when passing from reservoir to surface conditions because of the lower gas content below Pb. It is defined as the ratio between the oil liquid volume at reservoir temperature and pressure and the oil liquid volume of the same sample at surface. Its trend is shown in Figure 6.6.

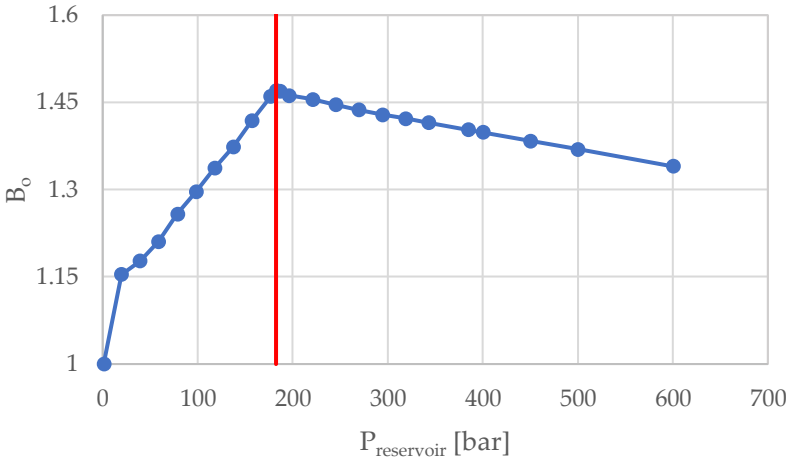

Figure 6.6: Oil formation volume factor trend.

As the reservoir pressure is decreased from initial pressure to bubble point pressure there is a slight expansion of the liquid. Then, when the reservoir pressure falls below the bubble point, gas comes out of solution and B_o decreases until a value of 1.

- μ_o: it is the oil viscosity, which is not constant when pressure changes are experienced. Its values are shown in Figure 6.7.

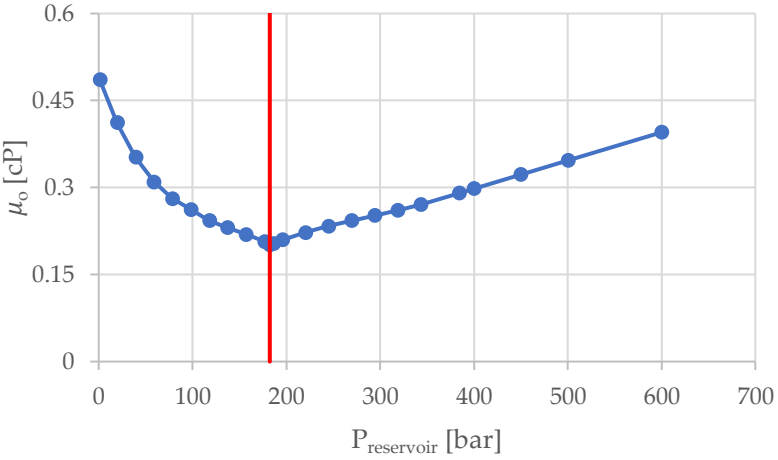

Figure 6.7: Oil viscosity trend.

- B_g: it is the gas formation volume factor, defined analogously to oil as the ratio of gas volume at reservoir conditions to the gas volume at standard conditions. Its trend is shown in Figure 6.8.

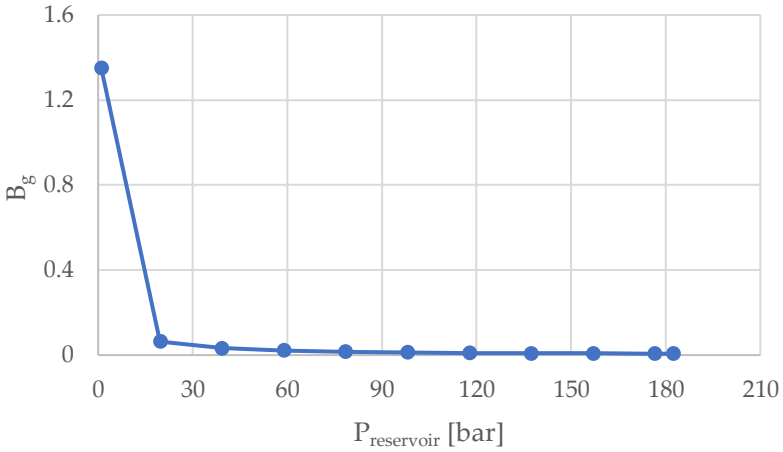

Figure 6.8: Gas formation volume factor trend.

- μ_g: it is the gas viscosity, once again not constant when there are pressure changes. Its values are displayed in Figure 6.9.

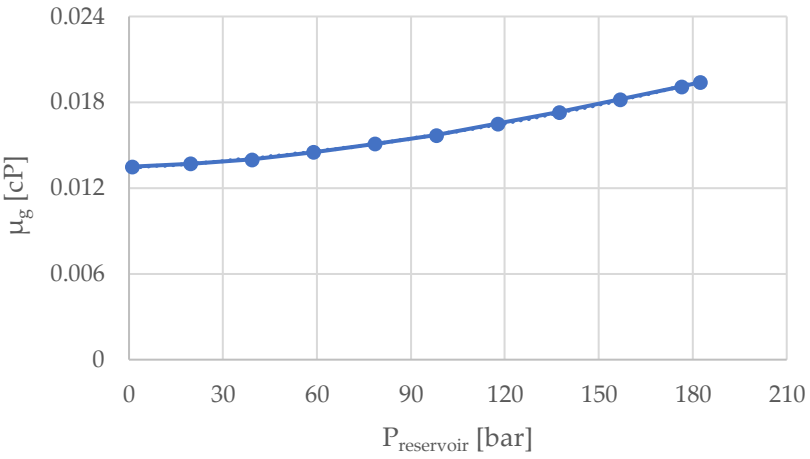

Figure 6.9: Gas viscosity trend.

Rock-fluid interaction data

In this section, as already explained in Chapter 4, saturation function curves are defined. Also in this case the relative permeabilities follow Corey's model (Equation (4.5) and (4.6)) and are specified together with the values of capillary pressure as a function of water saturation.

S_w	P_{cap}
0	3.105415
0.05	0.937611

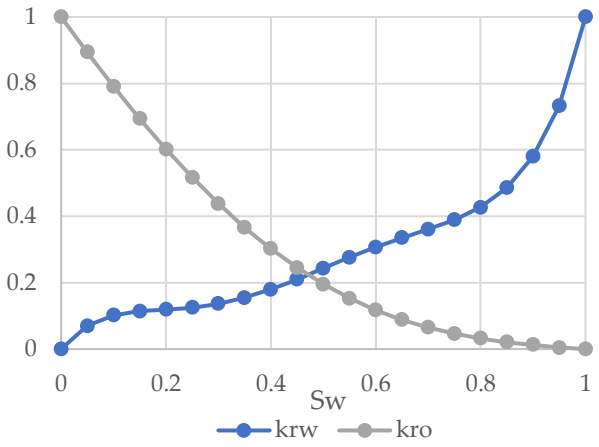

Figure 6.10: Water and oil relative permeabilities.

0.1	0.283091
0.15	0.085473
0.2	0.025807
0.25	0.007792
0.3	0.001457
0.35	0.00071
0.4	0.000214
0.45	6.48E-05
0.5	1.96E-05
0.55	0
0.6	0
0.65	0
0.7	0
0.75	0
0.8	0
0.85	0
0.9	0
0.95	0
1	0

Due to the presence of dissolved gas within the oil, also gas-liquid relative permeabilities need to be specified to properly describe the movement of gas coming out of solution.

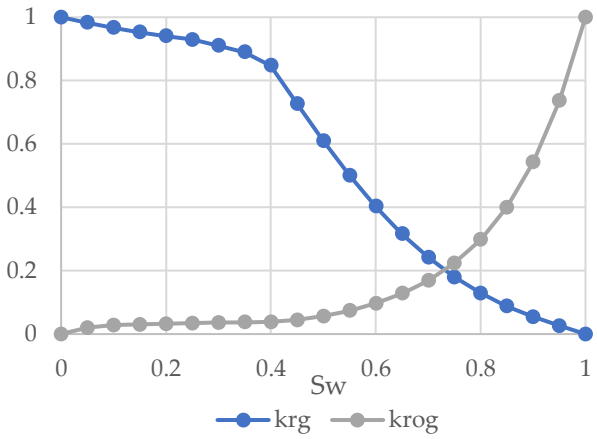

Figure 6.11: Gas-liquid relative permeabilities.

The relative permeability curves shown in Figure 6.10 and Figure 6.11 should be adjusted in view of the upscaling procedure passing from slim tube to sector model. This modification is achieved through Saturation table endpoints scaling. It provides a mechanism for redefining values of connate, critical, and maximum saturations in the saturation tables, for the description of reservoir fluids flow.

Initial conditions

At the beginning of the simulation the sector is characterized by an areal homogeneous distribution of water and oil saturation. Those fluids represent the only two phases present at the initial conditions since free gas is assumed to be absent in the reservoir. The described condition is summarized in terms of initial water saturations in Table 6.4 and displayed in Figure 6.12.

Layer	1	2	3	4	5	6	7	8	9	10	11	12
S_{wi}	0.29	0.30	0.30	0.31	0.32	0.31	0.32	0.33	0.36	0.39	0.47	0.50

Table 6.4: initial water saturation values for each layer.

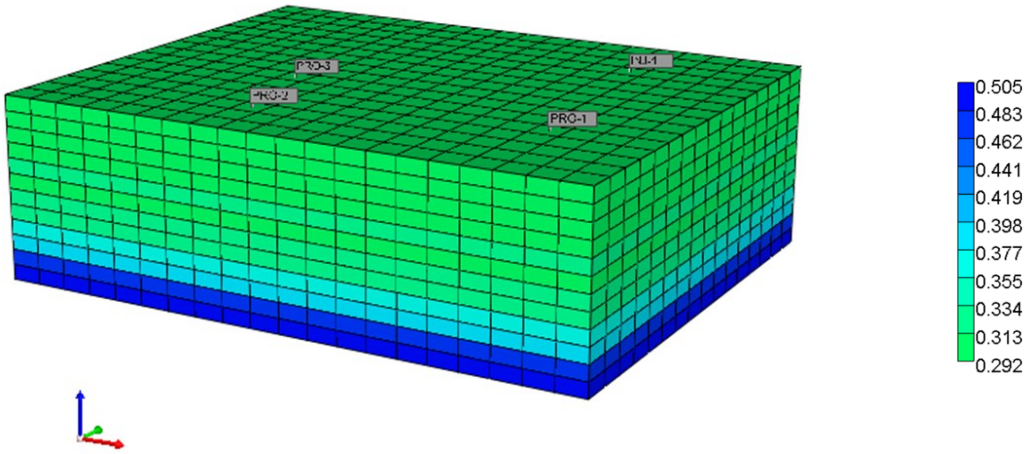

Figure 6.12: Initial water saturation over the 3-D grid.

Moreover, to fully characterize the original situation of the sector, it's fundamental to set the reservoir temperature – equal to 90°C – and a reference pressure. From field data the reference pressure results equal to 351.5 bar at a depth of 3360 m. However, since the grid is positioned between 3370 m and 3375 m, it's necessary to specify the value of pressure at these depths. To achieve this, water pressure gradient has been considered as shown in Equation (6.1):

$$P = P_{ref} + \rho_w \, g \, \Delta h \tag{6.1}$$

Where P is the pressure at the considered depth (3370 m), P_{ref} is the reference pressure known from field data, ρ_w is the water density and Δh is the difference between the considered depth and the reference one. At 3370 m pressure results equal to 352.69 bar.

Lastly, the oil water contact (*OWC*) is located at 3406 m, hence it is out of the generated sector.

Wells data

The number of wells inserted in the model and their positioning reproduce the configuration of real field. In particular, one injector and 3 producers are located on the grid as shown in Figure 6.13 and are provided by perforation on each layer.

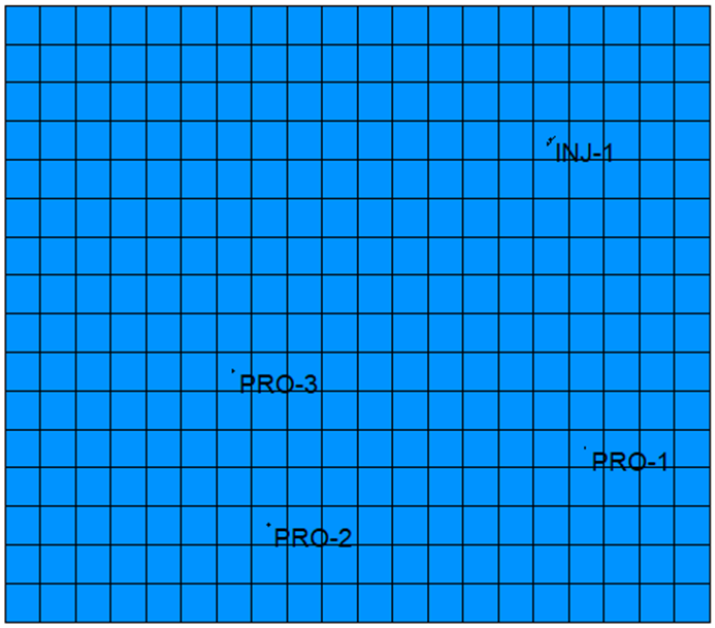

Figure 6.13: Wells positions.

Since the forecast simulations start from 2022 it is vital to reproduce the field conditions up to this date. To emulate the current Beta field status, values of real bottom hole pressure (*BHP*) and water cut (*WC*) need to be matched on producer 1 (Pro-1 in Figure 6.13) by the simulation. Producer 1 has been set as target well due to its proximity to the injection point. The values of quantities to be matched are equal to:

- *BHP* above bubble point (*BHP* = 185 bar, P_b = 182.4 bar);
- *WC* = 50%.

In order to reach this purpose a constant water injection and oil production profile has been respectively set to the injection and production wells. These constraints keep valid from the beginning of the simulation (startup of real field production, year 2000) until the specified *BHP* and *WC* values are registered on producer 1. Once the condition is fulfilled, producers 2 and 3 (Pro-2 and Pro-3 in Figure 6.13) are closed and the injection strategy on Inj-1 is changed according to Voidage Replacement (*VR*) = 1. This strategy ensures that the active production wells produce an amount of bottom-hole fluid in proportion to the total bottom-hole fluid

injected into the reservoir by the injection well, keeping the pressure constant. This approach is maintained until the present year (2022) is attained.

6.2. Production forecast in different scenarios

The production forecast scenarios exposed in this section aim at investigating at the field scale the additional contribution brought by nanoemulsion injection after the exploitation of Beta field performed through the sole waterflooding.

The nanoemulsion formulation used in this phase is the one used in slim tube flooding. Its properties have been already listed in Table 3.3.

Once defined the composition of the fluid to be injected, it is necessary to select a reference volume within the sector, which represents the basis for injection Pore Volume calculations. Given that for this preliminary forecast analysis it is sufficient to focus on one injector (Inj-1) and one producer (Pro-1), the examined volume includes only these two wells. It is highlighted by the red rectangle in Figure 6.14.

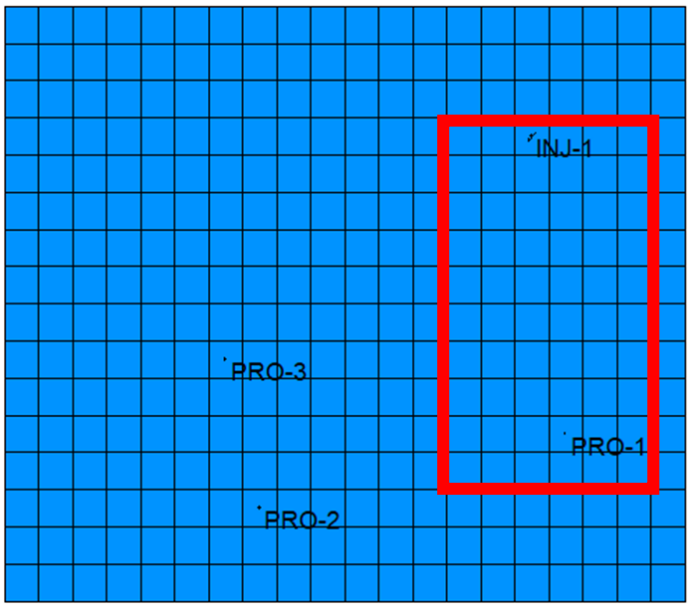

N. cells	6x11x12
Cell dimension (i direction) [m]	100
Cell dimension (j direction) [m]	100
Cell dimension (k direction) [m]	0.5

Figure 6.14: Selected reference volume for injection.

Keeping into account the entity of the reference volume considered and the porosity of each layer, it is possible to compute the void volume of the considered space. The total amount of oil within the referred volume to be displaced results equal to 478746 m^3 (1 PV). Nanoemulsion slug to be injected is determined as a chosen percentage of this number.

Once the PV is determined, 4 different nanoemulsion injection strategies have been elaborated:

1. An amount of 0.3 PV injected as a single slug;
2. An amount of 0.3 PV split into two separate injected slugs;
3. An amount of 0.1 PV injected as a single slug;
4. An amount of 0.5 PV injected as a single slug.

The quantity of *NE* slug injected in the first scenario has been set to 0.3 PV in agreement to the choice made during laboratory application. Then it has been changed to lower and higher values to investigate the effect of the injected volume of additional recovery. Moreover, a base case ("do nothing case") has been defined to compare nanoemulsions performance with waterflooding ones. This base case, indeed, simulates the exclusive injection of water for the whole duration of the forecast. In all the situations the same constraints on injection and production wells are set:

- Injection well: constant flow rate equal to 180 m^3/d;
- Production well: constant bottom hole pressure equal to 185 bar.

The injection startup is set in 2022 and all the simulations forecast last 28 years (up to 2050).

6.3. Forecast results

The results for each strategy have been collected in terms of oil production rate and cumulative oil production of the considered volume of interest. *WC* is also reported for every case to underline that the prevision is performed until a value for *WC* around 90% is attained at well Pro-1, as common practice for *EOR* processes suggests. In each chart the base case is also displayed to appreciate the improvements brought by nanoemulsion injection.

At the beginning strategy 1 and 2 have been compared to assess whether a different injection arrangement could have a consistent impact on recovery. In these first two cases 2.43 years are required for the complete injection of the slug.

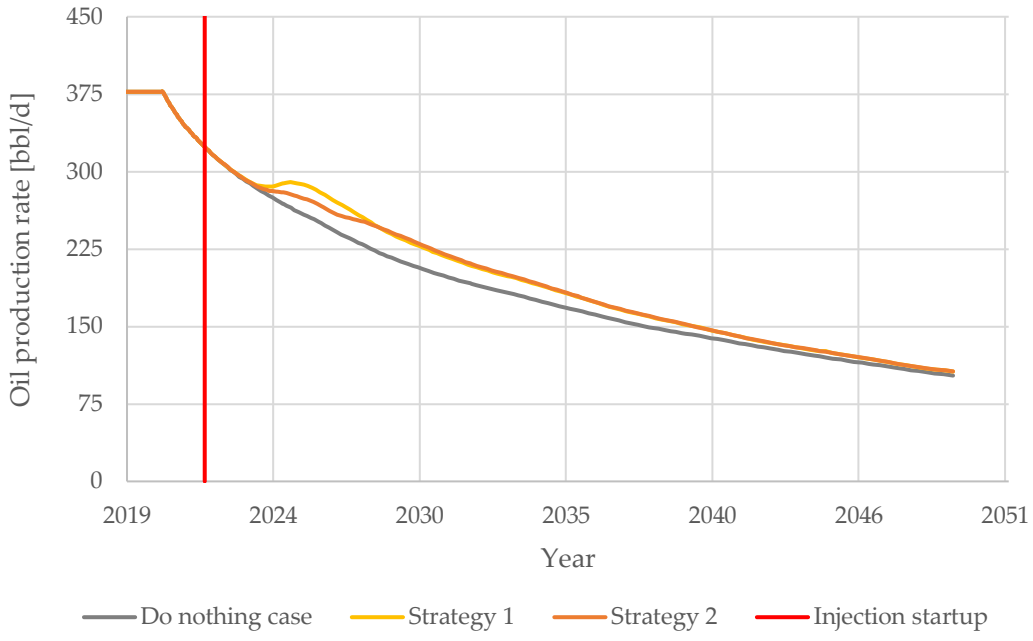

Figure 6.15: Oil production rate comparison between strategy 1 and 2.

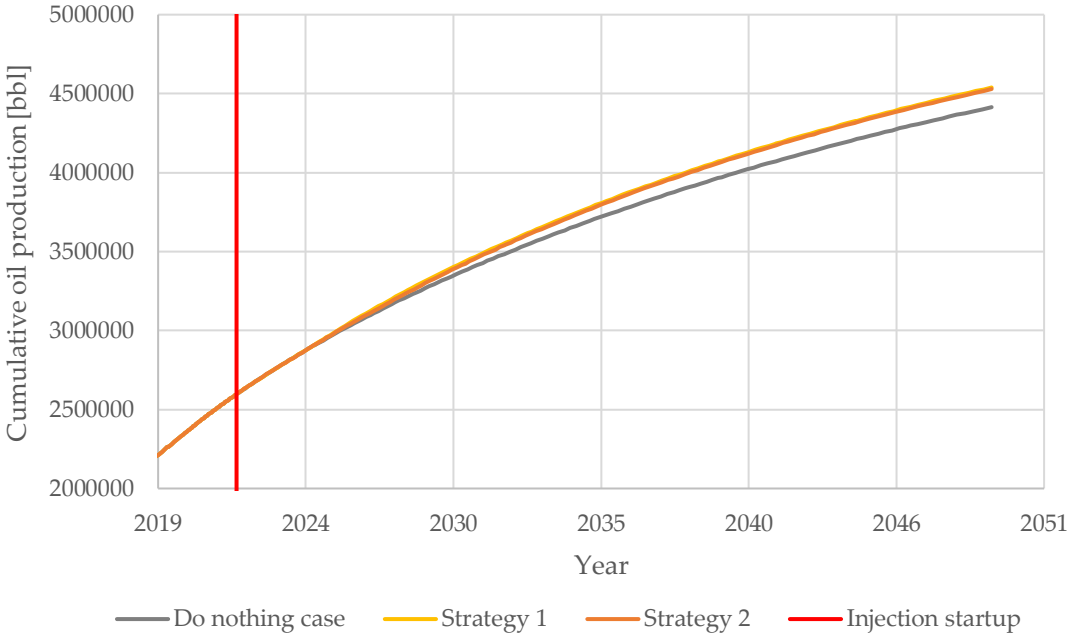

Figure 6.16: Cumulative oil production comparison between strategy 1 and 2.

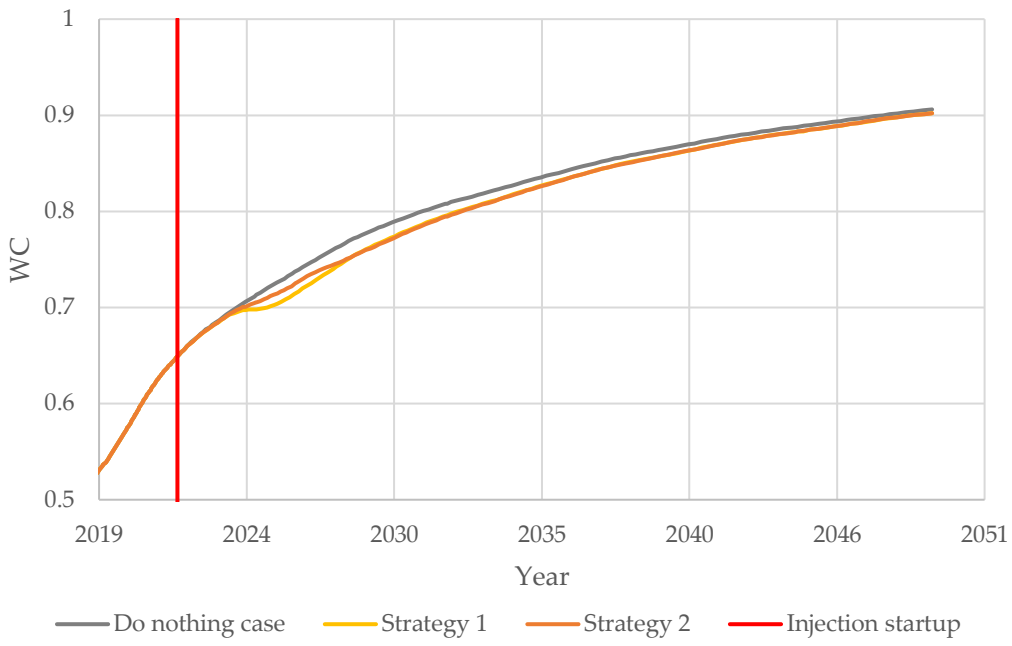

Figure 6.17: Water cut comparison between strategy 1 and 2.

Injection strategy	Cumulative oil production @ 2050 [bbl]
Base case	$4.41 \cdot 10^6$
Strategy 1	+ 130000
Strategy 2	+ 120000

Table 6.5: Cumulative production results from strategy 1 and 2.

Table 6.5 summarizes the gain obtained with strategies 1 and 2 with respect to the water injection. As itis possible to notice, the difference registered between the two arrangements is not substantial as expected in terms of cumulative oil production; however, the injection of the nanoemulsion in a single bigger volume does not give a significant load to the oil bank (Figure 6.15), failing in a potential early production with respect to the injection of the two smaller split nanoemulsion volumes.

The comparison among strategies at different *NE* injected amounts (i.e., strategy 1, 3 and 4) shows the higher efficacy of the case of 0.5 PV injected (Figure 6.19 and Table 6.6).

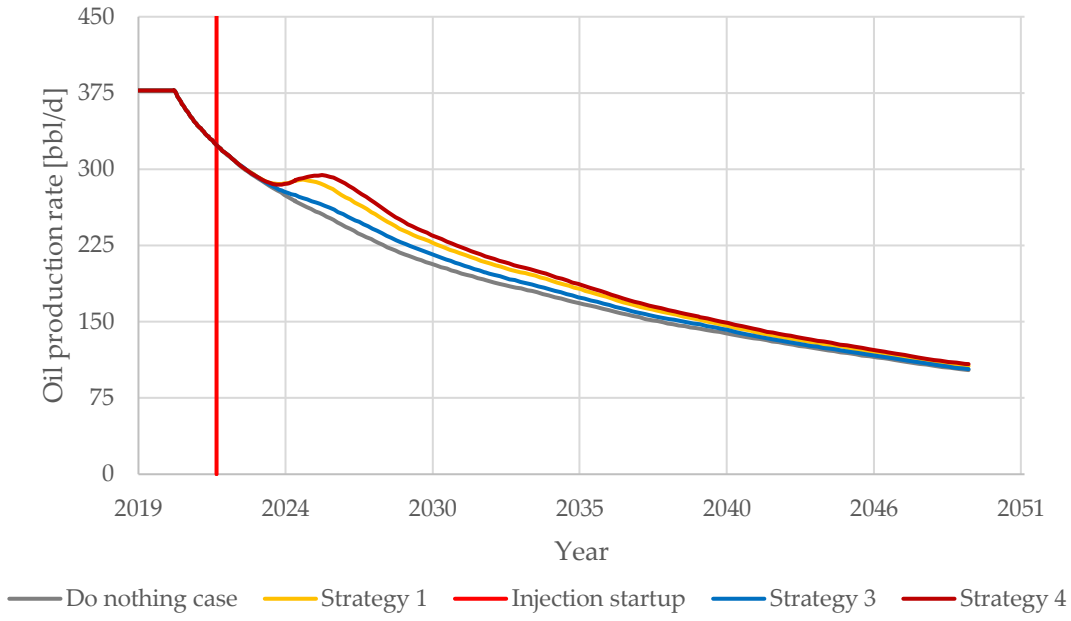

Figure 6.18: Oil production rate comparison between strategy 1, 3 and 4.

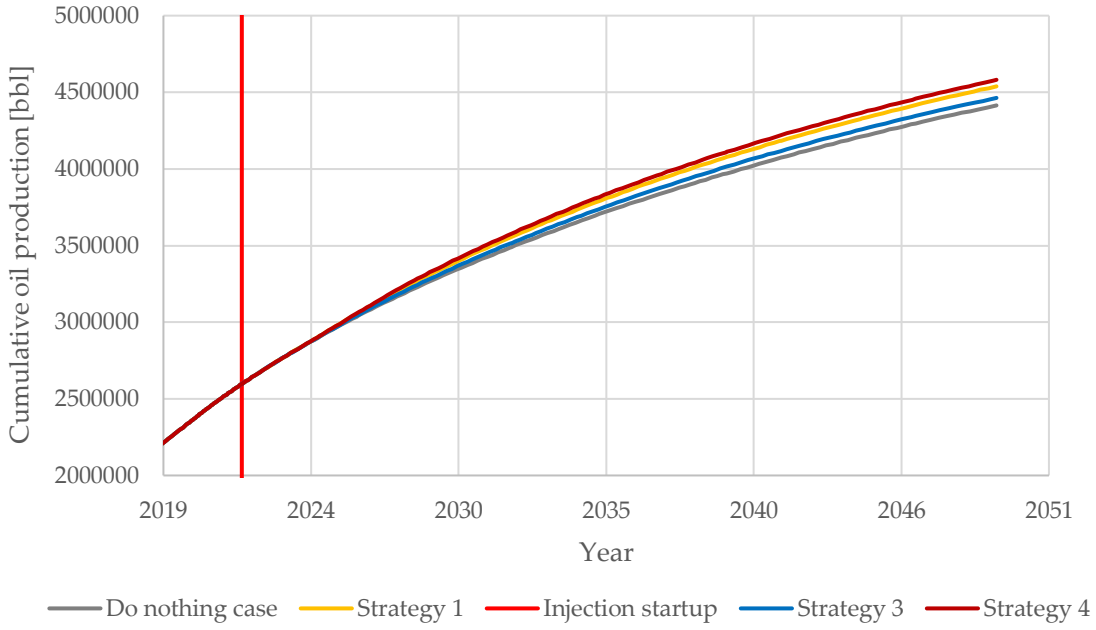

Figure 6.19: Cumulative oil production comparison between strategy 1, 3 and 4.

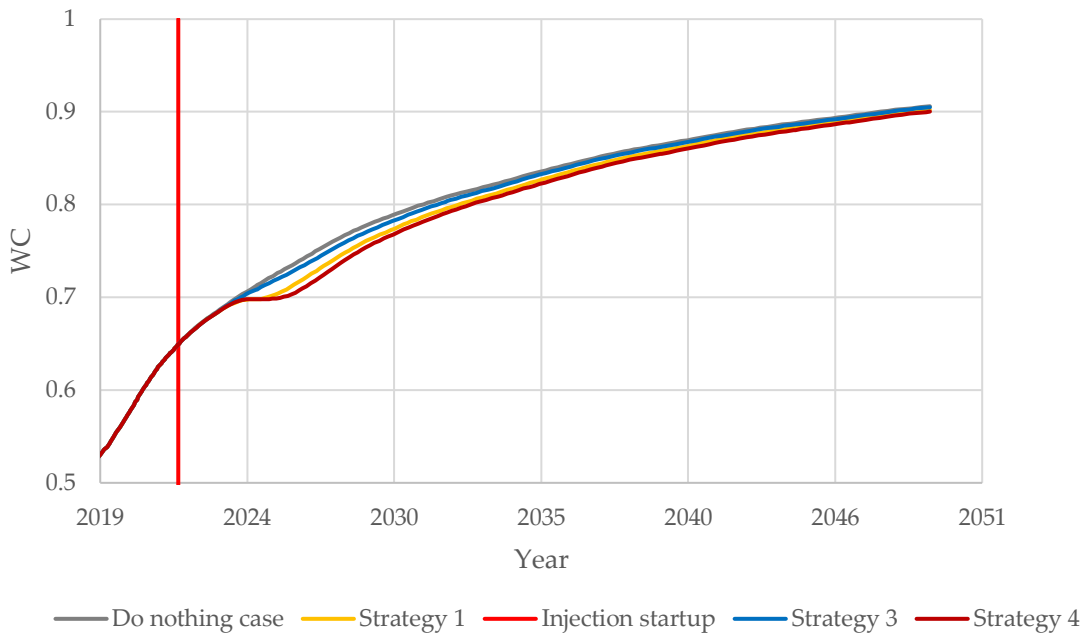

Figure 6.20: Water cut comparison between strategy 1, 3 and 4.

Injection strategy	Cumulative oil production @ 2050 [bbl]
Base case	$4.41 \cdot 10^6$
Strategy 1	+ 130000
Strategy 3	+ 50000
Strategy 4	+ 170000

Table 6.6: Cumulative production results from strategy 1, 3 and 4.

However, the drawback of injecting a huge amount of nanoemulsion is of course related to costs and time required for injection. As a matter of fact, in case 3 only 0.73 years are required for the complete injection versus the 3.64 years measured for strategy 4.

6.4. Preliminary economic evaluation

The incremental production of the analyzed forecast scenario must be accompanied by an economic evaluation to assess the effective feasibility of the *EOR* application process. Moreover, considering that the gain obtained with the different strategies is not so impacting, an estimation of costs associated to each of the considered scenario may help in the selection of the most affordable one. It's generally known that every industrial application relies on a trade-off condition: in this peculiar study, a greater cumulative oil production is reached considering higher costs for nanoemulsion injection and vice versa.

The incremental productions of nanoemulsion injection scenarios are compared with respect to waterflooding, in terms of *ΔNPV* (Net Present Value), *ΔCWP* (Cost When Produced) and *ΔCWP@WACC* (Discounted Cost When Produced):

$$\Delta NPV = \sum_{t=0}^{T} \frac{\Delta NCF_t}{(1+WACC)^t} \ [M\$] \tag{6.2}$$

$$\Delta\text{CWP} = \frac{\Delta(CAPEX + OPEX)}{\Delta Production} \left[\frac{\$}{bbl}\right] \tag{6.3}$$

$$\Delta\text{CWP@WACC} = \frac{\Delta(CAPEX + OPEX)@WACC}{(\Delta Production)@WACC} \left[\frac{\$}{bbl}\right] \tag{6.4}$$

The three economic indexes are computed from the year 0 to the year T = 28. The investments related to nanoemulsion plants construction are assumed to be done in the year 0 with no production delay in the year 1. The discount rate (*WACC*) is set at 10% and the oil price is set to 70 $/bbl according to Eni forecasts. No downtimes are considered. The costs are divided into *CAPEX*, related to specific pumps for nanoemulsion injection and storage tanks, and *OPEX*, related to fluid formulation and its transport. All the costs are listed in Table 6.7.

Injection pumps and storage tanks costs [M$]	0.5
Nanoemulsion formulation costs [$/ton]	1000
Nanomeulsion transport and injection costs [$/ton]	100

Table 6.7: Nanoemulsion injection costs.

It is possible to realize that *OPEX* are consistently higher than *CAPEX*, since there is no need of costly additional facilities with respect to waterflooding.

The incremental oil production values of the three analyzed scenarios (strategy 1, 3 and 4) at the end of forecast period with respect to waterflooding are reported in Table 6.8.

Injection strategy	Cumulative oil production @ 2050 [bbl]
Strategy 1	127000 bbl
Strategy 3	50855 bbl
Strategy 4	169000 bbl

Table 6.8: Incremental oil production for different analyzed scenario.

The results of the economic evaluation are summarized in Table 6.9.

Index	Strategy 1	Strategy 3	Strategy 4
ΔNPV [M$]	- 123.3	- 40.7	- 177.0

ΔCWP [$/bbl]	1211.6	908.8	1355.9
ΔCWP@WACC [$/bbl]	915415.9	764508.1	1005181

Table 6.9: Economic indices for the three different scenarios.

The results obtained from the preliminary economic evaluation are not encouraging. The negative value of the differential *NPV* suggests that the project is not economically feasible at the moment. This could be mainly related to the huge costs associated to nanoemulsion components and preparation, which make the technology still not affordable for field applications. In other words, the benefit coming from the additional production obtain from *EOR* application is not sufficient to overcome the related costs. Such consideration provides an important hint to guide the future tests and studies towards the optimization of nanoemulsion formulation in order to minimize the cost of operations. In particular, two procedures should be applied to improve economic results:

1. Optimization of nanoemulsion formulation activity at laboratory scale;
2. Optimization of injected volumes, keeping into account the possible cost amortization linked to higher employed nanoemulsion quantities at industrial level.

7 Conclusions

Nanoemulsion technology has been investigated in this thesis work, developed in collaboration with Eni, as potential applicable *EOR* technique. It represents a promising way to recover oil remaining in place after primary and secondary field production processes, helping in the sustainment of the increasing oil demand foreseen in next years. The efficacy of this fluid lies in its composition and emulsification strategy, which are responsible of the improved kinetic stability, low interfacial tension, unusual tunable rheology, and wettability alteration capacity even at small surfactant concentration. Results coming from the laboratory tests carried out by Eni, confirm the enhanced action of nanomulsion for oil mobilization in both plug and slim tube applications. In each case an additional recovery (~21% and ~16% respectively) has been reached in agreement with conventional *EOR* processes.

One major achievement of the present thesis work is the successful construction of the entire simulation workflow used to reproduce the laboratory experiments. This aspect represents a substantial innovation in nanoemulsion *EOR* studies, offering a concrete starting point for future improvements. Moreover, the elaborated model and the associated History Matching procedure have allowed to better understand which, among the mechanisms of action ascribed to this technology, have a crucial influence on oil recovery. In this context, the "solvent effect" has been identified as the main driving force to mobilize oil and bring it towards production wells. In addition to this, also *IFT* lowering and wettability alteration have been recognized as significative, even if their impact is considerably smaller compared to the solvent one. Such considerations have been validated through the *GSA* analysis, which scope is to understand how some of the input parameters of the model affect the probability density function of the output variable of interest: oil recovery factor in the considered case. From the examination of AMA indices, obtained with the aid of a *PCE* (Polynomial Chaos Expansion) surrogate model, it has been possible to demonstrate that statistical moments of recovery factor are very sensitive to partition coefficient during the whole flooding. This key parameter describes the solvent migration process towards oil in place, therefore its assessed importance on the output corroborates the initial assumptions.

The good response of the model at laboratory scale has encouraged the upscaling at field scale. A sector of the Beta field, a reservoir located in North Africa, has been chosen for this purpose. Different forecast scenarios have been performed considering a variable amount of nanoemulsion employed and different injection strategies. At the end of forecasting period, values of cumulative oil production from each case have been compared to the base case which accounts only for waterflooding, highlighting an enhancement in production linked this technology of roughly 170000 bbl in the best scenario.

A preliminary economic analysis has been carried out considering the production outcomes of the diverse forecast scenarios in the analyzed sector. Despite the improvement in oil recovered brought by nanoemulsion injection, economic indicators (*NPV*, *CWP*, and *CWP@WACC*) show the unaffordability of this technology. In other words, this technique results to be effective at field scale but the additional production obtained through this type of chemical *EOR* is not sufficient to recover costs and provide remuneration. A possible explanation of this fact lies in the expensive formation process of nanoemulsions, which requires costly components and advanced preparation methods. For this reason, in view of decreasing the production costs, an optimization in terms of formulation and injected volumes has been suggested.

In conclusion, this work also represents a precious help to strengthen the cooperation that exists between laboratory and simulation parts. In this sense the elaborated model has given to the experimental section a suggested path in terms of analysis and data measurements to be performed in order to reach a higher level of results reliability.

Bibliogaphy

[1] British Petroleum. Statistical Review of World Energy. 2021.

[2] British Petroleum. Energy Outlook 2020 edition. 2020.

[3] International Energy Agency. World Energy Outlook 2021. 2021.

[4] Soc. Pet. Eng. Petroleum Reserves Definitions [1997 Archive]. n.d.

[5] Zitha P, Felder R, Brown K, Mohanty K. Increasing Hydrocarbon Recovery Factors. Soc Pet Eng 2008:1–9.

[6] Novelli PM, Sella M, Giacca D, Mazzei R, Croce M. Hydrocarbons: Origin, Exploration and Production. 2005.

[7] Blunt M.J. Reservoir Engineering. 2017.

[8] Druetta P, Raffa P, Picchioni F. Chemical enhanced oil recovery and the role of chemical product design. Applied Energy 2019; 252:113480. https://doi.org/10.1016/j.apenergy.2019.113480.

[9] Lake LW. Enhanced oil recovery. United States: Old Tappan, NJ; Prentice Hall Inc.; 1989.

[10] Maugeri L. Oil: The Next Revolution. The unprecedented upsurge of oil production capacity and what it means for the world. Cambridge: 2012.

[11] Hughes L, Rudolph J. Future world oil production: Growth, plateau, or peak? Current Opinion in Environmental Sustainability 2011; 3:225–34. https://doi.org/10.1016/j.cosust.2011.05.001.

[12] Tunio SQ, Tunio AH, Ghirano NA, Mohamed Z, Adawy E. Comparison of Different Enhanced Oil Recovery Techniques for Better Oil Productivity. vol. 1. 2011.

[13] Alvarado V, Manrique E. Enhanced Oil Recovery: An Update Review. Energies (Basel) 2010; 3:1529–75. https://doi.org/10.3390/en3091529.

[14] Fanchi JR. Improved Recovery. Shared Earth Modeling, Elsevier; 2002, p. 272–81. https://doi.org/10.1016/B978-075067522-2/50016-1.

[15] Lake LW, Johns R, Rossen B, Pope GA. Fundamentals of enhanced oil recovery. vol. 1. Society of Petroleum Engineers Richardson, TX; 2014.

[16] Schlumberger. Schlumberger Oilfield Glossary n.d.

[17] Wang C, Liu P, Wang Y, Yuan Z, Xu Z. Experimental Study of Key Effect Factors and Simulation on Oil Displacement Efficiency for a Novel Modified Polymer BD-HMHEC. Scientific Reports 2018; 8:3860. https://doi.org/10.1038/s41598-018-22259-z.

[18] Lake LW, Schmidt RL, Venuto PB. A niche for enhanced oil recovery in the 1990s. Oilfield Review 1992; 4:55–61. https://doi.org/https://doi.org/.

[19] Taber JJ, Martin FD, Seright RS. EOR Screening Criteria Revisited - Part 1: Introduction to Screening Criteria and Enhanced Recovery Field Projects. Spe Reservoir Engineering 1997; 12:189–98.

[20] Shandrygin A, Lutfullin A. Current Status of Enhanced Recovery Techniques in the Fields of Russia. SPE Annual Technical Conference and Exhibition, Denver, Colorado, USA: SPE; 2008. https://doi.org/10.2118/115712-MS.

[21] Kumar A, Mandal A. Core-scale modelling and numerical simulation of zwitterionic surfactant flooding: Designing of chemical slug for enhanced oil recovery. Journal of Petroleum Science and Engineering 2020;192. https://doi.org/10.1016/j.petrol.2020.107333.

[22] Bera A, Mandal A. Microemulsions: a novel approach to enhanced oil recovery: a review. Journal of Petroleum Exploration and Production Technology 2015; 5:255–68. https://doi.org/10.1007/s13202-014-0139-5.

[23] Alvarado V, Manrique E. Enhanced Oil Recovery. Elsevier; 2010. https://doi.org/10.1016/C2009-0-30583-8.

[24] Satter A, Iqbal GM. Enhanced oil recovery processes: thermal, chemical, and miscible floods. Reservoir Engineering, Elsevier; 2016, p. 313–37. https://doi.org/10.1016/B978-0-12-800219-3.00017-6.

[25] Druetta P. Numerical simulation of chemical EOR processes. 2018.

[26] She H, Kong D, Li Y, Hu Z, Guo H. Recent Advance of Microbial Enhanced Oil Recovery (MEOR) in China. Geofluids 2019; 2019:1–16. https://doi.org/10.1155/2019/1871392.

[27] Del Gaudio L, Bortolo R, Lockhart TP. Nanoemulsions: A New Vehicle for Chemical Additive Delivery. SPE International Symposium on Oilfield Chemistry, Houston, Texas, USA: Society of Petroleum Engineers; 2007.

[28] Mathews RG, Donald AM. Conditions for Imaging Emulsions in the Environmental Scanning Electron Microscope. Scanning 2002; 24:75–85.

[29] Tadros TF. Emulsion Science and Technology: A General Introduction. Emulsion Science and Technology, John Wiley & Sons, Ltd; 2009, p. 1–56. https://doi.org/https://doi.org/10.1002/9783527626564.ch1.

[30] Tadros TF. Emulsions: Formation, Stability, Industrial Applications. Berlin/Boston, GERMANY: Walter de Gruyter GmbH; 2016.

[31] Dantas TNC, Santanna VC, Souza TTC, Lucas CRS, Dantas Neto AA, Aum PTP. Microemulsions and nanoemulsions applied to well stimulation and enhanced oil recovery (EOR). Brazilian Journal of Petroleum and Gas 2019; 12:251–65. https://doi.org/10.5419/bjpg2018-0023.

[32] Tadros T, Izquierdo P, Esquena J, Solans C. Formation and stability of nano-emulsions. Advances in Colloid and Interface Science 2004;108–109:303–18. https://doi.org/10.1016/j.cis.2003.10.023.

[33] Solans C, Solé I. Nano-emulsions: Formation by low-energy methods. Current Opinion in Colloid and Interface Science 2012; 17:246–54. https://doi.org/10.1016/j.cocis.2012.07.003.

[34] Druetta P, Raffa P, Picchioni F. Plenty of room at the bottom: Nanotechnology as solution to an old issue in enhanced oil recovery. Applied Sciences (Switzerland) 2018;8. https://doi.org/10.3390/app8122596.

[35] Forgiarini A, Esquena J, González C, Solans C. Formation of Nano-emulsions by Low-Energy Emulsification Methods at Constant Temperature. Langmuir 2001; 17:2076–83. https://doi.org/10.1021/la001362n.

[36] Forgiarini A, Esquena J, González C, Solans C. Studies of the relation between phase behavior and emulsification methods with nanoemulsion formation. In: Buckin V, editor. Trends in Colloid and Interface Science XIV, Berlin, Heidelberg: Springer Berlin Heidelberg; 2000, p. 36–9.

[37] Kumar N, Verma A, Mandal A. Formation, characteristics and oil industry applications of nanoemulsions: A review. Journal of Petroleum Science and Engineering 2021;206. https://doi.org/10.1016/j.petrol.2021.109042.

[38] Church J, Lundin JG, Diaz D, Mercado D, Willner MR, Lee WH, et al. Identification and characterization of bilgewater emulsions. Science of the Total Environment 2019; 691:981–95. https://doi.org/10.1016/j.scitotenv.2019.06.510.

[39] Griffin WC. Classification of surface-active agents by HLB. Journal of Cosmetic Science 1949; 1:311–26.

[40] Solans C, Izquierdo P, Nolla J, Azemar N, Garcia-Celma MJ. Nano-emulsions. Current Opinion in Colloid and Interface Science 2005; 10:102–10. https://doi.org/10.1016/j.cocis.2005.06.004.

[41] Braccalenti E, Gaudio L del, Belloni A, Albonico P, Radaelli E, Bartosek M, et al. Nanoemulsion flooding: the journey to field begins. 14th Offshore Mediterranean Conference and Exhibition, Ravenna, Italy: 2019.

[42] Uchenna O, Amendola A, Maddinelli G, Braccalenti E, Belloni A, Albonico P, et al. Nanoemulsion Enhanced Oil Recovery - From Theoretical Aspects to Coreflooding Simulation. IOR 2017 - 19th European Symposium on Improved Oil Recovery, vol. 2017, Stavanger, Norway: European Association of Geoscientists & Engineers; 2017, p. 1–9. https://doi.org/10.3997/2214-4609.201700236.

[43] Kumar N, Mandal A. Thermodynamic and physicochemical properties evaluation for formation and characterization of oil-in-water nanoemulsion. Journal of Molecular Liquids 2018; 266:147–59. https://doi.org/10.1016/j.molliq.2018.06.069.

[44] Moldoveanu SC, David V. Chapter 7 - RP-HPLC Analytical Columns. In: Moldoveanu SC, David V, editors. Selection of the HPLC Method in Chemical Analysis, Boston: Elsevier; 2017, p. 279–328. https://doi.org/https://doi.org/10.1016/B978-0-12-803684-6.00007-X.

[45] Pal N, Mandal A. Oil recovery mechanisms of Pickering nanoemulsions stabilized by surfactant-polymer-nanoparticle assemblies: A versatile surface energies' approach. Fuel 2020; 276:118138. https://doi.org/https://doi.org/10.1016/j.fuel.2020.118138.

[46] Kumar N, Mandal A. Wettability Alteration of Sandstone Rock by Surfactant Stabilized Nanoemulsion for Enhanced Oil Recovery—A Mechanistic Study. Colloids and Surfaces A: Physicochemical and Engineering Aspects 2020; 601:125043. https://doi.org/10.1016/j.colsurfa.2020.125043.

[47] Braccalenti E, Gaudio L del, Belloni A, Albonico P, Radaelli E, Bartosek M. Enhancing Oil Recovery With Nanoemulsion Flooding. 13th Offshore Mediterranean Conference and Exhibition, Ravenna, Italy: 2017.

[48] Kumar N, Mandal A. Experimental Investigation of PEG 6000/Tween 40/SiO2 NPs Stabilized Nanoemulsion Properties: A Versatile Oil Recovery Approach. Journal of Molecular Liquids 2020; 319:114087. https://doi.org/https://doi.org/10.1016/j.molliq.2020.114087.

[49] Kwok W, Hayes RE, Nasr-El-Din HA. Modelling dynamic adsorption of an anionic surfactant on berea sandstone with radial flow. Chemical Engineering Science 1995; 50:769–83.

[50] Yang F, Tchoukov P, Pensini E, Dabros T, Czarnecki J, Masliyah J, et al. Asphaltene Subfractions Responsible for Stabilizing Water-in-Crude Oil Emulsions. Part 1: Interfacial Behaviors. Energy & Fuels 2014; 28:6897–904. https://doi.org/10.1021/ef501826g.

[51] Javora PH, Baccigalopi G, Sanford J, Cordeddu C, Qu Q, Poole G, et al. Effective High-Density Wellbore Cleaning Fluids: Brine-Based and Solids-Free. SPE Drilling & Completion 2008; 23:48–54. https://doi.org/10.2118/99158-PA.

[52] Wang J, Zhou F-J. Cause analysis and solutions of water blocking damage in cracked/non-cracked tight sandstone gas reservoirs. Petroleum Science 2021;18:219–33. https://doi.org/10.1007/s12182-020-00482-6.

[53] Luo M, Si X, Zhang Y, Yuan Z, Yang D, Gong J. Performance Evaluation of Water Control with Nanoemulsion as Pre-pad Fluid in Hydraulically Fracturing Tight Gas Formations. Energy & Fuels 2017; 31:3698–707. https://doi.org/10.1021/acs.energyfuels.6b03291.

[54] Guan B, Jiang W, Liu P, Liang L, Yang J. Evaluation of Nanoemulsion to Improve the Fracturing Fluid Flowback. Proceedings of the 3rd International Conference on Material, Mechanical and Manufacturing Engineering, Atlantis Press; 2015, p. 171–8. https://doi.org/https://doi.org/10.2991/ic3me-15.2015.33.

[55] Mandal A, Bera A. Surfactant Stabilized Nanoemulsion: Characterization and Application in Enhanced Oil Recovery. World Academy of Science, Engineering and Technology, International Journal of Chemical, Molecular, Nuclear, Materials and Metallurgical Engineering 2012;6:537–42.

[56] Demikhova II, Likhanova N v., Hernandez Perez JR, Falcon DAL, Olivares-Xometl O, Moctezuma Berthier AE, et al. Emulsion flooding for enhanced oil recovery: Filtration model and numerical simulation. Journal of Petroleum Science and Engineering 2016; 143:235–44. https://doi.org/10.1016/j.petrol.2016.02.018.

[57] Ponce F. R v, Carvalho MS, Alvarado V. Oil recovery modeling of macro-emulsion flooding at low capillary number. Journal of Petroleum Science and Engineering 2014; 119:112–22. https://doi.org/https://doi.org/10.1016/j.petrol.2014.04.020.

[58] de Castro Dantas TN, de Souza TTC, Dantas Neto AA, Moura MCP de A, de Barros Neto EL. Experimental Study of Nanofluids Applied in EOR Processes. Journal of Surfactants and Detergents 2017; 20:1095–104. https://doi.org/10.1007/s11743-017-1992-2.

[59] Zhou Y, Yin D, Chen W, Liu B, Zhang X. A comprehensive review of emulsion and its field application for enhanced oil recovery. Energy Science & Engineering 2019; 7:1046–58. https://doi.org/https://doi.org/10.1002/ese3.354.

[60] Kumar N, Mandal A. Surfactant Stabilized Oil-in-Water Nanoemulsion: Stability, Interfacial Tension, and Rheology Study for Enhanced Oil Recovery Application. Energy & Fuels 2018; 32:6452–66. https://doi.org/10.1021/acs.energyfuels.8b00043.

[61] Kumar N, Pal N, Mandal A. Nanoemulsion flooding for enhanced oil recovery: Theoretical concepts, numerical simulation and history match. Journal of Petroleum Science and Engineering 2021; 202:108579. https://doi.org/https://doi.org/10.1016/j.petrol.2021.108579.

[62] Pal N, Mandal A. Enhanced oil recovery performance of gemini surfactant-stabilized nanoemulsions functionalized with partially hydrolyzed polymer/silica nanoparticles. Chemical Engineering Science 2020; 226:115887. https://doi.org/https://doi.org/10.1016/j.ces.2020.115887.

[63] Peng F, Ke Y, Zhao Y, Hu X, Zhao X. The influence of organically intercalated montmorillonites on the interfacial tension and structure of oil-in-water nanoemulsions. RSC Advances 2019; 9:13378–85. https://doi.org/10.1039/c8ra10595b.

[64] Noor MIIM, Islam A, Saalah S, Ken CC, Anisuzzaman SM, Kamin Z. Synthesis of nano emulsion from waste cooking oil for enhanced oil recovery applications. IOP Conference Series: Materials Science and Engineering, vol.

606, Institute of Physics Publishing; 2019. https://doi.org/10.1088/1757-899X/606/1/012004.

[65] Stefano A. Testing an Enhanced Oil Recovery Hybrid Technique: Low Salinity Polymer Injection. 2018.

[66] Jerauld GR, Mohammadi H, Webb KJ. Interpreting Single Well Chemical Tracer Tests. SPE Improved Oil Recovery Symposium, Tulsa, Oklahoma, USA: 2010. https://doi.org/https://doi.org/10.2118/129724-MS.

[67] Pandey A, Suresh Kumar M, Beliveau D, Corbishley DW. Chemical Flood Simulation of Laboratory Corefloods for the Mangala Field: Generating Parameters for Field-Scale Simulation. SPE Symposium on Improved Oil Recovery, Tulsa, Oklahoma, USA: SPE; 2008. https://doi.org/10.2118/113347-MS.

[68] Goudarzi A, Delshad M, Sepehrnoori K. A chemical EOR benchmark study of different reservoir simulators. Computers & Geosciences 2016; 94:96–109. https://doi.org/10.1016/J.CAGEO.2016.06.013.

[69] Lashgari H, Pope G, Balhoff M, Tagavifar M. New and Improved Physical Property Models for Chemical Flooding Simulators. SPE Reservoir Simulation Conference, Galveston, Texas, USA: SPE; 2019. https://doi.org/10.2118/193930-MS.

[70] Elhajjaji RR, Swedan A., Behr A, Awofodu DD, Hincapie R. Evaluation of a Chemical Enhanced Oil Recovery EOR Application in A Heterogeneous and Low Permeable Oil Reservoir: Advanced Screening by Reservoir Simulation. SPE Kuwait Oil & Gas Show and Conference, Kuwait City, Kuwait: SPE; 2017. https://doi.org/10.2118/187636-MS.

[71] Alfi M, Hosseini SA. Integration of reservoir simulation, history matching, and 4D seismic for CO2-EOR and storage at Cranfield, Mississippi, USA. Fuel 2016;175:116–28. https://doi.org/10.1016/J.FUEL.2016.02.032.

[72] Lei Z, Yuan S, Song J, Yuan J, Wu Y-S. AA Mathematical Model for Emulsion Mobilization and Its Effect on EOR during ASP Flooding. SPE Symposium on Improved Oil Recovery, Tulsa, Oklahoma, USA: SPE; 2008. https://doi.org/10.2118/113145-MS.

[73] Zuloaga-Molero P, Yu W, Xu Y, Sepehrnoori K, Li B. Simulation Study of CO2-EOR in Tight Oil Reservoirs with Complex Fracture Geometries. Nature Publishing Group 2016. https://doi.org/10.1038/srep33445.

[74] Guo Z, Dong M, Chen Z, Yao J. Dominant Scaling Groups of Polymer Flooding for Enhanced Heavy Oil Recovery. Industrial & Engineering Chemistry Research 2013; 52:911–21. https://doi.org/10.1021/ie300328y.

[75] Waggoner JR, Castillo JL, Lake LW. Simulation of EOR Processes in Stochastically Generated Permeable Media. SPE Formation Evaluation 1992; 7:173–80. https://doi.org/10.2118/21237-PA.

[76] Øystein P. Basics of Reservoir Simulation With the Eclipse Reservoir Simulator Lecture Notes 2006.

[77] Kumar Rai S, Bera A, Mandal A. Modeling of surfactant and surfactant-polymer flooding for enhanced oil recovery using STARS (CMG) software. Journal of Petroleum Exploration and Production Technology 2015; 5:1–11. https://doi.org/10.1007/s13202-014-0112-3.

[78] Computer Modelling Group Ltd. STARS (Advanced Processes & Thermal Reservoir Simulator) USER GUIDE 2018.

[79] Stanislaus BR, Mahmud HKB. Numerical Approach for Enhanced Oil Recovery with Surfactant Flooding using STARS (CMG). International Journal of Petroleum and Petrochemical Engineering 2017; 3:1–18. https://doi.org/10.20431/2454-7980.0304001.

[80] Qiao C, Khorsandi S, Johns RT. A General Purpose Reservoir Simulation Framework for Multiphase Multicomponent Reactive Fluids. SPE Reservoir Simulation Conference, Montgomery, Texas, USA: SPE; 2017. https://doi.org/10.2118/182715-MS.

[81] Liu H, Chen Z. A Scalable Thermal Reservoir Simulator for Giant Models on Parallel Computers. 2019.

[82] Goudarzi A, Delshad M, Sepehrnoori K. A Critical Assessment of Several Reservoir Simulators for Modeling Chemical Enhanced Oil Recovery Processes. SPE Reservoir Simulation Symposium, The Woodlands, Texas, USA: SPE; 2013. https://doi.org/10.2118/163578-MS.

[83] Chukwudeme EA, Fjelde I, Abeysinghe K, Lohne A. Effect of Interfacial Tension on Water/Oil Relative Permeability on the Basis of History Matching to Coreflood Data. SPE Reservoir Evaluation & Engineering 2014; 17:37–48. https://doi.org/10.2118/143028-PA.

[84] Kazempour M, Alvarado V, Manrique EJ, Izadi M. Impact of Alkaline-Surfactant-Polymer Flooding Model on Upscaled Recovery Predictions:

Medium and Heavy Oils. SPE Heavy and Extra Heavy Oil Conference, Latin America, Medellin, Colombia: SPE; 2014. https://doi.org/10.2118/171055-MS.

[85] Pal N, Mandal A. Compositional simulation model and history-matching analysis of surfactant-polymer-nanoparticle (SPN) nanoemulsion assisted enhanced oil recovery. J Taiwan Inst Chem Eng 2021; 122:1–13. https://doi.org/10.1016/j.jtice.2021.04.022.

[86] Callegaro C, Bartosek M, Masserano F, Nobili M, Parasiliti Parracello V, Pizzinelli C, et al. Opportunity of Enhanced Oil Recovery Low Salinity Water Injection - From Experimental Work to Simulation Study up to Field Proposal. EAGE Annual Conference & Exhibition incorporating SPE Europec, London, UK: European Association of Geoscientists & Engineers; 2013, p. cp-348-00363. https://doi.org/10.3997/2214-4609.20130888.

[87] AlSofi AM, Yousef AA. Insight into Smart-Water Recovery Mechanism through Detailed History Matching of Coreflood Experiments. SPE Reservoir Characterization and Simulation Conference and Exhibition, Abu Dhabi, UAE: SPE; 2013. https://doi.org/10.2118/166035-MS.

[88] Corey, T. A. The interrelation between gas and oil relative permeabilities. Producers Monthly 1954:38–41.

[89] Meng X, Gu X, Wu J, Vesovic V. Viscosity measurements of ortho-xylene, meta-xylene, para-xylene and ethylbenzene. The Journal of Chemical Thermodynamics 2016; 95:116–23. https://doi.org/https://doi.org/10.1016/j.jct.2015.11.027.

[90] Zhou Y, Wu J, Lemmon EW. Thermodynamic Properties of o-Xylene, m-Xylene, p-Xylene, and Ethylbenzene. Journal of Physical and Chemical Reference Data 2012;41. https://doi.org/10.1063/1.3703506.

[91] Rice NM, Irving HMNH, Leonard MA. Nomenclature for liquid-liquid distribution (solvent extraction) (IUPAC Recommendations 1993). Pure and Applied Chemistry 1993; 65:2373–96. https://doi.org/10.1351/pac199365112373.

[92] CRODA. Safety Data Sheet: Zephrym PD 4913-LQ-(MV) 2018.

[93] Sigma-Aldrich. Scheda di dati di sicurezza: Span 80 2019.

[94] BASF. Safety Data Sheet: Glucopon 600 UP 2017.

[95] Bravo Rodriguez V, Jurado Alameda E, Reyes Requena A, Garcia Lopez AI, Bailon-Moreno R, Cuevas Aranda M. Determination of Average Molecular

Weight of Commercial Surfactants: Alkylpolyglucosides and Fatty Alcohol Ethoxylates. J Surfactants Deterg 2005; 8:341–6.

[96] Cheng X, Kleppe J, Torsæter O. Simulation study of surfactant injection in a fractured core. Journal of Petroleum Exploration and Production Technology 2019; 9:3079–90. https://doi.org/10.1007/s13202-019-0705-y.

[97] Hakiki F, Maharsi DA, Marhaendrajana T. Surfactant-Polymer Coreflood Simulation and Uncertainty Analysis Derived from Laboratory Study. Journal of Engineering and Technological Sciences 2015; 47:706–25. https://doi.org/10.5614/j.eng.technol.sci.2015.47.6.9.

[98] Pal N, Mandal A. Numerical simulation of Enhanced Oil Recovery (EOR) studies for aqueous Gemini Surfactant-Polymer-Nanoparticle system. Authorea 2020. https://doi.org/10.22541/au.158921497.75237962.

[99] Grattoni CA, Dawe RA, Bidner MS. On the simultaneous determination of dispersion and nonlinear adsorption parameters from displacement tests by using numerical models and optimisation techniques. Advances in Water Resources 1993:127–35.

[100] Curbelo FDS, Santanna VC, Neto ELB, Dutra TV, Dantas TNC, Neto AAD, et al. Adsorption of nonionic surfactants in sandstones. Colloids and Surfaces A: Physicochemical and Engineering Aspects 2007; 293:1–4. https://doi.org/10.1016/j.colsurfa.2006.06.038.

[101] Kumar A, Mandal A. Critical investigation of zwitterionic surfactant for enhanced oil recovery from both sandstone and carbonate reservoirs: Adsorption, wettability alteration and imbibition studies. Chemical Engineering Science 2019;209. https://doi.org/10.1016/j.ces.2019.115222.

[102] Azam MR, Tan IM, Ismail L, Mushtaq M, Nadeem M, Sagir M. Static adsorption of anionic surfactant onto crushed Berea sandstone. Journal of Petroleum Exploration and Production Technology 2013; 3:195–201. https://doi.org/10.1007/s13202-013-0057-y.

[103] Zhang R, Somasundaran P. Advances in adsorption of surfactants and their mixtures at solid/solution interfaces. Advances in Colloid and Interface Science 2006;123–126:213–29. https://doi.org/10.1016/j.cis.2006.07.004.

[104] Park S, Lee ES, Sulaiman WRW. Adsorption behaviors of surfactants for chemical flooding in enhanced oil recovery. Journal of Industrial and Engineering Chemistry 2015; 21:1239–45. https://doi.org/10.1016/j.jiec.2014.05.040.

[105] ExxonMobil. Scheda di sicurezza: Solvesso 150 ND 2019.

[106] Jalilian M, Tabzar A, Ghasemi V, Mohammadzadeh O, Pourafshary P, Rezaei N, et al. An experimental investigation of nanoemulsion enhanced oil recovery: Use of unconsolidated porous systems. Fuel 2019; 251:754–62. https://doi.org/10.1016/j.fuel.2019.02.122.

[107] Dell'Oca A, Riva M, Guadagnini A. Moment-based metrics for global sensitivity analysis of hydrological systems. Hydrology and Earth System Sciences 2017; 21:6219–34. https://doi.org/10.5194/hess-21-6219-2017.

[108] Sudret B. Global sensitivity analysis using polynomial chaos expansions. Reliability Engineering and System Safety 2008; 93:964–79. https://doi.org/10.1016/j.ress.2007.04.002.

[109] Russian A, Riva M, Russo ER, Chiaramonte MA, Guadagnini A. Stochastic Inverse Modeling and Global Sensitivity Analysis to Assist Interpretation of Drilling Mud Losses in Fractured Formations. Stochastic Environmental Research and Risk Assessment 2019;33.

[110] Zhou X, Al-Otaibi F, Kokal S. Relative permeability characteristics and wetting behavior of supercritical CO2 displacing water and remaining oil for carbonate rocks at reservoir conditions. Energy and Fuels 2019; 33:5464–75. https://doi.org/10.1021/acs.energyfuels.9b01053.

[111] Knobloch LO, Reina REH, Födisch H, Ganzer L. Qualitative and Quantitative Evaluation of Permeability Changes during EOR Polymer Flooding Using Micromodels. World Journal of Engineering and Technology 2018; 06:332–49. https://doi.org/10.4236/wjet.2018.62021.

[112] Shi L, Ye Z, Zhang Z, Zhou C, Zhu S, Guo Z. Necessity and feasibility of improving the residual resistance factor of polymer flooding in heavy oil reservoirs. Petroleum Science 2010; 7:251–6. https://doi.org/10.1007/s12182-010-0029-5.

[113] Castro RH, Llanos S, Rodríguez J, Quintero HI, Manrique E. Polymers for eor application in high temperature and high viscosity oils: Rock–fluid behavior. Energies (Basel) 2020;13. https://doi.org/10.3390/en13225944.

[114] dos Santos Azevedo J, Oliveira SP. A numerical comparison between quasi-Monte Carlo and sparse grid stochastic collocation methods. Communications in Computational Physics 2012; 12:1051–69. https://doi.org/10.4208/cicp.260111.230911a.

[115] Lever V. Analisi di sensitività globale basata su espansione in caos polinomiale per lo studio di processi di trasporto reattivo a scala di bacino. 2010.

[116] Stuttgarter V, Valentin J, Roberts S, Radetzki IM. B-Splines for Sparse Grids: Algorithms and Application to Higher-Dimensional Optimization. Stuttgart, Germany: 2019.

[117] Hadigol M, Doostan A. Least squares polynomial chaos expansion: A review of sampling strategies. Computer Methods in Applied Mechanics and Engineering 2018; 332:382–407. https://doi.org/10.1016/j.cma.2017.12.019.

[118] Tarantola S, Becker W, Zeitz D. A comparison of two sampling methods for global sensitivity analysis. Computer Physics Communications 2012; 183:1061–72. https://doi.org/10.1016/j.cpc.2011.12.015.

[119] Sudret B. Polynomial chaos expansion and stochastic finite element methods. In: Phoon K, Ching J, editors. Risk and Reliability in Geotechnical Engineering, CRC Press; 2015, p. 265–300.

[120] Xiu D, Karniadakis GE. The Wiener-Askey polynomial chaos for stochastic differential equations. SIAM Journal on Scientific Computing 2002; 24:619–44.

[121] Soize C, Ghanem R. Physical Systems with Random Uncertainties: Chaos Representations with Arbitrary Probability Measure. SIAM Journal on Scientific Computing 2004; 26:395–410. https://doi.org/10.1137/S1064827503424505.

[122] Guo B, Liu X, Tan X. Chapter 2 - Properties of Petroleum Fluids. In: Guo B, Liu X, Tan X, editors. Petroleum Production Engineering (Second Edition), Boston: Gulf Professional Publishing; 2017, p. 19–36. https://doi.org/https://doi.org/10.1016/B978-0-12-809374-0.00002-7.

List of Figures

List of Tables

List of symbols

Variable	Description	SI unit
S_{or}	residual oil saturation	-
S_{oi}	initial oil saturation	-
S_{wi}	initial water saturation	-
$\Delta G_{formation}$	Gibbs free energy of formation	kJ
γ	interfacial tension	mN/m
A	area	m^2
T	temperature	K
S	entropy	J/K
k	permeability	D
P	pressure	Pa
L	length	m
μ	viscosity	Pa·s
q	fluid flux	m/s
MW	molecular weight	g/mol
ρ	density	kg/m^3
S	saturation	-
T	transmissibility	mD·m
k_r	relative permeability	-

n_o, n_w	Corey exponents	-
R_s	solution gas to oil ratio	-
P_b	bubble point pressure	Pa
B	formation volume factor	-

List of acronyms

ANOVA	ANalysis Of VAriance
ASP	Alkaline Surfactant Polymer
BHP	Bottom Hole Pressure
CAPEX	CAPital EXpenditure
CMC	Critical Micelle Concentration
CMG	Computer Modelling Group
CSS	Cycling Steam Stimulation
CWP	Cost When Produced
DECE	Designed Exploration and Controlled Evolution
ED	Displacement Efficiency
EM	ElectroMagnetic radiation heating
EOR	Enhanced Oil Recovery
ER	Electrical Resistive
EV	Volumetric sweep Efficiency
GSA	Global Sensitivity Analysis
HLB	Hydrophilic-Lipophilic Balance
HM	History Matching
HSW	High Salinity Water
IEA	International Energy Agency
IFT	InterFacial Tension
KRs	Relative permeability curves
LSA	Local Sensitivity Analysis
MAE	Mean Absolute Error
MC	Monte Carlo
MRE	Mud Removal Efficiency
NCF	Net Cash Flow
NPV	Net Present Value
OOIP	Original Oil In Place
OPEX	OPerating EXpenditure
OWC	Oil-Water Contact
PCE	Polynomial Chaos Expansion
PIT	Phase Inversion Temperature
PV	Pore Volume

QMC	Quasi Monte Carlo
RF	Recovery Factor
RRF	Residual Resistance Factor
SAGD	Steam Assisted Gravity Drainage
SG	Sparse Grids
SRC	Standardized Regression Coefficients
STARS	Steam Thermal and Advanced processes Simulator
SWCTT	Single Well Chemical Tracer Test
VR	Voidage Replacement
WACC	Weighted Average Cost of Capital
WC	Water Cut

Acknowledgments

This thesis work has been developed in the EORG (Enhanced Oil Recovery & Geomechanics) and LAIP (Laboratori Ingegneria del Petrolio) departments of Eni during my internship period.

I would like to express my sincere gratitude to all the people who have helped me to finalize the project, allowing me to get at the end of this study course.

First of all, I would like to thank Professor Alberto Guadagnini, whose expertise has been invaluable in approaching the problem with a robust methodology. His insightful feedback pushed me to sharpen my thinking and brought my work to a higher level.

An irreplaceable figure has been my company advisor Martina Sambiase of EORG, that deserves my warmest thank for the support given to me in understanding the analyzed topics and the constant positive presence during the development of the thesis.

I would also like to express my sincere gratitude to all the people of Eni who provided me the necessary material and information to complete my work.

I am truly grateful to Rafael Leonardo Sandoval Pabon for his great willingness to clarify my doubts and help me with the encountered issues.

Finally, I would like to thank my family infinitely, for encouraging me even when I was on the point to give up, and my boyfriend, for his constant motivation and understanding.